smart Tectonics

2019

Over-pressured caverns and leakage mechanisms Part 3: Dome-scale analysis

smartTectonics GmbH

DR. TOBIAS BAUMANN
PROF. DR. BORIS KAUS
DR. ANTON POPOV

Table of Contents

1 Introduction 5

2 Literature review 7

2.1 Stresses within salt structures 8

2.1.1 Constraints from the microstructure 8

2.1.2 Constraints from in-situ measurements 10

2.1.3 Models of stresses within salt structures 11

2.2 Stresses around salt structures 20

2.2.1 Numerical models 20

2.3 Effect of differential stresses within salt on cavity and hole closure 23

2.4 Summary 27

3 Salt rheology 28

3.1 Review of Creep Laws 29

3.2 Grain size and recrystallization 35

3.3 From microscale to macroscale 40

3.4 Summary 41

4 Modeling 43

4.1 Numerical approach 44

4.1.1 Mathematical description 44

4.1.2 Numerical implementation 46

4.2 Boundary Conditions 47

4.2.1 Tectonic boundary conditions 47

4.2.2 Glacial tectonic boundary conditions 48

4.2.3 Temperature boundary and initial conditions 49
4.3 Model geometries, resolution and rock parameters 50
4.4 Salt Pillow 54
4.4.1 Reference model with coupled PS-DC creep 54
4.4.2 Variations of the reference model with coupled PS-DC creep 57
4.4.3 Models with deactivated pressure solution creep 59
4.4.4 The effect of glacial loading: Coupled PS-DC creep models 63
4.4.5 The effect of glacial loading: DC creep models 65
4.4.6 Summary: Differential stresses induced by glacial loading 65
4.4.7 Summary and key observations 67
4.5 Salt wall model 68
4.5.1 Changes due to larger grain size and tectonic deformation 71
4.5.2 The effect of different DC-creep laws 71
4.5.3 The effect of tectonic deformation 72
4.5.4 Relative changes in maximum differential stress 76
4.5.5 The effect of glacial loading for the salt wall scenario 78
..... 80
4.5.6 Summary and key observations 81
4.6 Flat bedded salt 82
4.6.1 Ranges of differential stress for coupled PS-DC creep rheology 82
4.6.2 DC-creep reference model of flat-bedded salt 84
4.6.3 Variations of the DC-creep reference model 84
4.6.4 Summary and key observations 89
5 Summary and Recommendations 90

5.1 Overall summary 90
5.2 Recommendations 92
6 References 94

1 Introduction

In order to estimate the risk for fracking or permeation to occur during the longterm abandonment of salt cavities, we need a thorough understanding of the state of stress of the salt dome.

In most cavern-scale numerical models, deviatoric stresses within the salt dome are assumed to be negligible in magnitude. Yet, as salt structures are typically not homogeneous, this assumption is known to be incorrect, particularly by practitioners drilling through salt (Willson and Fredrich 2005). Stress variations may be caused by internal heterogeneities such as the presence of anhydrite layers, or by the large-scale structure and ongoing deformation of the salt dome or pillow as a result of their lower density compared to the overlying rocks.

The rheology of the salt itself, a not very well constrained parameter which varies significantly between different types of salt, may also have a significant effect. (Cornet, Dabrowski, and Schmid 2018a) for example, analyzed the closure of a borehole through salt and showed that when preexisting deformation or stresses exist, a significant change in the effective viscosity of the salt may occur, which increases the rate of closure. The magnitude and orientation of stresses within salt domes is thus an essential factor to estimate whether more detailed calculations are required, or whether it can be considered safe to neglect them in cavity-scale models.

Yet, the stress state in the host rock above the salt structure also plays a significant role as it determines whether a fracture, once initiated, propagates to the surface or whether it takes a different pathway (which is dictated by the orientation and magnitude of the maximum principal stress). Moreover, the permeability and stratigraphy of rocks within the overburden are important too; if the permeability is sufficiently large, brine that escapes from the salt dome can dissipate within the highly permeable layer where salt may precipitate. If, on the other hand, the permeability is low, it may be more favorable to release excess pressure of the cavity through fracking.

In order to give recommendations on avoiding undesired interference effects between caverns and salt dome boundaries, it is thus crucial to have a better understanding of how salt deformation-induced stresses vary within the salt dome and which lower/upper bounds to expect for a particular type of structure. Where are such stresses likely to be negligible, and can we safely use existing approaches that neglect the background stress field? To which extent do uncertainties in the model parameters and geometries of the external and internal layering affect the stress state in the salt dome? To which extent do deformation processes and fluid pressure changes in the overburden affect deformation within the salt?

The objective of this study is to review the literature on this subject and present the results of additional 3D simulations that incorporate the state-of-the-art rheological flow laws of salt and evaluate the stress state over approximately 300 kyrs.

2 Literature review

Much of the geodynamic and geomechanical literature on salt dynamics focusses on forward modelling of salt structures, typically for more generic cases (Albertz and Ings 2012; Fuchs, Koyi, and Schmeling 2014; Gradmann, Beaumont, and Albertz 2009; A.N.B. Poliakov, Podladchikov, and Talbot 1993), using 2D models and focusing on the geometric evolution of the salt structures. 3D models using purely viscous rheologies and density-driven instabilities have been around for some time (Fernandez and Kaus 2015; Ismail-Zadeh et al. 2004; Kaus and Podladchikov 2001), but they are a poor representation of the sedimentary overburden which behaves as (poro)-elastoplastic rocks. It is only very recently that numerical simulations have evolved to the stage where full 3D large-strain evolutionary models can be performed that take the nonlinear (visco)-elastoplastic rheological behavior of salt and sediments into account, together with tectonic deformation and sedimentation processes (Baumann, Kaus, and Eichheimer 2017). This required significant developments in the numerical models and solver techniques, thanks to which it is now possible to perform the simulations sufficiently fast to allow for parameter studies.

Most published scientific articles of stresses in and around salt domes do not show variations within the salt dome itself, predominantly because they are typically significantly lower than stresses within the overburden (whereas stresses in the overburden can be on the order of 50-100 MPa depending on the depth and tectonic deformation, stresses within the salt itself are on the order of 1-2 MPa), and are thus not visible if plotted with the same color scale. An alternative reason, however, may also be that the salt rheology behaves like a (nearly) incompressible viscous fluid whereas the overburden has a compressible (visco)-elastoplastic rheology. Modeling incompressible fluid flow is well-known to be notoriously difficult and requires the use of instable finite elements (which employ, for example, quadratic shape functions for velocity and linear, discontinuous shape functions for pressure). If linear quadrilateral or triangular finite elements are employed, one may obtain so-called checkboard

pressures within the incompressible fluid, which affects both the pressure and stress states (Gresho and Sani 2000; Pelletier, Fortin, and Camarero 1989; Popov and Sobolev 2008) but is typically less noticeable in the velocity and displacements fields. Similar effects are expected to occur in explicit, rather than implicit, modeling algorithms. It is difficult to estimate to which extent this effect played a role in not showing the intra-salt stress state in publications, as in most cases, insufficient details on the employed numerical scheme or the type of finite element are given. In some cases, dynamic pressures are shown [e.g., Figure 4 of (Nikolinakou, Flemings, and Hudec 2014)], but the patchiness of the plots suggest that either this effect played a role, or that the employed numerical resolution was insufficient. The stresses within the overburden are less affected by this issue, as the overburden rheology is elastically compressible, which is numerically easier to handle.

In this section, we give an overview of some constraints that exist for salt-dome scale variations of stresses and summarize existing numerical models.

2.1 Stresses within salt structures

2.1.1 Constraints from the microstructure

As explained in the report of phase 1 of this project (micro-scale processes), the size of salt subgrains can be used to estimate paleo-stresses in salt (Carter and Hansen 1983; Carter, Hansen, and Senseny 1982; Urai and Spiers 2007).

Such measurements have been performed, for example, the z2HS1 and z2HS2 layers within the Gorleben salt dome, which form the main salt layers of the dome, and resulted in differential stress estimates of 1.1-1.3 MPa (Thiemeyer et al. 2016). Their samples were obtained from a single tunnel within the Gorleben mine over a distance of around 200 m. Their results did not show a statistically significant variation of stresses with distance along the tunnel. Yet, their samples were taken at a location ~600 m below the top of the salt structure and at least several 100 meters away from the lateral sides of the salt body. The same research group obtained higher values of

up to ~3 MPa within Gorleben, but in this case from a high-strain domain in the vicinity of a dense anhydrite layer (Mertineit et al. 2014).

TABLE 2.1

Summary of paleo stress estimates from the salt microstructures for different localities. After (Thiemeyer et al. 2016).

Publication	Mean Differential stress [MPa]	Locality	Geological Setting
(Thiemeyer et al. 2016)	1.1-1.3	Gorleben (Germany)	Salt dome
(Desbois et al. 2010; Desbois, Urai, and de Bresser 2012)	3.1-4.8	Qom Kuh (Iran)	Salt fountain
(Kneuker et al. 2014)	1.2-2.9	Morsleben (Germany)	Salt dome
(Leitner et al. 2011)	2.0-5.4	Haselgebirge (Austria)	Rocksalt-mudrock-tectonite
(Mertineit et al. 2014)	2.28-2.97	Gorleben (Germany)	Salt dome
(Schléder and Urai 2005)	0.45-0.97	Hengelo (Netherlands)	Bedded salt
(Schléder, Burliga, and Urai 2007)	0.9-3.1	Klodawa (Poland)	Salt dome
(Schléder and Urai 2007)	1.4-2.0	Garmsar Hills (Iran)	Extrusive salt (protomylonite)
(Schoenherr et al. 2007)	<2.0	Birba, Haweel (Oman)	Salt diapir
(Závada et al. 2012)	3.8-4.8	Neuhof (Germany)	Folded salt

A compilation of stress values from different locations is given in Table 2.1 and shows that differential stresses estimated in this manner generally vary from ~0.5-5.5 MPa. The lowermost stress-estimates come from flat-lying salt layers in the Netherlands, whereas the higher estimates are from locations where the salt is strongly deformed

(such as in salt domes). However, no systematic compilation of paleo stress estimates with distance away from the side or top of salt domes has been published so far. As we will demonstrate in section 4, numerical models suggest that significant variations of stress magnitudes are expected to occur with salt structures, particularly closer to the salt-host rock contact zone. Future studies that address these microstructural analyses of samples at various points within the salt dome would thus be very helpful.

2.1.2 Constraints from in-situ measurements

Rocks salt is generally assumed to behave as a viscous fluid, and if this fluid is entirely at rest, the stress state should be isotropic, and differential stresses should be close to zero. Yet, as discussed in part 2 (cavity-scale models; section 1.1 and 1.2) of this study, it is less clear whether this is the case in actual salt domes as 1) salt is heterogeneous which may cause stress differences and 2) salt domes exhibit a significant density difference between salt and the depth-integrated average density of the surrounding host rocks which still causes (some) flow within the salt that induces stresses even if the salt structures no longer move at a high rate.

In-situ stress measurements within wells drilled through salt structures can be made but are not straightforward to perform as discussed in part 2 of this report (cavity-scale; section 1.2). Results reported in that section vary between having a nearly isotropic state of stress but at a higher pressure than estimated from integration density logs (Rummel, Fritz, Benke, Klaus, and Denzai, Klaus 1996), to cases within a salt dome in N. Germany where the minimum stress values are 1.0-1.5 MPa increased over the lithostatically expected value (Schreiner, Jäpel, and Popp 2004). The authors perform 2D numerical simulations to understand this effect better; results show that salt flow results in differential stresses (σ_1-σ_3) of 0.3 MPa or less, but that the increase in pressure is likely caused by the fact that higher-density sediments surround the dome.

These studies thus do not give clear evidence for differential stresses of significant magnitude within salt structures. It should, however, be noted that the stresses

estimated from the microstructural analyses are relatively small in magnitude compared to the overall values of pressure and that the hydraulic fracture tests may thus simply not have the accuracy to determine such differential stresses at sufficient accuracy.

2.1.3 Models of stresses within salt structures

The dynamics of salt structures has been studied in numerous 2D (Albertz et al. 2010; Schultz-Ela 2003; Albertz and Beaumont 2010; Chemia, Schmeling, and Koyi 2009; Albertz and Ings 2012; Allen and Beaumont 2012; Goteti, Ings, and Beaumont 2012; A.N.B. Poliakov et al. 1993; Kaus and Podladchikov 2001; Poliakov et al. 1996; A. N. B. Poliakov et al. 1993; Podladchikov, Talbot, and Poliakov 1993) and in a few 3D studies (Baumann et al. 2017; Baumann, Kaus, and Popov 2018; Fernandez and Kaus 2015; Ismail-Zadeh et al. 2004, 2004; Kaus and Podladchikov 2001), which mostly focus on forward modelling the geodynamic evolution of salt provinces. Yet, in nearly all cases, the focus of those simulations is on the geometric evolution of structures, or the stress state in the sediments surrounding the salt. Several modeling studies visualize stress states within salt bodies. However, there is no study that directly focusses on dome-scale variations of stresses within the salt dome and performs a systematic analysis.

A relatively well-studied problem is that of sinking stringers within the salt domes. In the Netherlands, these stringers are seismically well-imaged internal anhydrite and carbonate bodies within salt structures, some of which have been drilled (Strozyk et al. 2012, 2014; Van Gent, Urai, and de Keijzer 2011). As anhydrite layers have a higher density than the surrounding salt, they induce stress which depends on its volume V and density difference with the surrounding salt $\Delta\rho$ as

$$\sigma \propto \Delta\rho g V^{\frac{1}{3}} \tag{2.1}$$

So, for a stringer that has an equivalent size of ~100^3 m^3 and a density difference of 700 kg m^{-3}, dimensional analysis suggests stresses on the order of ~0.70 MPa. These results are in reasonable agreement with stresses compute in numerical models of (S. Li et al. 2012), which are reported to decrease from ~ 1 MPa at the onset of deformation

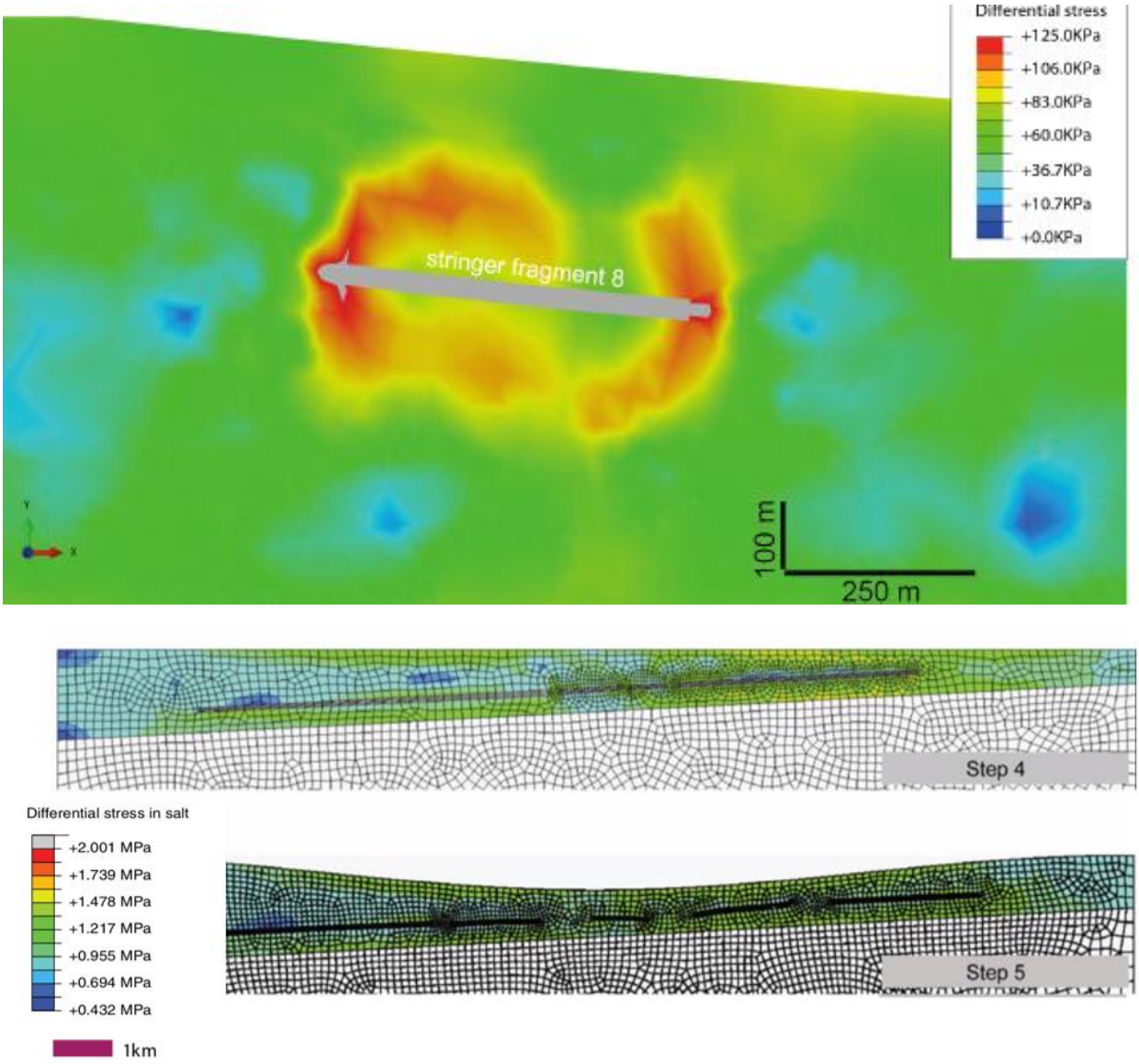

FIGURE 2.1

Left: Differential stresses around a sinking stringer embedded in salt with a non-Newtonian rheology Top: (S. Li et al. 2012), Lowermost snapshots: (Shiyuan Li et al. 2012).

until 0.15 MPa at a later stage (Figure 2.1). Within the stringer itself, stresses can be significantly larger, which may be caused by bending and folding of layers, which can cause significantly larger bending stresses [see, for example (Schmid, Podladchikov, and Marques 2004)].

Others have studied the sinking of anhydrite blocks in salt domes as well (Adamuszek and Dabrowski 2019; Burchardt et al. 2012; Koyi 2001; Li, Urai, and Zhang 2017), but predominantly focused on the geometrical evolution and did not discuss the stress distribution within the salt.

As discussed in phase 1 of this project, there is a considerable discussion on what the long-term rheology of salt is. Evidence for both pressure-solution and power-law creep exists from field examples, microstructural analysis, and laboratory experiments. However, as experiments are performed at higher deformation rates and stresses than geological conditions, the flow laws determined in this manner must be extrapolated over a wide range of scales from experimental to geological conditions. An alternative method, therefore, uses direct geological observations to put bounds on the parameters. One important method is the observation from salt layers in the Netherlands that stringers of anhydrite have not sunk significantly since the Permian, despite their high density.

To first order, the sinking velocity v_{sink} of the stringer can be estimated by using the Stokes sinking velocity of a sphere

$$\mathrm{v}_{sink} \propto \frac{2}{9}\frac{\Delta\rho g \mathrm{V}^{\frac{2}{3}}}{\eta_{eff}} \tag{2.2}$$

Where η_{eff} is the effective viscosity of the surrounding salt, and V the equivalent volume of the sphere.

Note that corrections of this expression exist for the case of a spherical inclusion sinking in a power-law fluid (Weinberg and Podladchikov 1994), and for the cases in which the geometry is non-spherical (Happel and Brenner 1983), which reduces the sinking velocity.

Using the values employed, combined with a salt viscosity of 10^{17} Pas, gives a sinking velocity of 4.9 mm/year, implying that the stringers would sink to the bottom of a 5 km thick layer within a million years. Given that in the Netherlands, stringers are still located towards the top of flat-lying salt layers suggests that the sinking velocity must

have been significantly lower. (Van Gent et al. 2011) suggest, based on seismic data, that the maximum sinking velocity cannot have been higher than ~0.004 mm/year in the Netherlands. This can be explained by an effective (linear) salt viscosity of 10^{20} Pas or higher (Burchardt et al. 2012). Alternatively, (S. Li et al. 2012) used 2D numerical models to simulate this situation and conclude that non-Newtonian salt rheology can explain the observations, suggest that pressure solution is ineffective under these conditions. They speculate that this may be because, under low differential stresses, fluid films at grain boundaries become arrays of fluid inclusions which lowers grain boundary diffusivity and thus effectively shuts down the pressure solution creep mechanism.

Yet, stringers rarely occur in isolation, but rather in arrays of blocks that are located reasonably close to the boundary of salt structures. Both the vicinity to the boundary and the arrangement reduces the sinking velocity. (Adamuszek and Dabrowski 2019) show that this, under certain conditions, may be sufficient to explain the observations. 3D geometries and the fact that stringers also often occur between different types of salt (which have different effective viscosities) have not yet been taken into account in this analysis, which may further reduce the sinking velocity.

To address the question of what the long-term rheology of salt is, it would thus be essential to perform additional work that employs 3D dynamic models, observed salt and stringer geometries from 3D seismic observations (Strozyk et al. 2012, 2014; Van Gent et al. 2011), and variations in the salt rheology of the salt and compares it with measured deformation rates to test which rheologies fit the observations best. At the same time, we also need a much better understanding of the well-documented occurrence of vertical anhydrite layers such as in Gorleben. Why did these layers not sink, and under which conditions and with which rheologies can we explain how they became vertical?

First studies addressed this in 2D and with linear viscous salt rheology (Chemia and Koyi 2008; Chemia, Koyi, and Schmeling 2008) and demonstrated that it there is a fine balance between sedimentation rates and (linear) salt viscosities that would explain a Gorleben-like salt wall which includes vertical anhydrite layers. Yet, to which extent

this is valid for realistic sedimentation rates (reconstructed from the surrounding sediments) and for 3D geometries remains to be studied.

(Koyi 2001) was among the first to point out that the occurrence of anhydrite layers within the Gorleben salt dome may be potentially hazardous as the blocks may continue sinking even when the salt dome stops growing (as is the presently the case). Of course, the sinking velocity depends on the employed creep law, and whereas the original study employed a linear viscous creep law with a viscosity of 10^{18} Pas, a later study took non-Newtonian creep of salt into account as well (Chemia et al. 2009). They presented several scenarios, starting with the geological model of the present-day structure of Gorleben. Their model results show that if the effective viscosity becomes smaller than around 10^{18} Pa s, the anhydrite starts sinking noticeably, and would likely not have formed vertical layers in the first place (Figure 2.2). For higher values of effective viscosity, sinking velocities are lower. In all cases, stress, dome-scale stress variations occur, which are on the order of MPa with the highest stress values within in the anhydrite layers.

More recently, 3D numerical models of the present-day deformation of Gorleben were presented in which the effect of salt rheology was explored, but the internal layering of the salt and the effect of anhydrite layers was not taken into account (Baumann et al. 2018). The results show that considerable variations in strain rate within the salt are expected to occur and that vertical velocities at the exploration level are slightly higher than observed rates of ~0.07 mm/year. These results are not all that sensitive to variations in the employed salt rheology, or whether only the Gorleben salt structure is taken into account or also the neighboring salt diapirs (Figure 2.3).

The fact that strain rates vary within the salt wall suggests that stresses vary in a similar manner. However, whereas the orientation of the maximum principal horizontal stress was visualized in their models, they did provide a systematic analysis of the stresses within the salt domes apart from stating that it varies between 1 and 3 MPa at the exploration level.

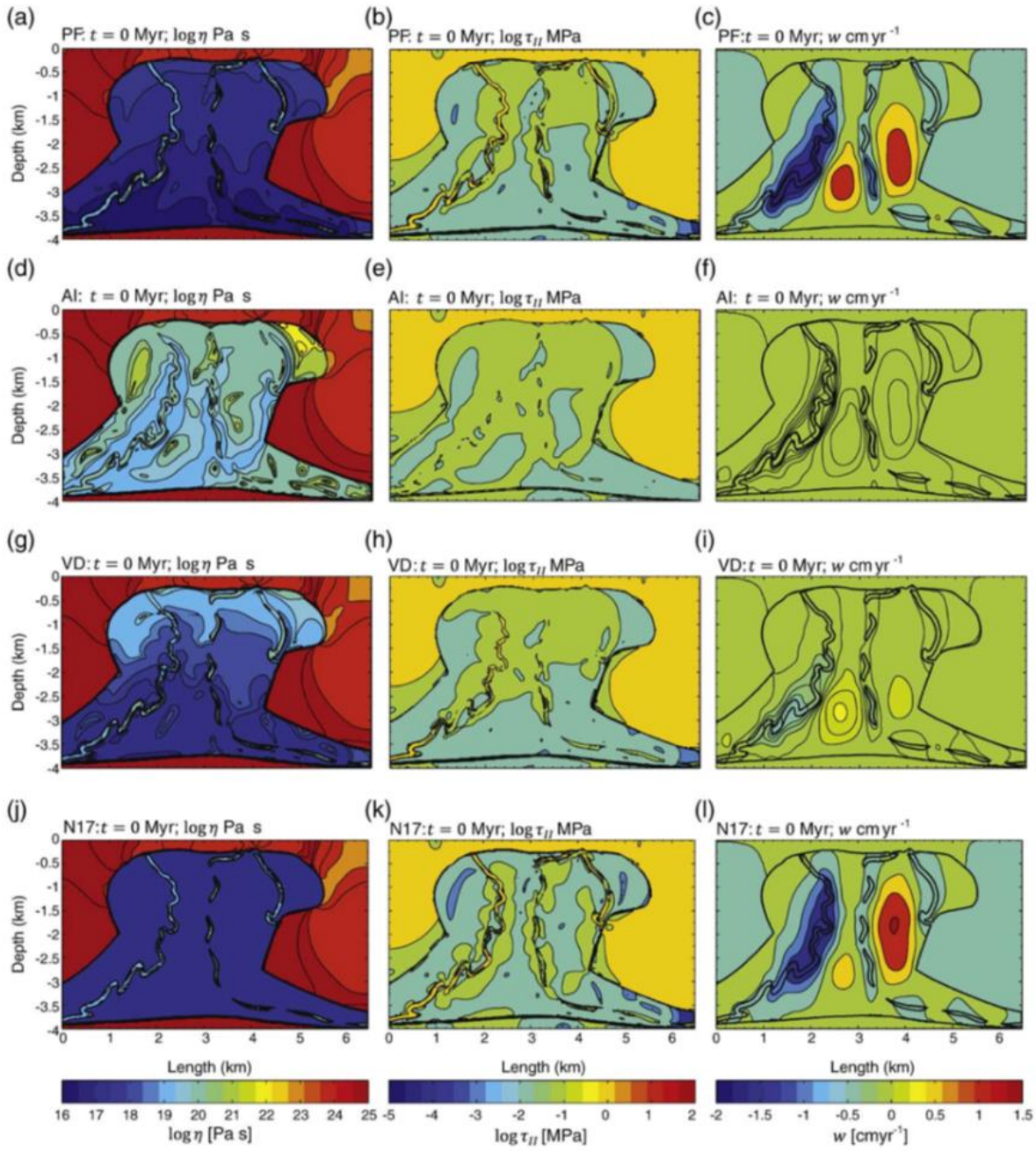

FIGURE 2.2

2D numerical simulations of scenarios of the Gorleben, starting with the present-day reconstructed geological structure and for different salt rheologies, while the overburden. The left column shows the effective viscosity, the middle column, the second invariant of the deviatoric stress tensor (which is half the differential stress) on a logarithmic scale, and the right column the vertical flow velocity. Four different scenarios are shown: PF: mildly non-Newtonian rheology (n=1.39), AI: non-Newtonian with n=4.10, VD: non-Newtonian with n=2.2, N17: Newtonian rheology with a viscosity of 10^{17} Pas. Taken from Figure 4 in (Chemia et al. 2009).

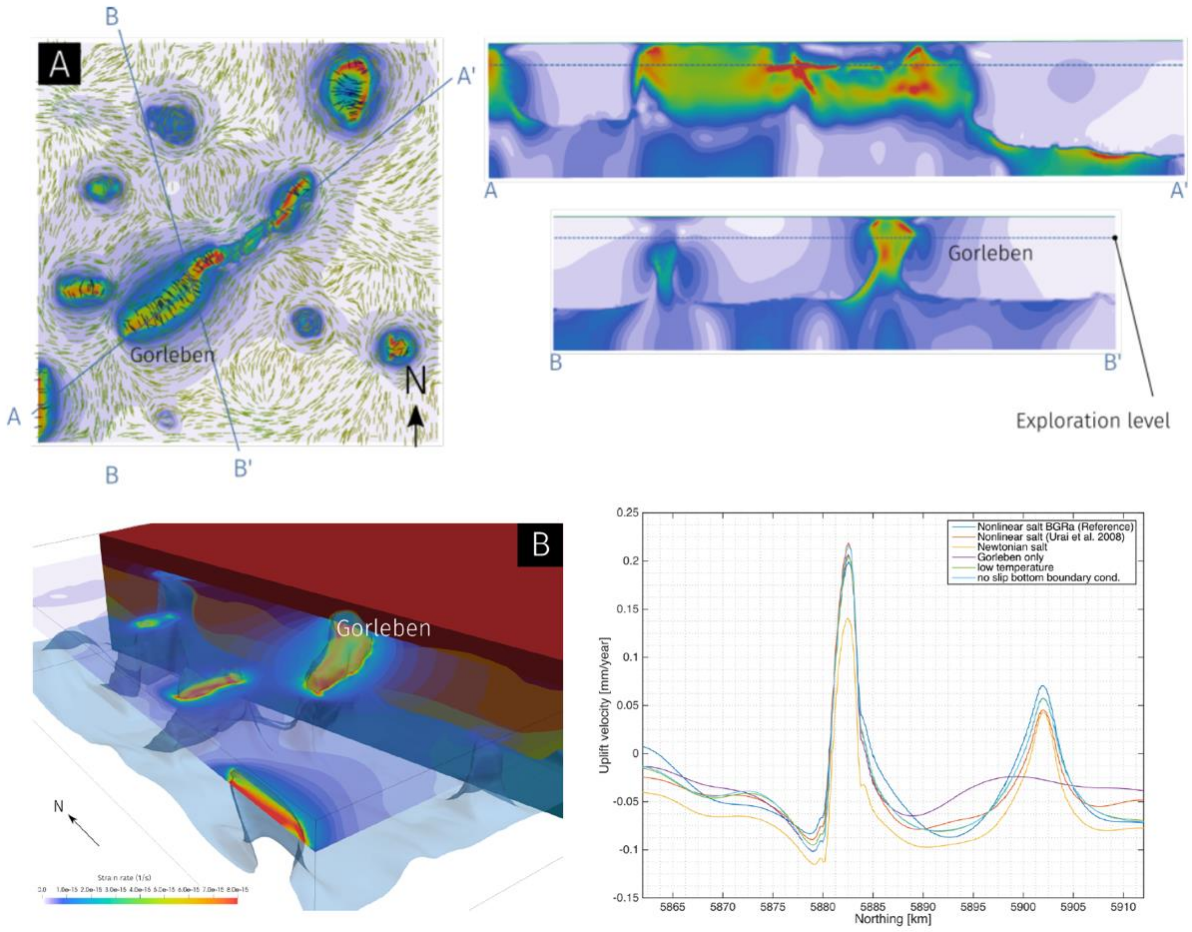

FIGURE 2.3

Strain rate deformation rates in a 3D model of the Gorleben structure, which show that significant variations in the strain rate within the salt occur, even when internal mechanical layering of the salt and the presence of anhydrite layers are not taken into account. From (Baumann et al. 2018).

In order to study the impact of salt flow on drilling campaigns through salt sheets, Weijermars and coauthors developed an analytical model in a series of papers to simulate the motion of salt sheets by considering analytical end-member models of Couette and Poiseuille flow (Weijermars 2015; Weijermars et al. 2015; Weijermars and Jackson 2014). In (Weijermars and Jackson 2014), the authors state that "shear stresses caused by ductile creep in salt bodies may reach 100 MPa" (page 912). Yet, these estimates are based on analytical calculations, for rapidly moving salt sheets flowing down a continental slope (which may be applicable, for example, for the Gulf of Mexico), and no field evidence is given that stresses of similar magnitude indeed occur (even

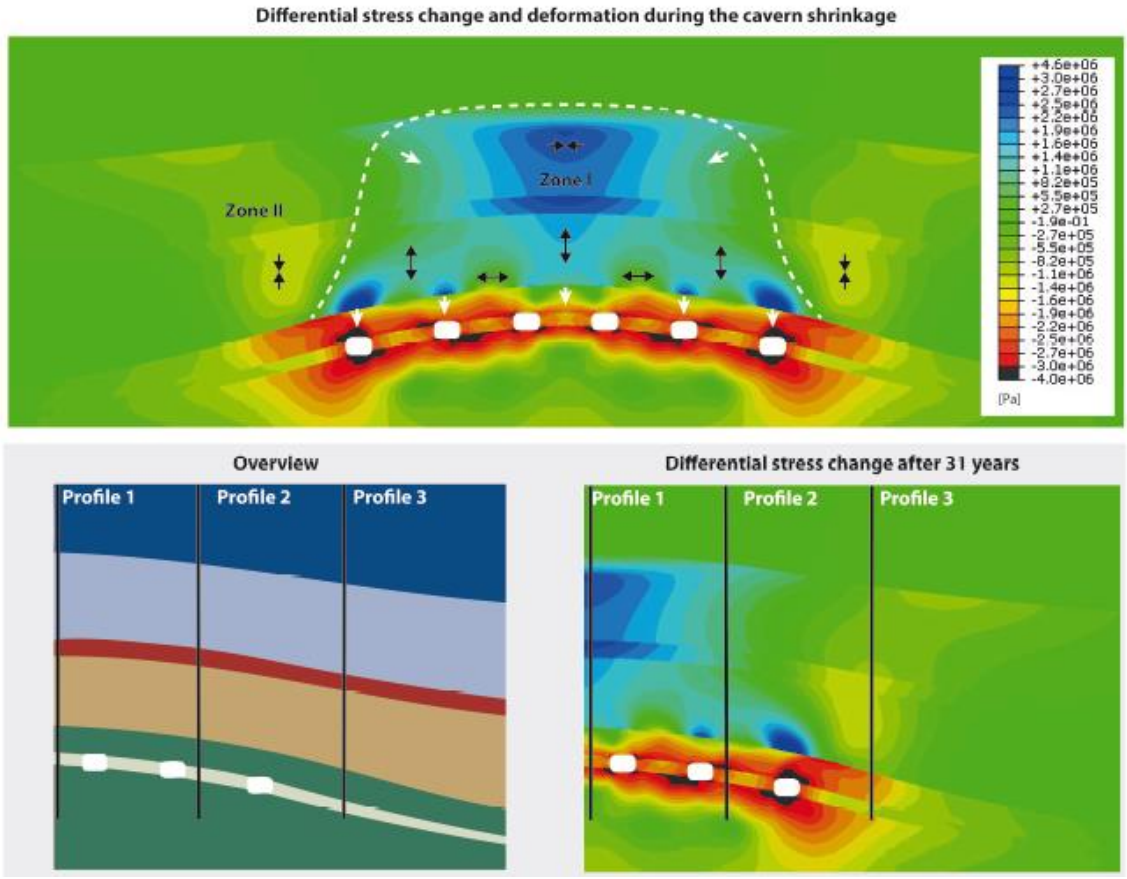

FIGURE 2.4

Stresses induced by cavity excavation of a K-Mg salt layer within a halite salt layer, in an idealized salt dome that is constructed to mimic the situation of the Veendam salt structure. Results show that this induces stress variations on the order of 4 MPa, after around 30 years. The differential stress in the overburden is reduced as a result of salt mining. Density heterogeneities within the salt are not taken into account, and the overburden is assumed to behave elastically. From Figure 7 of (Raith and Urai 2018).

though we note that well-hole collapse is a frequently occurring phenomenon while drilling through salt). Flat-lying salt or even salt domes in the Netherlands are mechanically much less active, and it is therefore unlikely that stresses of similar magnitude are to be expected here. Moreover, (Weijermars and Jackson 2014) do not provide field evidence that stresses of such magnitude indeed occur.

(Raith and Urai 2018) performed 2D axisymmetric finite element simulations to study the stability of faults above the Veendam structure in the Netherlands as a result of squeeze mining of a cavern field (Figure 2.4). Their models take differences in the

mechanical strength of salt, a nonlinear dislocation-creep salt viscosity, as well as the internal cavities into account, and simulate the stress state as a result of cavity mining. Results show that subsidence, as a result of cavity mining, will reduce the differential stress in the overburden and thus makes it less likely that preexisting faults will be reactivated. Their models also suggest that expected stress variations within the salt are several MPa in magnitude and that stress localization within the weaker K-Mg salt layer is slightly smaller.

(Bruno, Ramos, and Lao 2017) employed geomechanical models to compute the stress heterogeneities caused by the presence of cavity and shows that significant risks exist if the distance of the cavity to the salt dome boundary is less than the radius of the cavity. Yet, their models assumed the salt to be homogeneous and initially stress-free. Deviations of this due to large-scale deformation processes within the salt structure may dramatically affect this “safe-distance,” and it is thus essential to have more realistic estimates on how significant these stresses may be.

The effect of glacial periods on stresses within salt structures is a factor that may be relevant for salt structures in Northern Europe. In (Schreiner et al. 2004), this effect was modeled by adding a load for a limited time, which was subsequently removed. Results show that the effect of the ice load is nearly but not completely recovered (Figure 2.5), a fact that is likely to depend on the salt viscosity.

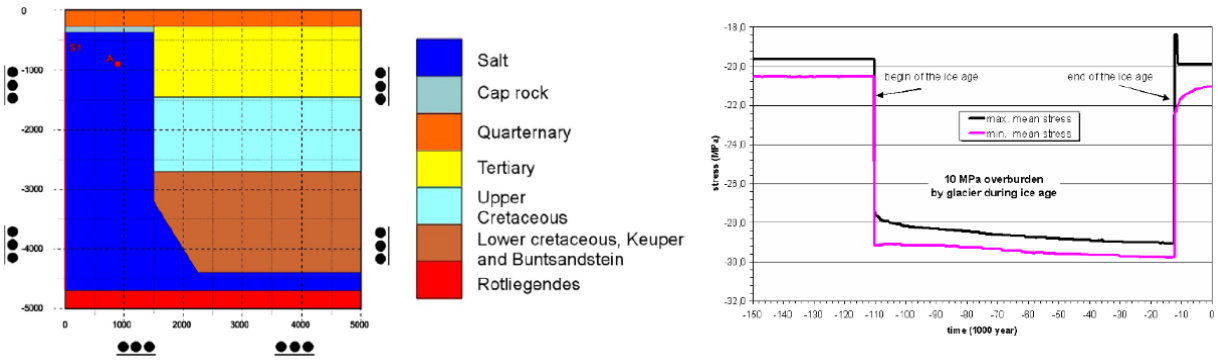

FIGURE 2.5

Idealized, 2D model of a salt dome above which a load is added to mimic a glacial period. The right figure shows the temporal evolution of the minimum/maximum stresses at point A (red dot at the left), which illustrates that the effect of the glacial period it mostly recovered at the present day (Schreiner et al. 2004).

2.2 Stresses around salt structures

2.2.1 Numerical models

Most published work on stresses related to salt tectonics focusses on the state within the surrounding sediments (Baumann et al. 2018; Luo et al. 2012, 2012, 2017; Mossop 2012; Nikolinakou et al. 2012; Nikolinakou, Flemings, et al. 2014; Nikolinakou, Hudec, and Flemings 2014; van der Zee et al. 2011), or on the geomechanical stability of salt mines (Eickemeier et al. 2013).

Compared to the elastoplastic host rocks, stresses within the salt are significantly smaller such that the salt-sediment boundary is nearly a 'stress-free' boundary, just like the Earth surface (Zoback 2010). This causes a rotation of the principal stress direction such that it is (nearly) perpendicular to this interface, which significantly affects the state of stress around salt structures. These effects can be challenging to deal with if drilling through salt, and given the costs of well-hole collapse, quite a bit of effort went into creating numerical tools with which this situation can be simulated. In most cases, a detailed computation is required that can be calibrated with stress measurements in the overburden, if available.

An example of such a modeling study is shown in Figure 2.6, in which 3D finite models of stresses around complex salt structures are performed (van der Zee et al. 2011). In this model, the sediments are assumed to behave poroelastic, but plastic effects of the rocks are ignored, which may be a valid approximation if the overburden does not exhibit active faults. Results show that the stress distribution can be rather complex, which is non-trivial is planning drilling campaigns. Simulations around the Gorleben salt structure are presented in Figure 2.3a and suggest that the principal stress directions are indeed strongly influenced by the presence of salt structures (Baumann et al. 2018; King et al. 2012).

In order to understand the importance of the rheology of the sediments on the expected stresses in the overburden, (Luo et al. 2012) compared numerical models that include poroelastic effects with models that include brittle failure and plasticity as well, for idealized salt models. The results suggest that taking plasticity into account is crucial as purely elastic models significantly overestimate stresses. In a related study, they show that fully coupled models in which pore-pressures builds up as a result of salt deformation is an important factor as well and can result in localized overpressure within the sediments (Nikolinakou et al. 2012).

In (Nikolinakou, Hudec, et al. 2014), they compare stresses obtained from quasi-static models (based on the present-day geometry of salt structures) versus models in which the fully coupled geomechanical evolution of a salt dome was taken into account. The results show that there are significant differences in the stress magnitudes, which are larger in the evolutionary models. Yet, performing realistic evolutionary models of a specific region that are coupled with poroelastic effects also requires exact constraints on the fluid flow properties of the rocks and how it evolved with stress. Moreover, whereas these effects are pronounced in the poroelastoplastic overburden, where stresses do not relax fast, they may be much less pronounced within the salt dome itself, where the viscoelastic relaxation time of the rocks is significantly smaller.

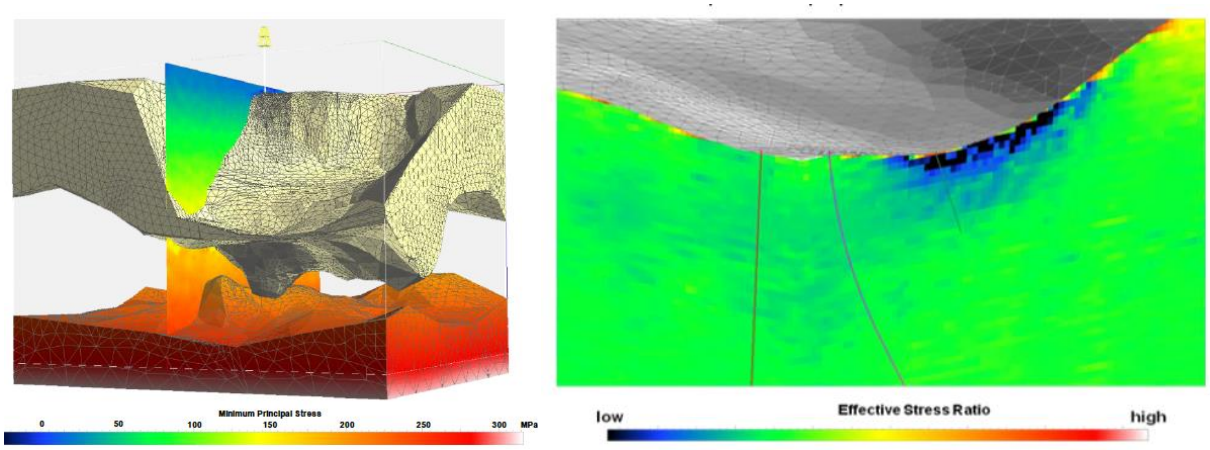

FIGURE 2.6

Example of a 3D numerical simulations of stresses around a salt sheet, showing the minimum principal stress (left) and the effective stress ratio (defined as $(\sigma_1 - P_f)/(\sigma_3 - P_f)$) below a salt sheet (right). Drilling experience showed that no significant problems occurred in the red well on the left, whereas major loss problems were encountered in the green well that traversed the low effective stress region. Figures from (van der Zee et al. 2011).

A recent compilation of stress measurements from boreholes in the northeast of the Netherlands, for example, illustrated that anomalous stress orientations occur in the vicinity of salt structures (Mechelse 2017). The precise amount by which stresses deviate depends on the rheology of the salt and sedimentary overburden, the pore-fluid pressure, the regional stress field, and the geometry of the salt structure. Detailed calculations are thus required to get a better estimate of the stress and its uncertainties. So far, the relationship between stresses in the overburden, which behaves (poro)elastoplastic, and viscous creep within the salt structures, is unclear. Moreover, in the Netherlands, the effects of the last glaciation, which added and removed weight, may still have a non-negligible effect on the stress-state in the overburden and perhaps on salt flow.

As this summary shows, stresses vary in a non-trivial manner in sedimentary basins around salt structures, and there are no simple rules of thumb that can be used. Instead, detailed calculations must be performed for a particular scenario, which should ideally take the following ingredients into account:

- Employ an incompressible viscous flow law for salt taking both pressure solution, and dislocation creep into account as well as reasonable parameter variations for each flow law.
- Model the overburden as a poro-elastoplastic material. Using a plastic flow law is particularly important in regions that show evidence of faults irrespective of whether they are still active or no longer deform (as stress relaxation from the plastic yield stress takes a long time for elastic materials).
- Use detailed geometries, including rheological changes within the salt.
- Perform the study in 3D.
- Take reasonable variations in material parameters into account, rather than relying on a single scenario.

Given the rapid advances in (parallel) geomechanical software that has been made over the last decade or so, it is feasible to do this.

2.3 Effect of differential stresses within salt on cavity and hole closure

Most models of cavity closure assume that the surrounding salt is static and that there are thus no pre-existing stresses. However, the fact that salt forms large-scale subsurface structures shows that it has deformed on geological timescales. This deformation may be ongoing today, albeit at a slow rate, and for viscous material, deformation will induce stresses. The main question is whether the magnitude of these stresses is sufficiently large to be of concern for the abandonment of cavities or for drilling campaigns through salt or whether it can be safely ignored.

Interestingly, there are only a few studies that address this topic. A series of papers by Cornet and coworkers addresses this problem in the context of the closure of holes within nonlinear viscous and viscoelastic rocks (Cornet and Dabrowski 2018; Cornet, Dabrowski, and Schmid 2017, 2018b), and derive new analytical expressions for this case.

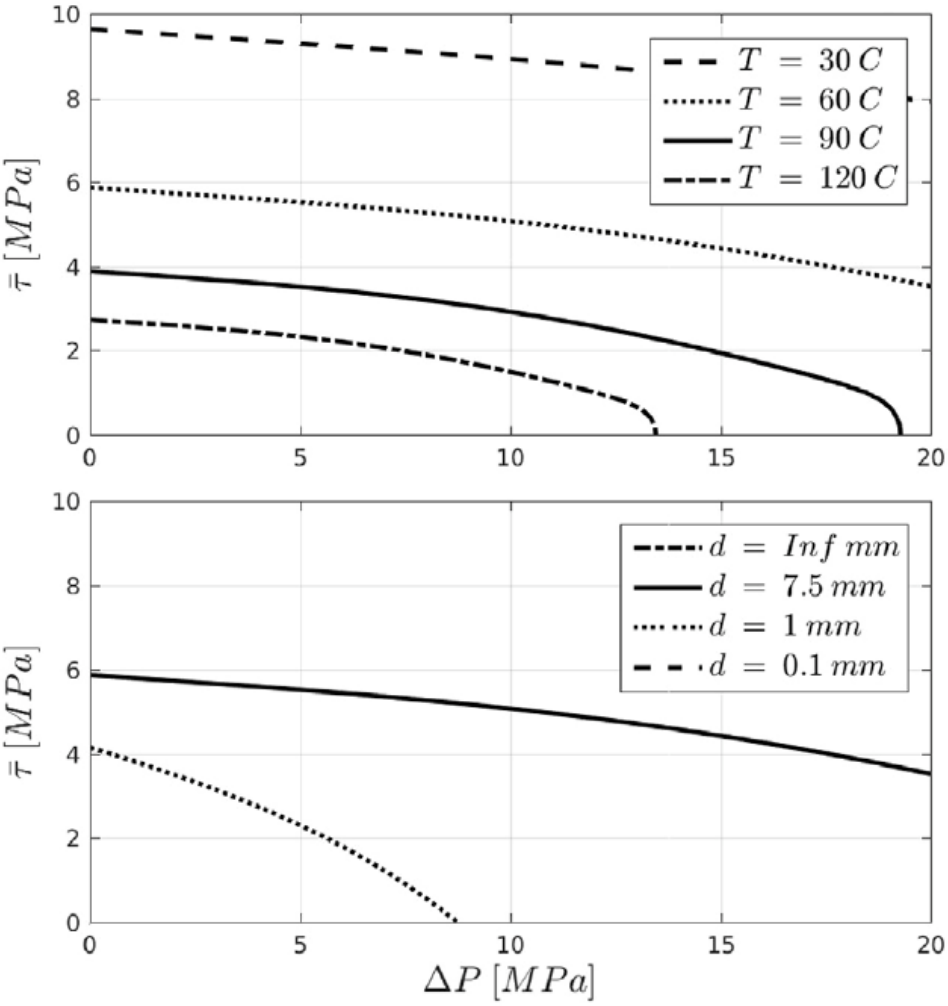

FIGURE 2.7

Load configurations required to reach a 10% rate of deformation per year for different temperatures as a function of far-field increase in pressure *vs.* shear stress for different a) temperatures and b) grain sizes (Cornet et al. 2018b). The effect of shear stress is more significant than that of an increase in pressure.

(Cornet et al. 2018b) employ a combined dislocation and pressure-solution creep law for the salt, similar to what we use in the models described in section 4, and study the effects of various parameters including that of non-zero stress within the salt on the closure velocity of the hole. They write that "*In the power-law regime, hole closure is almost n (stress exponent) times more sensitive to shear than pressure loads, demonstrating the necessity of considering far-field shear stresses for hole closure in*

applications going through moving salt bodies" (page 104), which is illustrated in Figure 2.7 and Table 2.2 and confirms their earlier results (Cornet, Dabrowski, and Schmid 2016). Physically, this can be understood because the effective viscosity of a nonlinear viscous material decreases with increasing deviatoric (or differential) stresses. Larger stress thus lowers the shear viscosity which increases the deformation and hole closure rate.

If, in addition, one also includes the effect of pressure solution, which is a strongly grain size dependent rheology (as discussed in more detail in Chapter 3), the behavior becomes non-trivial, and the two creep mechanisms may interact in an area around the hole or cavity. (Cornet et al. 2018b) and (Cornet et al. 2017) develop approximate analytical solutions for this case and point out the importance of including pressure solution as well in cavity closure models. They conclude that

"The influence of grain size dominates over all other parameters such as temperature or dislocation creep parameters. The difference in closure rates between coarse- and fine-grained salts can reach several orders of magnitude and significant hole closure can be attained in less than one day in very fine-grained salts. Given that grain size may vary considerably within the same salt body, closure rates may also be very different and it is important to characterize the range of grain sizes at the location of the hole."

They also write that:

"Best practices to prevent hole closure include increasing hole pressure, decreasing temperature, and avoiding as much as possible moving, fined-grained rock salts, where pressure solution is active.

For sealing applications, fast hole convergence can be achieved by choosing a warm, moving, fine-grained salt and using a pressure difference as large as possible. Great depths where temperatures and pressure differences are high should be preferred. Using in addition water as a pressurizing fluid can promote pressure solution and lead to increased closure rates." (page 105)

What is important in this context is that the approximate solution presented in their work is valid for cylindrical holes and does not take heterogeneities or complexities such as its the vicinity to the salt-host rock boundary into account. Whereas it is certainly a useful first-order estimate, a more detailed case study would be important to be made the expected ground subsidence as a result of the full closure of a deep cavity. Moreover, microstructural analysis is, in principle, capable to determine in which creep regime rock salt has deformed. Repeated sonar studies of the cavity shape can potentially be used to calibrate cavity closure models, which is useful to make more precise predictions of its long-term behavior.

TABLE 2.2

Time in years required to reach a 10% hole closure for three different loading configurations (with either a far-field pressure increase ΔP or a far-field increase in shear stress $\tau^{far\text{-}field}$) and grain sizes for a cavity within a viscous salt that deforms by pressure-solution and dislocation creep a 660 °C according to (Cornet et al. 2018b)

Grain size [mm]	**ΔP=5 MPa, $\tau^{farfield}$=0 MPa**	**ΔP=5 MPa, $\tau^{farfield}$=2 MPa**	**ΔP=10 MPa, $\tau^{farfield}$=0 MPa**
Infinite	5500	50.0	243
7.5	297	49.5	45
1	1.97	1.07	0.833
0.1	$2.1x10^{-3}$	$1.2x10^{-3}$	$1.0x10^{-3}$

2.4 Summary

There is relatively little information about the stresses that are expected to occur within salt structures as a result of tectonic deformation of salt. An analysis of stresses from the microstructure seems to suggest that stresses are generally around 1 MPa, with lower values occurring in flat-lying salt layers and higher values occurring in salt domes, close to anhydrite layers and in the vicinity of strongly deformed part within the salt domes. However, there are only a few studies, and there is no study that systematically measures stresses with distance away from the salt/wall-rock contact area.

Whereas differential stresses of < 0.01 MPa are unlikely to be of major concern for the construction of salt cavities, this is not the case for stress values of ~0.5-1 MPa, which may affect the closure of salt cavities, depending on what the salt rheology is. Estimates of stress magnitudes from estimating natural rocks thus do not exclude this from occurring.

Published numerical models on the dynamics of salt structures predominantly focus on the external dynamics of salt domes, on the geodynamic evolution of salt structures, or on stresses surrounding salt structures. In a few cases, plots of the stress distribution within the salt are shown, which suggest that stress magnitudes can be quite heterogeneous.

The literature on stresses magnitudes and orientations within salt structures is thus not entirely conclusive. In particular, we need more information about how stresses in salt are distributed as a function of geometry (flat-lying salt, pillows, or salt walls), and as a function of salt rheology.

For this reason, in the current report, we have performed additional systematic, 3D, geomechanical simulations of salt dynamics using realistic geometries and for a range of salt rheologies.

3 Salt rheology

Accurate prediction of differential stresses and deformations occurring within and around natural salt bodies, such as pillows or domes, requires a thorough understanding of the rock salt rheology. In other words, we need to build a model of how rock salt flows under externally applied stresses. Yet, the rheological behavior of rock salt is quite complex. On a short time scale, at shallow depths and low temperatures, salt can exhibit brittle and elastic deformations. However, on a long-term geological time scale, salt typically does not sustain significant differential stresses, as indicated by the sub-grain paleo-piezometers (Schléder and Urai 2005). Hence, its rheological behavior is termed to be viscous, which implies that any differential stress built up by a slow tectonic deformation will generally dissipate in a relatively short time scale if deformation ceases. On a microscopic level, the viscous deformation of salt is attributed to the cross-slip and climb-controlled dislocation creep mechanisms (Spiers et al. 1990). It was also reported that if salt contains brine, which is quite typical for natural conditions, the deformation mechanism is drastically changing. The dislocation creep is substituted by the fluid-enhanced dynamic recrystallization, and grain boundary diffusion creep, also known as the pressure solution creep (Urai et al. 1986). On a macroscopic level, these two creep mechanisms possess different phenomenological description. The dislocation creep is defined by a power-law dependence between the strain-rates and differential stresses (non-Newtonian creep), while pressure solution creep is built upon a linear relationship (Newtonian creep). The latter is, however, strongly dependent on the mean grain size (Spiers et al. 1990).

Despite that considerable progress has been made in recent decades in laboratory experiments (Spiers et al. 1990), (Ter Heege, De Bresser, and Spiers 2005b), (Berest et al. 2019), and microstructural studies (Urai et al. 1986), (Schléder and Urai 2005), the details of salt rheology remain a controversial issue. The problem is primarily related to the inability to reach low deformation rates in the laboratory, that would mimic slow

geological conditions. Hence to obtain a meaningful insight into the geological regime, it is necessary to extrapolate laboratory data to low geological strain rates. How reliable this extrapolation is, remains a question. Recently (Berest et al. 2019) reported the results of in-situ creep experiments in the low-stress regime. Their results show considerable underestimation (7-8 orders of magnitude) of the measured strain rates compared to the extrapolated predictions from the relatively high-stress laboratory measurements. Based on the obtained data, it was advocated that pressure solution creep might be the dominant mechanism under the low-stress regime. If we consider a combination between the dislocation and pressure solution creep from a mechanical viewpoint, as shown in the next section, it becomes clear that the transition between them will depend strongly on the mean grain size. Yet, the grain size itself will also be affected by the fluid-assisted dynamic recrystallization, leading to a rather complex interplay between the creep mechanisms (Urai and Spiers 2007). The exact understanding of which parameter combination triggers the onset of dynamic recrystallization remains mostly unknown in the state-of-the-art literature.

3.1 Review of Creep Laws

The macroscopic phenomenological description of the rock salt creep mechanisms can be summarized in the following functional form:

[1] Dislocation (power-law) creep (Urai et al. 2008):

$$\dot{\varepsilon}_{dc} = A_{dc}\,\sigma^{n} \qquad A_{dc} = B_{dc}\exp\left(-\frac{Q_{dc}}{RT}\right) \tag{3.1}$$

[2] Pressure solution creep (Spiers et al. 1990):

$$\dot{\varepsilon}_{ps} = A_{ps}\,\sigma \qquad A_{ps} = \frac{B_{ps}}{T\,d^{3}}\exp\left(-\frac{Q_{ps}}{RT}\right) \tag{3.2}$$

Here σ is the differential stress norm, *T* the absolute temperature, *R* = 8.314 J $mol^{-1}K^{-1}$ the gas constant, *B* the pre-exponential constant, *Q* the activation energy, *n* the power-

law exponent, and *d* the mean grain size. The total creep strain rate is equal to the sum of strain rates of individual creep mechanisms:

$$\dot{\varepsilon} = \dot{\varepsilon}_{dc} + \dot{\varepsilon}_{ps} \tag{3.3}$$

An alternative definition of the dislocation creep is given by (Wawersik and Zeuch 1986), (van Keken et al. 1993):

$$\dot{\varepsilon}_{dc} = D \exp\left[-\frac{Q_{dc}}{RT}\left(\ln\frac{\tau_0}{\mu_0} - \ln\frac{\sigma}{\mu}\right)\right] \tag{3.4}$$

where *D* is the pre-exponential constant, τ_0 and μ_0 the flow stress and shear modulus at absolute zero, and μ the average shear modulus. This definition can be rearranged to a standard power-law form with the following temperature-dependent exponent (van Keken et al. 1993):

$$\dot{\varepsilon}_{dc} = A_{dc}\, \sigma^n \tag{3.5}$$

where the power-law exponent and the pre-exponential constant, respectively, are given as follows:

$$n = \frac{Q_{dc}}{RT} \tag{3.6}$$

$$A_{dc} = D \exp\left[-n \ln\frac{\tau_0}{\mu_0}\right] \mu^{-n} \tag{3.7}$$

Determination of the rheological parameters for the rock salt creep mechanism has been the subject of numerous previous studies (Spiers et al. 1990), (Bräuer et al. 2011a), (Wawersik and Zeuch 1986), (Ter Heege, De Bresser, and Spiers 2005a). Table 3.1 summarizes the rheological parameters systematically employed in this report.

Instead of fixing the parameters for each creep mechanism, we consider different creep experiments and investigate the resulting differences. Figure 3.1 shows a comparison between the dislocation creep parameters for the rock salt employed here. The experiments are in rather good agreement. At given temperature and differential stress, all considered creep laws give strain rate predictions that usually show

variability within an order of magnitude. Nevertheless, the difference between the experiments is significant. Therefore, it is essential to test the influence of changing the rheological parameters on the simulated stress and deformation fields.

Along with stress modeling in natural salt bodies, we also consider how anhydrite layers, the so-called “stringers” (Li and Urai 2016), influence the stress balance. This requires a parametrization of the anhydrite rheology. (Briegel and Müller 1978) reported that anhydrite typically deforms by the dislocation creep mechanism with a rather small power-law exponent of $n = 2$, even though the overall mechanical response of the anhydrite layers is much stronger compared to that of rock salt (due to differences in the pre-exponential constant). The anhydrite creep parameters are also summarized in Table 3.1.

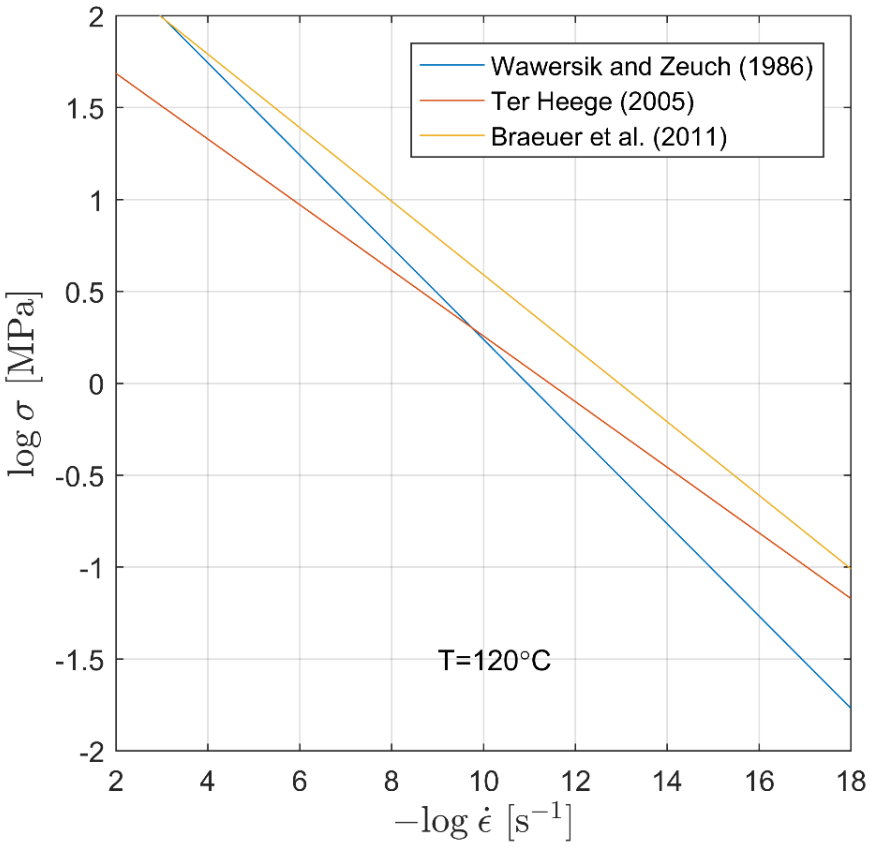

FIGURE 3.1

Comparison between dislocation creep parameters resulting from various creep experiments, using a logarithmic ($\log_{10}$) scale.

A typical combination of the dislocation creep (Wawersik and Zeuch 1986), and pressure solution creep (Spiers et al. 1990) with reasonable grain size (e.g., *d* = 1cm) results in a smooth transition shown in Figure 3.2. As expected, dislocation creep is active in the high-stress regime, while pressure solution creep is dominant in the low-stress regime. The influence of temperature is moderate. Note that for the dislocation creep described by (Wawersik and Zeuch 1986), the effective stress exponent is temperature-dependent. Hence on a log-log plot, slopes of the dislocation creep branch are slightly different. For other creep mechanisms, e.g. (Ter Heege et al. 2005b), this effect is not present.

TABLE 3.1

Rheological parameters of salt and anhydrite used in this report.

Parameter	Unit	Salt-PS[1]	Salt-DC[2]	Salt-DC[3]	Salt-DC[4]	Anhydrite-DC[5]
B	$Pa^{-n} \cdot s^{-1}$	$1.87 \cdot 10^{-19}$	-	$6.91 \cdot 10^{-36}$	$5.21 \cdot 10^{-37}$	$3.23 \cdot 10^{-11}$
D	s^{-1}	-	5.1	-	-	-
Q	$J \cdot mol^{-1}$	24530	14020	80000	54000	152260
n	-	1	-	5.6	5	2
τ_0 / μ_0	-	-	0.06	-	-	-
μ	Pa	-	$1.4 \cdot 10^{10}$	-	-	-
d	m	0.005 - 0.2	-	-	-	-

Legend:

PS – pressure solution creep

DC – dislocation creep

1 – (Spiers et al. 1990)

2 – (Wawersik and Zeuch 1986)

3 – (Ter Heege et al. 2005b)

4 – (Bräuer et al. 2011a) (BGRa Creep)

5 – (Briegel and Müller 1978)

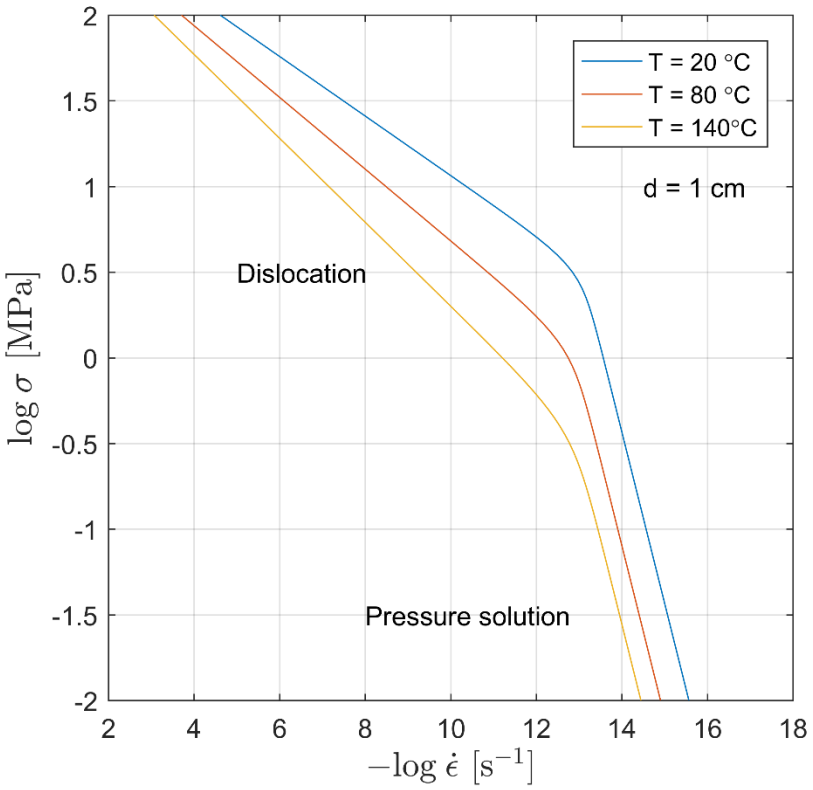

FIGURE 3.2

Transition between dislocation creep (Wawersik and Zeuch 1986), and pressure solution creep (Spiers et al. 1990) for different temperatures and a fixed grain size of *d* = 1cm.

In order to formulate a rheological model combining two creep mechanisms in a smooth manner, it is necessary to recast the constitutive equation in a form defining stress as a function of strain rate as follows:

$$\sigma = 2\eta^{*}\dot{\varepsilon} \tag{3.8}$$

Here, η^{*} is the effective viscosity that depends on the strain rate and temperature. Constitutive laws in the above form are typically required to formulate the finite element or the finite difference model of the deformation process. For the case of simultaneously active pressure solution and dislocation creep mechanisms, it is not possible to derive an analytical expression for effective viscosity as a function of strain rate. In order to avoid the numerical solution of the constitutive equation, it is quite

common to adopt a so-called Carreau model (Cornet et al. 2018a). This model provides a simple expression for the effective viscosity that yields a very close approximation to the exact combination of both mechanisms:

$$\eta^* = \eta_{ps}\left(1 + \frac{\dot{\varepsilon}}{\dot{\varepsilon}^*}\right)^{\frac{1/n-1}{2}} \tag{3.9}$$

Here

$$\eta_{ps} = \left(2A_{ps}\right)^{-1} \tag{3.10}$$

is the effective viscosity of the pressure solution creep, which is linear Newtonian, and the transition strain rate:

$$\dot{\varepsilon}^* = A_{ps}\left(\frac{A_{ps}}{A_{dc}}\right)^{\frac{1}{n-1}} \tag{3.11}$$

is solved from the condition that strain rates of pressure solution and dislocation creep mechanisms are the same, namely:

$$\dot{\varepsilon}^* = \dot{\varepsilon}_{ps} = \dot{\varepsilon}_{dc} \tag{3.12}$$

Figure 3.3 shows the resulting smooth transition between both creep mechanisms for different temperatures.

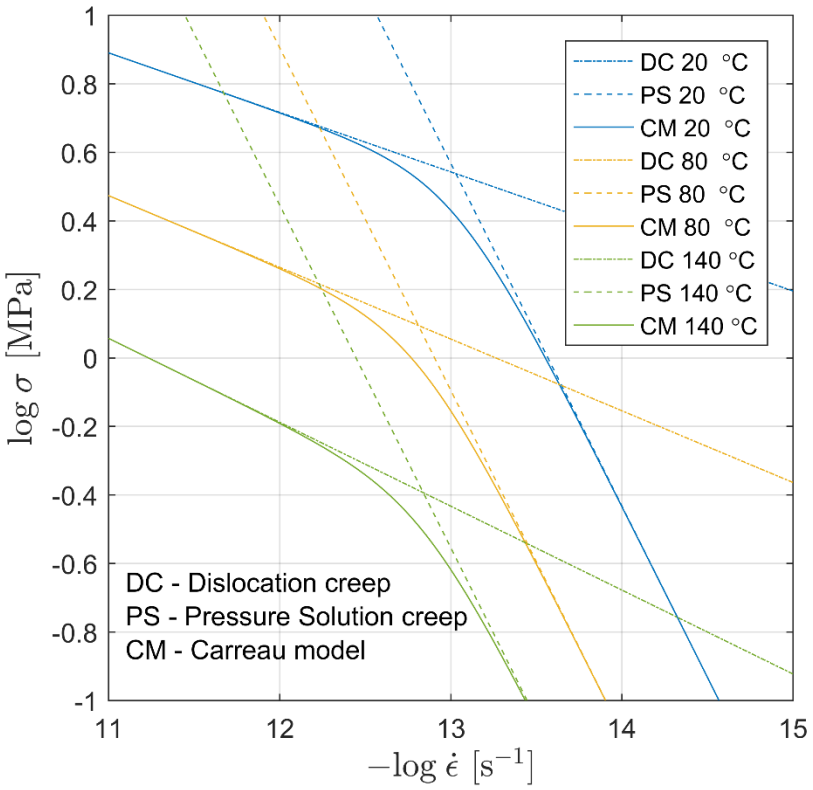

FIGURE 3.3

Smooth transition between dislocation creep, and pressure solution creep implemented by Carreau viscosity model (Cornet et al. 2018a).

3.2 Grain size and recrystallization

The strain rate of the pressure solution creep linearly depends on the differential stresses, as shown in the above equations. However, the dependence on the grain size is more complicated as the strain rate is inversely proportional to the cube of the mean grain size. Practically, it means that at given stress level, doubling the grain size results in almost an order of magnitude reduction of the strain rate. If we put it the other way around, larger grain size would require more substantial stresses to maintain the same creep rate. Hence, pressure solution creep becomes stronger (“hardens”) with increasing grain size. This effect is rather dramatic, as visualized in Figure 3.4.

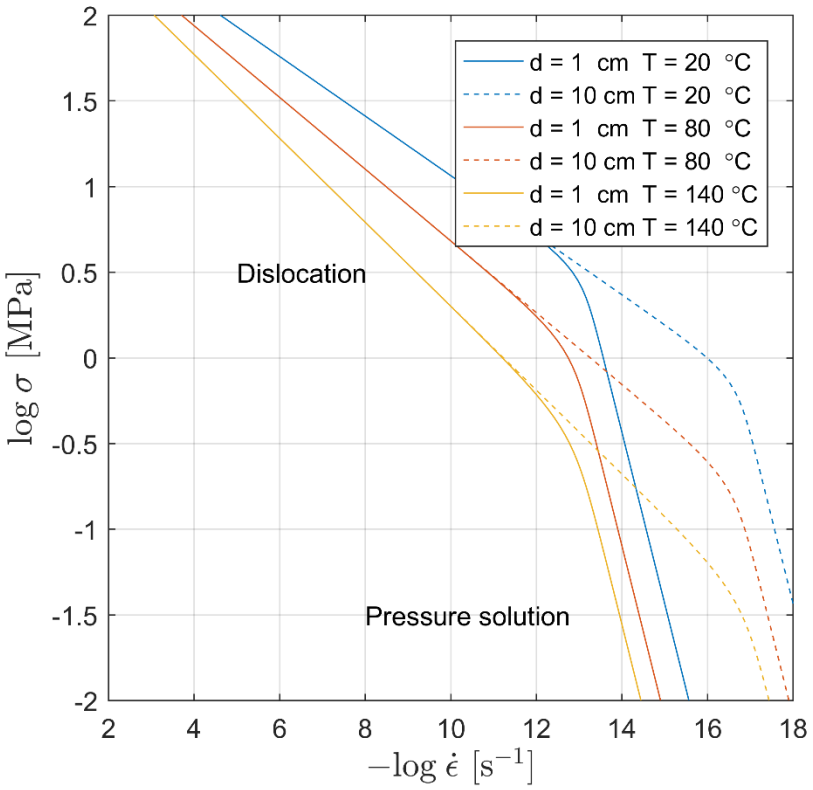

FIGURE 3.4

Influence of mean grain size on the transition between dislocation creep, and pressure solution creep.

Increasing grain size from 1 cm to 10 cm shifts the transition to significantly lower stresses and lower strain rates, essentially “switching off” pressure solution creep. Hence mean grain size has a decisive influence on the transition between the creep mechanisms.

In natural wet salts (>10-20 ppm of water) mean grain size is expected to decrease due to rapid dynamic recrystallization by fluid assisted grain boundary migration (Urai and Spiers 2007). The grain size reduction should, in theory, cause weakening and activation of the pressure solution creep mechanism. However, this process is counteracted by grain growth. The details of the grain size reduction – grain growth balance remains poorly understood. See (De Bresser, Ter Heege, and Spiers 2001) for an overview of the existing approaches to parametrize the mean recrystallized grain size. Among other

studies, (Ter Heege et al. 2005a) have obtained a systematic parametrization of the grain size evolution due to dynamic recrystallization as a function of flow stress and temperature for the wet salt samples:

$$\left(\frac{d}{b}\right) = K\left(\frac{\sigma}{\mu}\right)^{-p} \exp\left(\frac{\Delta Q}{aRT}\right) \tag{3.13}$$

Here $K = 10^{-1.55}$, $p = 1.85$ and $a = 1$ are non-dimensional constants, $b = 3.99 \cdot 10^{-10}$ m is the Burgers vector length, $\mu = 1.5 \cdot 10^{10}$ Pa the shear modulus, and $\Delta Q = 14.2 \cdot 10^{3}$ J·mol^{-1} the difference between activation energy for lattice diffusion and the activation energy for grain boundary diffusion.

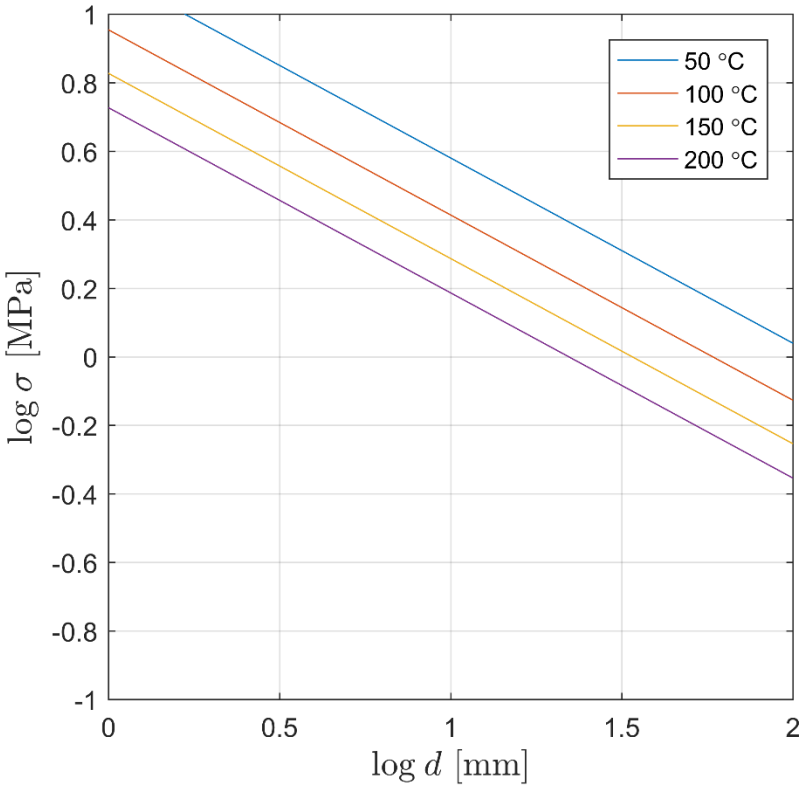

FIGURE 3.5

Mean grain size dependence on differential stress and temperature due to dynamic recrystallization for wet rocksalt (Ter Heege et al., 2005a).

Figure 3.5 visualizes the parametrization proposed by (Ter Heege et al. 2005a). The recrystallized grain size is inversely proportional to the temperature and to the differential stress, which means that an increase of either stress or temperature leads to a decrease of the equilibrium grain sizes.

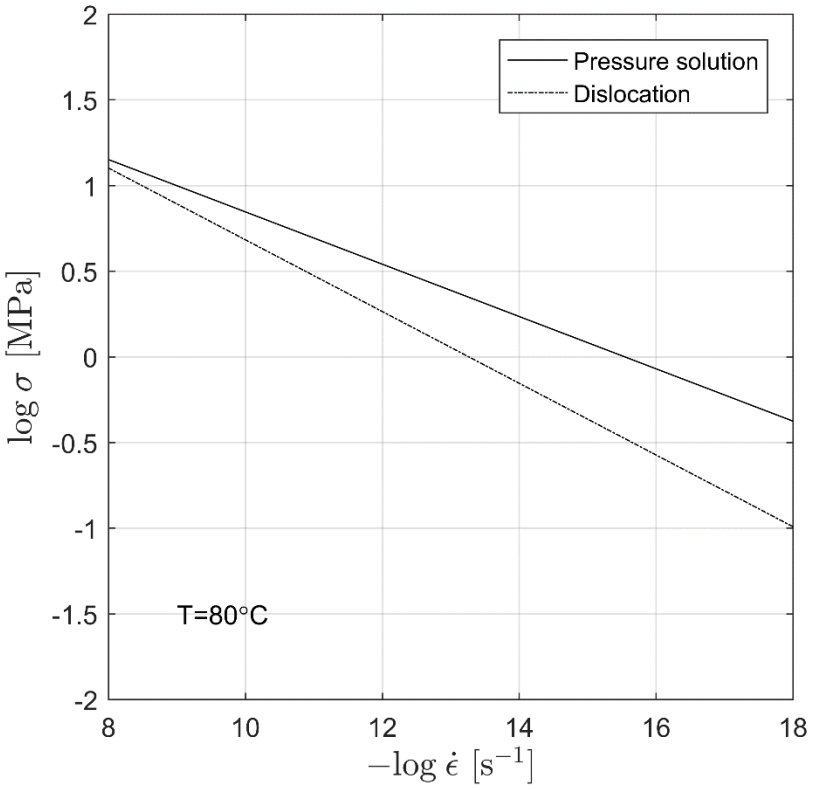

FIGURE 3.6

Comparison of pressure solution creep (Spiers et al. 1990) combined with instantaneous dynamic recrystallization (Ter Heege et al., 2005a), vs. dislocation creep (Wawersik and Zeuch 1986) at 80 °C.

If we substitute the recrystallized grain size expression of (Ter Heege et al. 2005a) (Equation 3.13) in the pressure solution creep law of (Spiers et al. 1990) (Equation 3.2), we obtain an effective power-law creep mechanism as shown in Figure 3.6. This combination is adequate if recrystallization can be assumed to occur instantaneously on geological time scale. Laboratory experiments, in general, confirm the validity of

this assumption (Urai and Spiers 2007). The power-law exponent of the recrystallized pressure solution creep is larger than that of the dislocation creep, which is indicated by a shallower slope in Figure 3.6. Moreover, the recrystallized pressure solution creep is uniformly stronger compared to dislocation creep over the entire range of relevant strain rates and differential stresses. That implies that salt will deform predominantly by the dislocation creep, and pressure solution creep will thus never be active. From these observations, we can immediately conclude that the recrystallized grain size, as described by (Ter Heege et al. 2005a) (Equation 3.13), probably cannot be extrapolated to the low-stress regime, since it predicts an essentially unbounded grain growth that goes far beyond the natural limits.

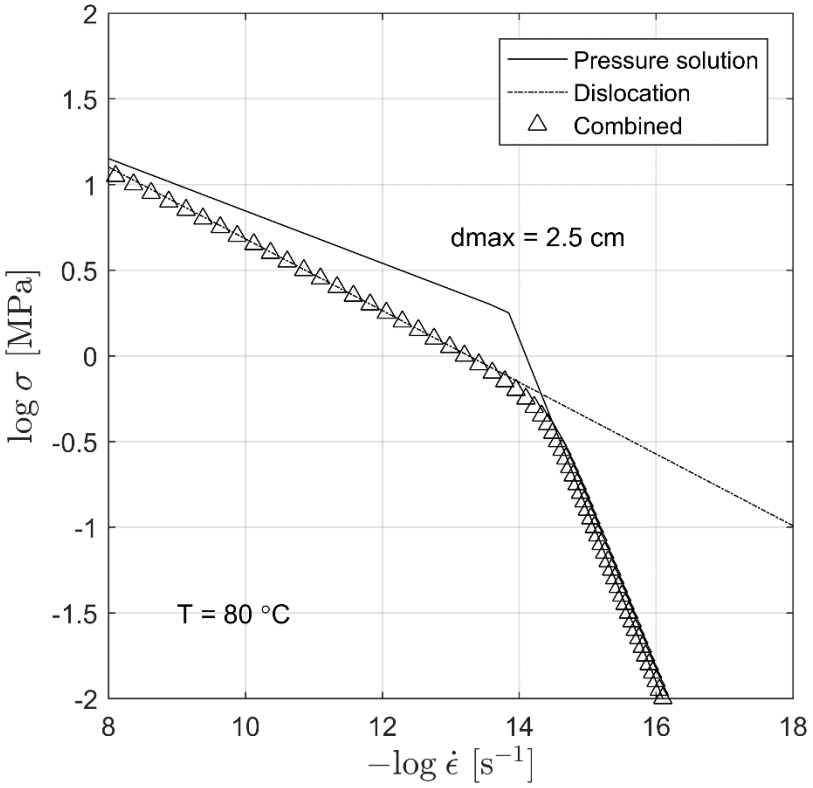

FIGURE 3.7

Comparison of pressure solution creep (Spiers et al. 1990) combined with instantaneous dynamic recrystallization (Ter Heege et al., 2005a), vs. dislocation creep (Wawersik and Zeuch 1986) at 80 °C.

Enforcing an upper bound for the grain size causes the changes shown in Figure 3.7. When recrystallized grain size reaches the upper limit, the recrystallized pressure solution creep rapidly turns ("kinks") into a normal pressure solution creep with a constant grain size equal to the enforced limit. A combination of pressure solution creep and dislocation creep becomes essentially insensitive to the recrystallization process. The only relevant parameter that remains, in that case, is the upper bound of the mean grain size d_{max}.

3.3 From microscale to macroscale

Present knowledge about pressure solution creep has mainly emerged from the extensive microstructural studies (Urai et al. 1986), (Spiers et al. 1990), and laboratory experiments. However, currently, our knowledge is not conclusive enough to build a reliable and unique macroscopic rheological description of the pressure solution creep. A major part of the problem remains in predicting the evolution of the grain size as a function of all possible macroscopic variables, such as differential stress, temperature, composition, water concentration, and possibly accumulated strain.

Moreover, a related issue is that it has been proposed that under very small differential stresses, the fluid films at grain boundaries disintegrate into arrays of fluid-inclusions with lower grain boundary diffusivity and essentially 'switches-off' the pressure solution creep mechanism (Urai et al. 2008). So far, no creep law has been proposed that includes this transition in a quantitative manner.

As these fundamental tasks go far beyond the scope of this report, we leave it as a topic for future research projects. In this study, we instead adopt a different strategy. Since the upper bound of the mean grain size remains poorly constrained, we treat it as a free parameter and conduct a parametric study by varying it in a wide range and monitoring the influence on the predicted stress fields within the salt bodies. Figure 3.8 demonstrates a typical combination of pressure solution creep and dislocation creep mechanisms along with grain size ranges considered here.

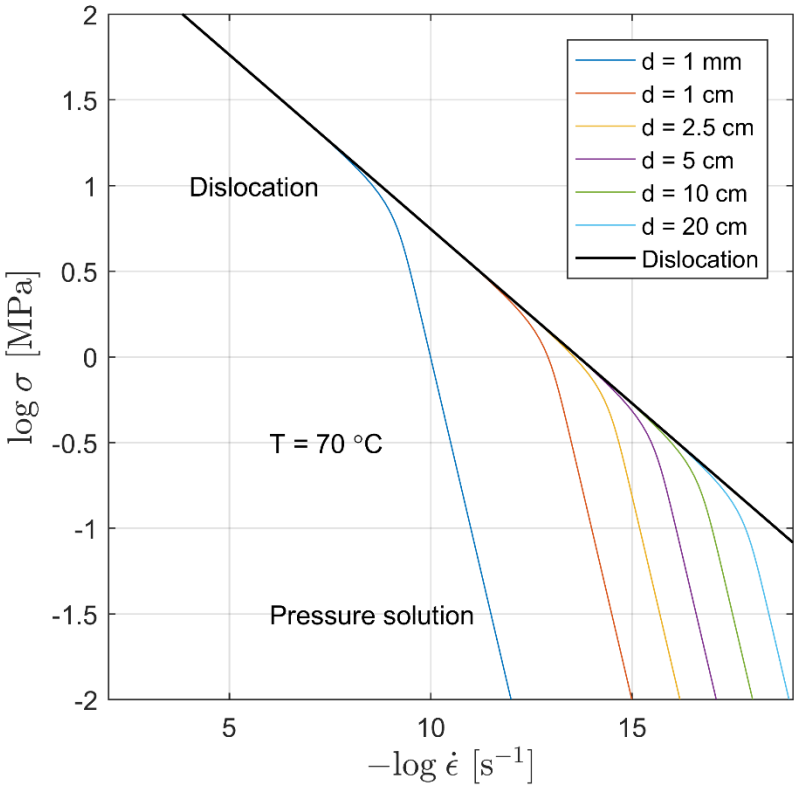

FIGURE 3.8

A combination of dislocation creep (Wawersik and Zeuch 1986), and pressure solution creep (Spiers et al. 1990) for grain size ranging between d = 1 mm and d = 20 cm at 70 °C.

3.4 Summary

Our preceding considerations outlined above enable us to draw the following intermediate conclusions regarding the salt rheology in the context of this report:

[1] Mean grain size has a decisive influence on the transition between the dislocation and pressure solution creep mechanisms. The significance of this effect so far received little attention in the literature. In this report, we put an explicit accent on this issue.

[2] Dynamic recrystallization, as described by (Ter Heege et al. 2005a), mathematically predicts the total inactivity of pressure solution creep over the entire range of stresses and strain rates physically achievable in the natural conditions. This is attributed to essentially unbounded grain size growth at low stresses (which may grow to unrealistically large values). Introducing an upper bound for the grain size in the parametric model essentially removes the influence of recrystallization on the pressure solution creep. The upper bound for the mean grain size becomes the only important parameter controlling the transition from the dislocation creep to the pressure solution creep.

[3] Due to a significant amount of experimental evidence of the occurrence of pressure solution creep in natural salts (Urai et al., 2008), we have to conclude that dynamic recrystallization, according to Ter Heege et al. (2005) probably cannot be extrapolated to the low-stress regime. Moreover, the disintegration of continuous fluid films at grain boundaries is well-known to occur from microstructural observations of rock salt (see phase 1 of this project). This effect needs to be quantified to be taken into account in numerical models of salt domes.

[4] The upper bound for the mean grain size remains an essentially undetermined key parameter that requires additional constraints from experiments and observations in each particular case study. In this report, we treat it as a free parameter and conduct a parametric study by varying it over a wide range.

4 Modeling

To better understand the stress distributions to be expected in salt structures, we perform three-dimensional numerical simulations to model the stress evolution of the salt structure. With this, we not only track the stress evolution but also check the stability of the salt structure.

We consider three generic models of typical salt structure geometries, as found in the Netherlands, which includes a salt pillow, a salt wall model, and a model with a flat salt bed (Figure 4.1). For all models, we simulate the stress evolution of the salt structure, starting 300 kyrs ago until the present day. Doing that, we consider the effect of glacial loading and unloading during the Saalian ice age and tectonic boundary conditions within the expected ranges and systematically compare the resulting state of stress at present day with predictions of other models with different input parameters.

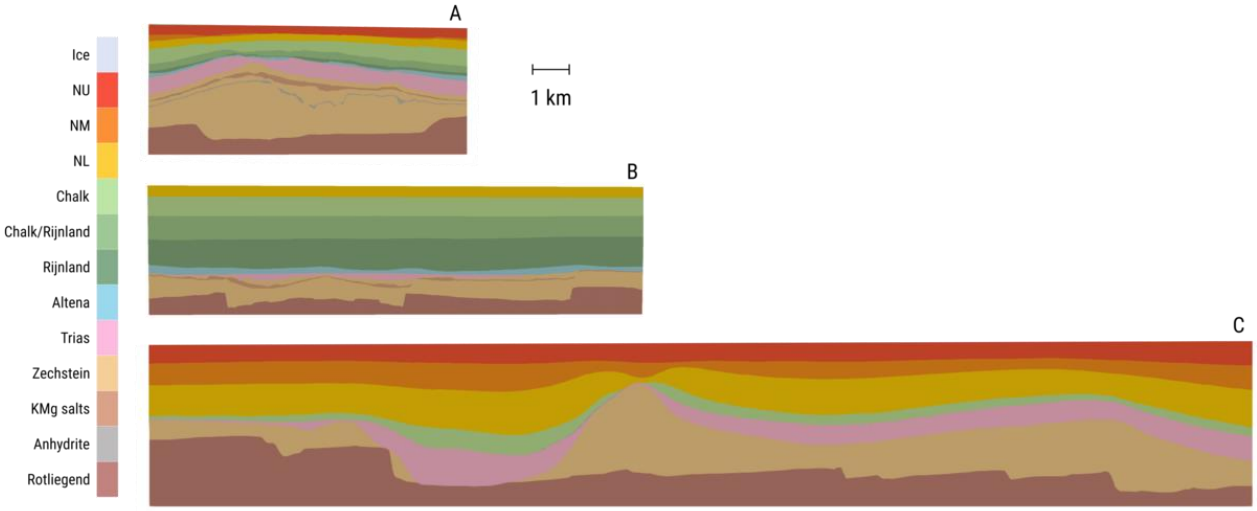

FIGURE 4.1

Stratigraphic overview of the three model types examined in this study. **A:** A salt pillow structure with internal heterogeneities, i.e., K-Mg salt and anhydrite layers. **B:** A flat-bedded salt structure with a weak K-Mg layer intrusion. **C:** A salt wall or dome structure. The wall structure is the largest among the three model types, but it does not contain internal heterogeneities. Colors and layer names are adapted from (Duin et al. 2006).

The objective of these models was to identify significant key parameters and further analyze their impact on the stress state within the rock salt. In this sense, we focus on varying the rheology of the salt, internal heterogeneities, and model-specific tectonic boundary conditions.

Other model properties, such as the density and rheology of the overburden, temperature boundary conditions, and thermal rock properties, are kept unmodified. Of course, also all of those properties contribute to the overall stress state in a coupled, thermomechanical model. We, therefore, adopt those parameters to observed ranges of actual data, whenever this is possible, or incorporate values from the literature. A case study for a specific site, where we would be able to take into account actual observations, will have a higher predictive power but was not the objective of this report.

In the following, we will present details of the numerical approach, the employed model geometries, the boundary and initial conditions applied to the models as well as an overview of the assigned rock properties and other material parameters. The systematic modeling is conducted by computing a reference case and vary selected (uncertain) model parameters.

4.1 Numerical approach

The three-dimensional numerical modeling presented in this report is performed using the open-source parallel finite-difference software package LaMEM (Kaus et al. 2016). Below, we briefly summarize the details of the mathematical model and numerical implementation.

4.1.1 Mathematical description

The model is based on a coupled system of momentum and mass conversation equations, respectively, with velocity (v_i) and pressure (P) as primary unknowns:

$$\frac{\partial \tau_{ij}}{\partial x_j} - \frac{\partial P}{\partial x_i} + \rho g_i = 0 \tag{4.1}$$

$$\frac{1}{K}\frac{D(P - \alpha P_f)}{Dt} + \frac{\partial v_i}{\partial x_i} = 0 \tag{4.2}$$

Here x_i $(i = 1,2,3)$ denote Cartesian coordinates, $\tau_{ij} = \sigma_{ij} + P\delta_{ij}$ is the Cauchy stress deviator, ρ density, g_i the gravity acceleration vector, α the Biot constant, P_f the pore fluid pressure, K the elastic bulk modulus, and $\frac{D}{Dt}$ stands for the material time derivative, respectively. The visco-elastoplastic constitutive equation for the deviatoric stress is given by:

$$\dot{\varepsilon}_{ij} = \dot{\varepsilon}_{ij}^{el} + \dot{\varepsilon}_{ij}^{vs} + \dot{\varepsilon}_{ij}^{pl} = \frac{\check{\tau}_{ij}}{2G} + \dot{\varepsilon}_{II}^{vs}\frac{\tau_{ij}}{2\eta} + \dot{\varepsilon}_{II}^{pl}\frac{\tau_{ij}}{\tau_{II}}, \tag{1.3}$$

where $\dot{\varepsilon}_{ij} = \frac{1}{2}\left(\frac{\partial v_i}{\partial x_j} + \frac{\partial v_j}{\partial x_i}\right) - \frac{1}{3}\frac{\partial v_k}{\partial x_k}\delta_{ij}$ is the deviatoric strain rate tensor, $\dot{\varepsilon}_{ij}^{el}, \dot{\varepsilon}_{ij}^{vs}, \dot{\varepsilon}_{ij}^{pl}$ are the elastic, viscous and plastic components, respectively, $\check{\tau}_{ij} = \frac{\partial \tau_{ij}}{\partial t} + \tau_{ik}w_{kj} - w_{ik}\tau_{kj}$ is the Jaumann objective stress rate, $w_{ij} = \frac{1}{2}\left(\frac{\partial v_i}{\partial x_j} - \frac{\partial v_j}{\partial x_i}\right)$ is the spin tensor, G is the elastic shear modulus, η denotes the effective viscosity of the creep mechanism and the subscript $_{II}$ denotes the square root of the second invariant of a corresponding tensor, e.g., for the deviatoric stress $\tau_{II} = \left(\frac{1}{2}\tau_{ij}\tau_{ij}\right)^{1/2}$. The magnitude of the plastic strain rate ($\dot{\varepsilon}_{ij}^{pl}$) is determined by enforcing the Drucker-Prager yield criterion:

$$\tau_{II} \leq \tau_Y = (P - P_f)\cdot \sin(\phi) + c \cdot \cos(\phi), \tag{4.4}$$

where τ_Y is the yield stress, ϕ is the friction angle, and c is the cohesion. For this study, we describe the pore fluid pressure P_f as a function of the limiting hydrostatic (P_h) and lithostatic (P_{lith}) pressure and define the pore fluid pressure ratio λ :

$$P_f = P_h + \lambda(P_{lith} - P_h) \tag{4.5}$$

λ is generally assumed to be 0.2 in the simulations presented here.

4.1.2 Numerical implementation

We discretize the conservation Eqs. (4.1) and (4.2) in space using staggered grid finite differences (Harlow and Welch 1965) as it is a low-order but stable discretization for (nearly) incompressible fluid flow To achieve parallel scalability we use the distributed arrays (DMDA) and iterative solvers (KSP, SNES) from the PETSc library (Balay et al. 2019). The free surface is implemented using a so-called sticky air approach, which assigns a relatively low but nonzero viscosity to the air phase, together with an appropriate stabilization method to allow for sufficiently large time steps (Duretz et al. 2011; Kaus, Mühlhaus, and May 2010). The topography of the free surface is explicitly tracked by an internal 2D grid that covers the entire domain.

We employ a marker and cell (Harlow and Welch 1965) method to track material properties and implement material advection in an Eulerian kinematical framework.

During the advection, the elastic history stresses from the previous time step (τ_{ij}^{n}) are corrected on markers to account for the rigid-body rotation, and then interpolated on the edge and cell control volumes using distance-based averaging (Duretz et al. 2011) to obtain the effective strain rates:

$$\dot{\varepsilon}_{ij}^{*} = \dot{\varepsilon}_{ij} + \frac{\tau_{ij}^{*}}{2G\Delta t}, \qquad \tau_{ij}^{*} = \tau_{ij}^{n} + \Delta t\left(w_{ik}\tau_{kj}^{n} - \tau_{ik}^{n}w_{kj}\right). \tag{4.6}$$

The second invariant of the effective strain rate is computed by cross-interpolation and averaging of the missing data (squares of the corresponding components) between all the control volumes. The effective viscosity (η^{*}) and the updated deviatoric stresses (τ_{ij}) are computed from the effective strain rates, using the standard quasi-viscous expression:

$$\tau_{ij} = 2\eta^{*}\dot{\varepsilon}_{ij}^{*}, \qquad \eta^{*} = \min\left[\left(\frac{1}{G\Delta t} + \frac{1}{\eta}\right)^{-1}, \frac{\tau_{Y}}{2\dot{\varepsilon}_{II}^{*}}\right]. \tag{4.7}$$

The discretized coupled system of nonlinear algebraic equations is solved at each time step using the preconditioned Jacobian-Free Newton-Krylov (JFNK) method with line-

search as implemented in the PETSc SNES nonlinear solver framework (Balay et al. 2019).

4.2 Boundary Conditions

4.2.1 Tectonic boundary conditions

For the systematic modeling study, we establish tectonic stress by applying a constant, horizontal strain rate to our models. In the scope of this work, we employ strain rates of the order of $\pm(10^{-17}$ to 10^{-16} $s^{-1})$ to either extend or compress the model perpendicular to the orthogonal domain boundaries. Even though there are no direct measurements on tectonic strain rate values in the N. Netherlands, these values are in the range of those estimated for Northern Europe, which predominantly result from glacial isostatic unloading (Nocquet, Calais, and Parsons 2005).

The overburden density determines the amount of vertical loading and the resulting vertical stress on the salt body. In Figure 4.2, we show observations of vertical stress obtained from wellbore observations in Veendam (Raith and Urai 2018). Here, we adopt the rock densities used in (Raith and Urai 2018) and test the salt pillow model prediction of vertical stress against these observations. As other data is not available, we assume that the density of the individual overburden layers is not different from similar layers of the same rock type in the other model geometries.

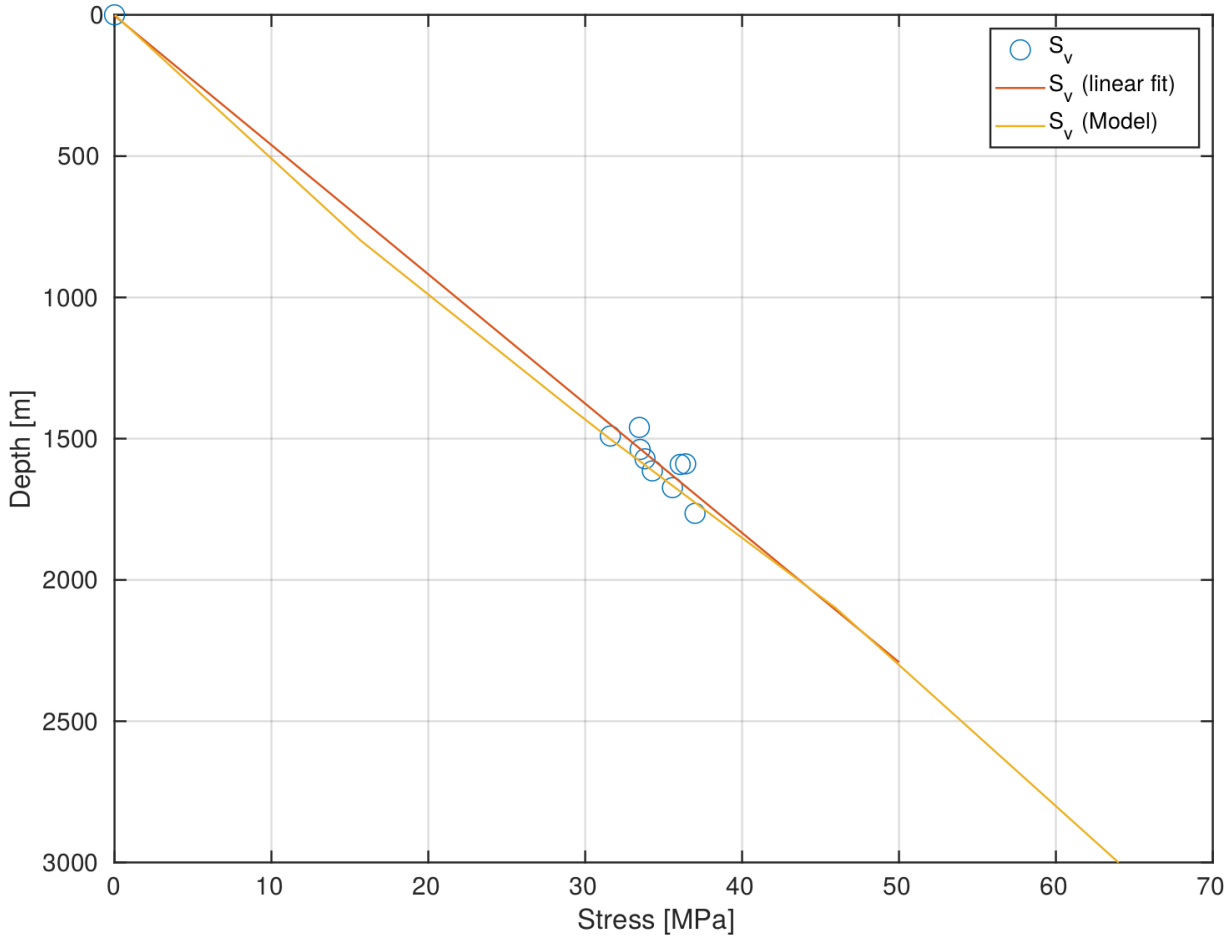

FIGURE 4.2

Vertical stress and model density calibration. Blue symbols denote vertical stress obtained from wellbore observations, as reported in (Raith and Urai 2018). The solid red line shows a linear fit through these data points. For this study, we adopt the rock densities used in (Raith and Urai 2018) and compute the model prediction of the vertical stress (solid yellow line).

4.2.2 Glacial tectonic boundary conditions

In addition to the weight of the overburden, we also account for the weight of the ice sheet that overlaid the Netherlands during the Saalian ice age (Ehlers 1990; Lang, Lauer, and Winsemann 2018; Svendsen et al. 2004). The glaciation period took place approximately between 300-130 kyrs ago (Lauer and Weiss 2018; Svendsen et al. 2004) with a maximum extent of the ice sheet at 300 kyrs (Lang et al. 2018; Svendsen et al.

2004). For the ice sheet, we assume a maximum thickness of 300 m (Lang et al. 2014), but unlike (Lang et al. 2014), we do not account for a lateral retreat of the ice sheet as our maximum model width is less than 25 km. Instead, we assume a gradually decreasing thickness of the ice sheet between 160 kyrs and 130 kyrs.

4.2.3 Temperature boundary and initial conditions

The rheology of rock salt is usually assumed to be temperature-dependent. Thus, a realistic and accurate prediction of the temperature distribution within the model is essential for a well-constrained state of stress. The conductivity of rocksalt is well constrained, e.g., (Bräuer et al. 2011b; Jackson and Hudec 2017) and much higher ($k_{rocksalt} \approx 5.5 \frac{W}{m \cdot K}$) than the thermal conductivities of sedimentary rocks ($k_{sedimentary\ rocks} \approx 2.5 \frac{W}{m \cdot K}$). In order to mimic a realistic temperature distribution within the model domains, we compute a steady-state distribution for the given thermal conductivities of the rocks. For doing that, we require realistic temperature estimates to superimpose the model temperature at the location of the model domain boundaries. As a first-order estimate, we extract average temperatures from present-day temperature observations at respective depths of the model domains (Figure 4.1).

The temperature data showed here (Bonté, Van Wees, and Verweij 2012) are observations from the entire onshore area of the Netherlands from which we computed a 2nd order regression line (solid red line) as a proxy for an average geotherm in the Netherlands. For us, this approximation estimates the basal boundary temperatures of the respective model types in this study:

- 113 °C (flat-bedded salt model)
- 130°C (salt pillow model)
- 150°C (salt wall model)

As surface boundary temperatures, we employ 0°C for all model types.

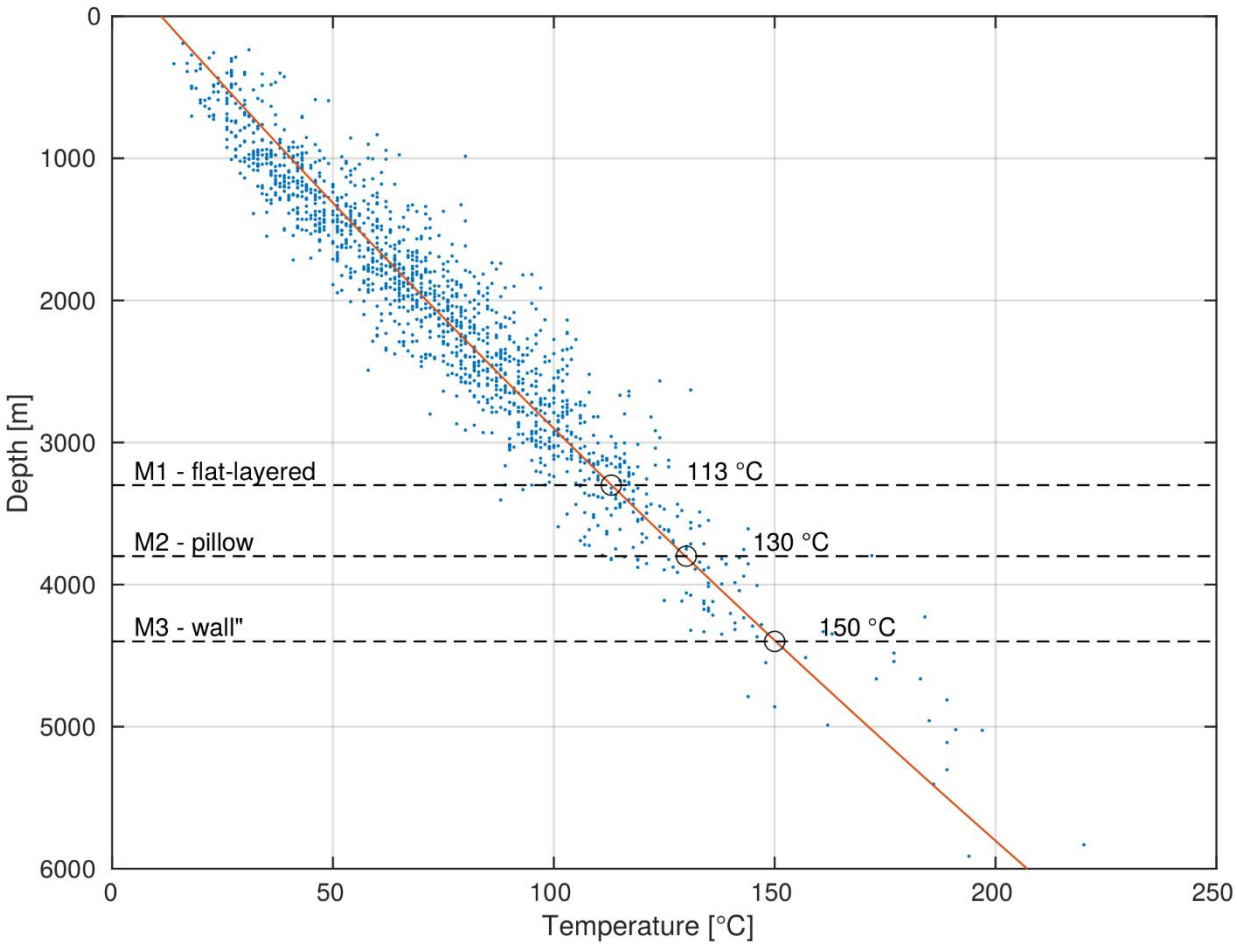

FIGURE 4.3

Temperature constraints for generic model types. Blue markers indicate temperature observations across the Netherlands (Bonté et al. 2012). The averaged geotherm is given as second-order polygon (red, solid line). Dashed horizontal lines mark the depths of the generic model types in this report. We use the associated temperature of the depths as bottom-boundary temperatures for the respective reference models.

4.3 Model geometries, resolution and rock parameters

For the systematic modeling study, we employ three generic model geometries, a salt pillow (Figure 4.4), a salt wall (Figure 4.5), and a flat-bedded salt structure (Figure 4.6). The stratigraphy and layer names of these models are inspired by (Duin et al. 2006), and the domain sizes are given in the respective figures. For the salt pillow, we set a

resolution of 30 × 30 × 25 m, with the salt wall model, we yield a resolution of 40 × 40 × 40 m; and for the flat-bedded salt structure, we obtain a resolution of 40 × 40 × 30 m.

All rock types are modeled as poro-visco-elastoplastic materials with the parameters listed in Table 4.1. For the elastic properties, we use the parameters from (Raith and Urai 2018), and the thermal properties are adapted from (Bräuer et al. 2011b). For the rock salt, in particular, we employ the viscous creep laws explained in section 3 and use the parameters listed in Table 3.1. In the case of K-Mg salt, which should be weaker than the primary rock salt (Jackson and Hudec 2017; Raith and Urai 2018), we decrease the effective prefactor of the effective viscosity by one order of magnitude.

TABLE 4.1

General rheological parameters used for the modeling in this report.

Lithology	ρ [kg m^{-3}]	ν [1]	E [GPa]	C [MPa]	ϕ [°]	**Viscous Rheology**	α [K^{-1}]	c_p [kJ kg^{-1}K^{-1}]	k [W m^{-1} K^{-1}]	λ [1]
Rotliegend	2600	0.18	15	10	30	10^{23} Pa s	3 10^{-5}	1.2	2.5	0.3
Rock salt	2040	0.25	30	10	30	Table 3.1	3 10^{-5}	1.2	5.5	0.1
K-Mg salt	2040	0.25	30	10	30	Table 3.1	3 10^{-5}	1.2	5.5	0.1
Anhydrite	2600	0.25	30	10	30	Table 3.1	3 10^{-5}	1.2	5.5	0.1
Triassic	2450	0.30	10	10	27	10^{23} Pa s	3 10^{-5}	1.2	2.5	0.2
Jurassic	2400	0.25	15	10	27	10^{23} Pa s	3 10^{-5}	1.2	2.5	0.2
L. Cretaceous	2350	0.23	15	10	27	10^{23} Pa s	3 10^{-5}	1.2	2.5	0.2
M. Cretaceous	2350	0.20	12	10	27	10^{23} Pa s	3 10^{-5}	1.2	2.5	0.2
U. Cretaceous	2300	0.18	10	10	27	10^{23} Pa s	3 10^{-5}	1.2	2.5	0.2
Tertiary	2100	0.30	5	10	27	10^{23} Pa s	3 10^{-5}	1.2	2.5	0.2
Paleogene	2000	0.38	5	10	27	10^{23} Pa s	3 10^{-5}	1.2	2.5	0.2
Neogene	1900	0.38	5	10	27	10^{23} Pa s	3 10^{-5}	1.2	2.5	0.2

Legend

ρ	*Density*
ν	*Poisson ratio*
E	*Young's modulus*
C	*Cohesion*
ϕ	*Friction angle*
α	*Thermal expansion*
c_p	*Specific heat capacity*
k	*Thermal conductivity*
λ	*Pore pressure ratio*

For simplicity, we do not account for the temperature dependence of the host rock viscosity, but given the chosen values, the effective relaxation time is such that the material behaves poro-elastoplastic.

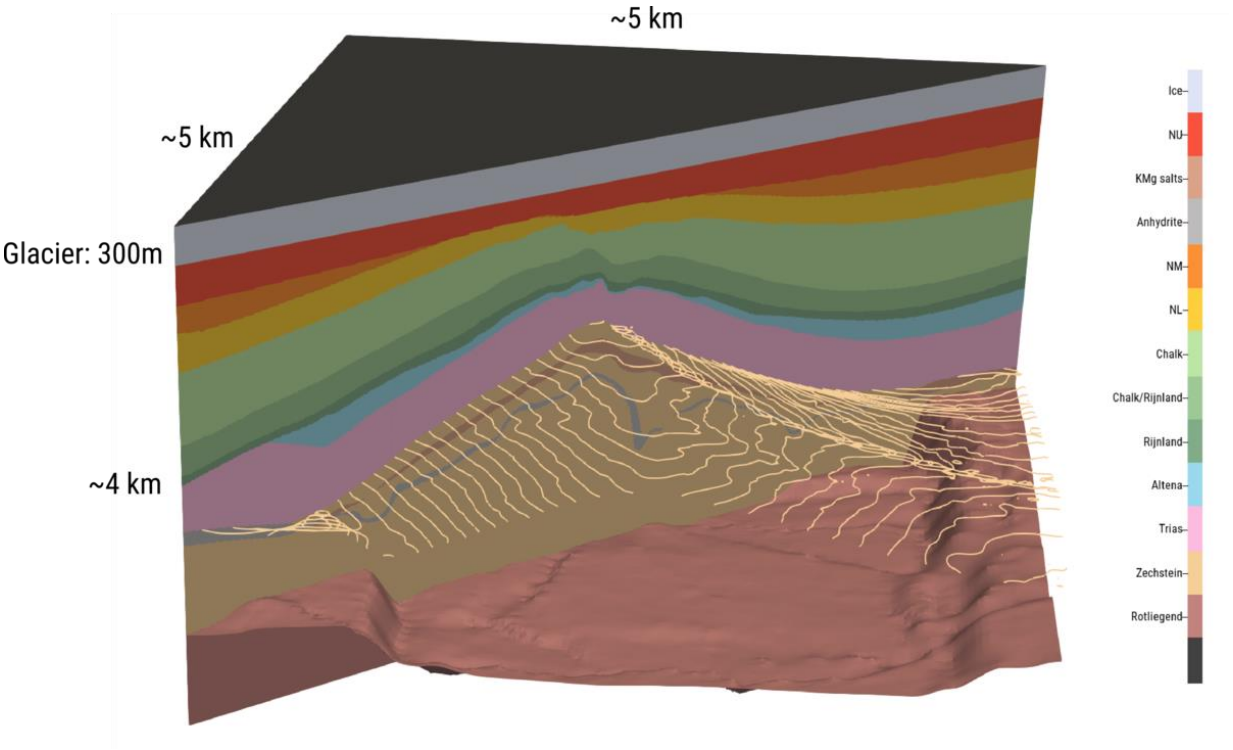

FIGURE 4.4

Stratigraphy and geometry of the salt pillow model. Colors and layer names are adapted from (Duin et al. 2006). Contour lines show the location of the Top salt. In general, the Zechstein salt is heterogeneous; here, we included two heterogeneities, a layer of Anhydrite and a layer of K-Mg salts. Note that for some simulations, we remove these heterogeneities to study their impact on the stress state.

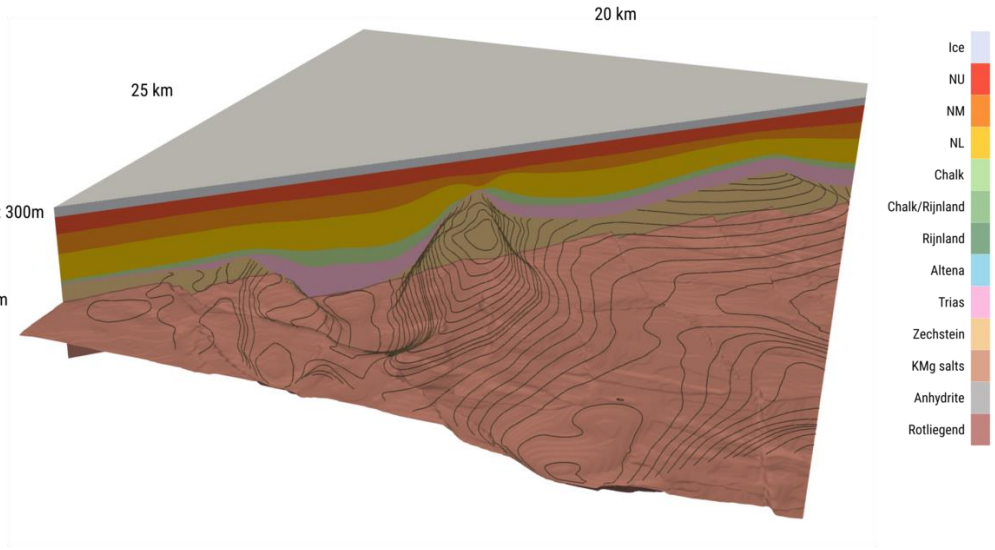

FIGURE 4.5

Stratigraphy and geometry of the salt wall model. Colors and layer names are adapted from (Duin et al. 2006). Contour lines show the location of the Top salt. In contrast to the other models, the salt wall model geometry does not contain heterogeneities.

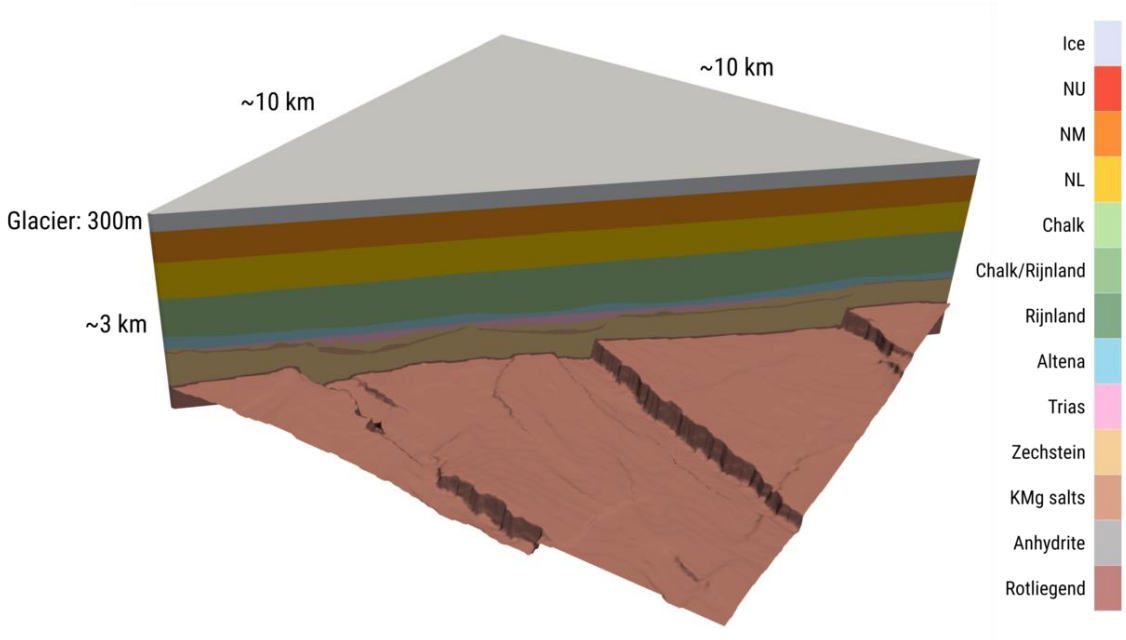

FIGURE 4.6

Stratigraphy and geometry of the model with flat bedded salt. Colors and layer names are adapted from (Duin et al. 2006). The brownish surface shows the top basement, which has pre-existing faults. By default, the Zechstein contains a layer with K-Mg salt, which is either kept or removed to study its impact on the model stress state.

4.4 Salt Pillow

We present the modeling results in terms of maximum differential stress and strain rates. In the models, the strain rate is treated as a strain rate tensor (see section 4.1.1), however, to illustrate the tensor as a scalar value, we compute the second invariant of the strain rate tensor, which, for simplicity, we denote as strain rate.

4.4.1 Reference model with coupled PS-DC creep

For reference, we show a model that incorporates a coupled pressure solution and dislocation (PS-DC) creep rheology with a maximum grain size of 2.5 cm and in the absence of external tectonic strain (Figure 4.7). We look at a vertical cross-section through the salt pillow. The gray surface shows the top basement, and temperature contour lines outline the temperature structure within the model domain (see section 4.2.3). In the background, shaded colors indicate the stratigraphy and salt-internal heterogeneities (see also Figure 4.4).

The thermal conductivity of the overburden is set to $2.5\,\frac{W}{m\cdot K}$, whereas the conductivity of salt is typically much higher (Jackson and Hudec 2017). Here, we prescribe the salt conductivity with $5.5\,\frac{W}{m\cdot K}$ (Bräuer et al. 2011b). As the temperature evolution in our model is assumed to be in steady-state, the contour lines indicate a consistent distribution. Contour lines are bent upwards above the salt top in the overburden. Below, within the salt, they are bent downwards. At the base of the pillow, they are bend upwards, consistent with the higher conductivity of the salt.

The model results are shown for the present-day, which corresponds to a snapshot of the simulation after 300 kyrs.

To illustrate areas of active deformation, we visualize self-consistent strain rates in Figure 4.7a., where the color scale is clipped at 10^{-15} s^{-1}. Strain rates below 10^{-16} s^{-1} are made increasingly transparent. High strain rates are strongly correlated with the heterogeneities present in the salt structure. The effect is multifaceted. Dense anhydrite induces high strain rates in the surrounding salt. In this model, the weak

K-Mg layer decouples the salt at the very top of the pillow from the salt below, which allows for a differential motion and increased strain rates in the vicinity of the K-Mg salt layer. Moreover, we also observe high strain rates at the flanks of the pillow and the base of the salt structure. Faults in the basement topography result in a focussing effect of the strain rates within the salt. We want to emphasize that these faults are not a result of active faulting during the simulation, but part of the superimposed model geometry. The increased strain rates are thus caused by the focused flow of the salt in areas with variations in salt thickness.

In Figure 4.7b, we illustrate the maximum differential stress on the same cross-section, as in Figure 4.7a. As the stresses in the overburden are much higher than in the salt, we limit the color scale to stress magnitudes below 200 kPa and indicate higher stresses with transparent red shading.

The anhydrite stringers are associated with the highest differential stresses and reflect the different (power-law) rheology used for anhydrite (see A typical combination of the dislocation creep (Wawersik and Zeuch 1986), and pressure solution creep (Spiers et al. 1990) with reasonable grain size (e.g., d = 1cm) results in a smooth transition shown in Figure 3.2. As expected, dislocation creep is active in the high-stress regime, while pressure solution creep is dominant in the low-stress regime. The influence of temperature is moderate. Note that for the dislocation creep described by (Wawersik and Zeuch 1986), the effective stress exponent is temperature-dependent. Hence on a log-log plot, slopes of the dislocation creep branch are slightly different. For other creep mechanisms, e.g. (Ter Heege et al. 2005b), this effect is not present.

Table 3.1). In general, the stress patterns are very similar to the patterns of strain rate. We observe the highest stresses within the salt in the vicinity of the stringers.

To better interpret these stress results, we employ Figure 4.8 additionally, which is adapted from Figure 3.8. Here, we, in particular, indicate the value ranges obtained in this model. The contour lines show the coupled pressure-solution- and dislocation-

creep behavior of rock salt at a 70°C reference temperature, which corresponds to the top of the salt pillow. Without external boundary forces, we observe strain rates of the order 10^{-16}-10^{-15} s^{-1} that are caused by gravitational instabilities and specifically for this feedback system, which employs a maximum dominant grain-size of 2.5 cm for the rock salt. It becomes clear that pressure-solution creep is most dominant and stresses at 100 kPa, and below are to be expected. However, one has to keep in mind that a grain size growth at low stresses, which can lead to higher stresses, is not part of this model.

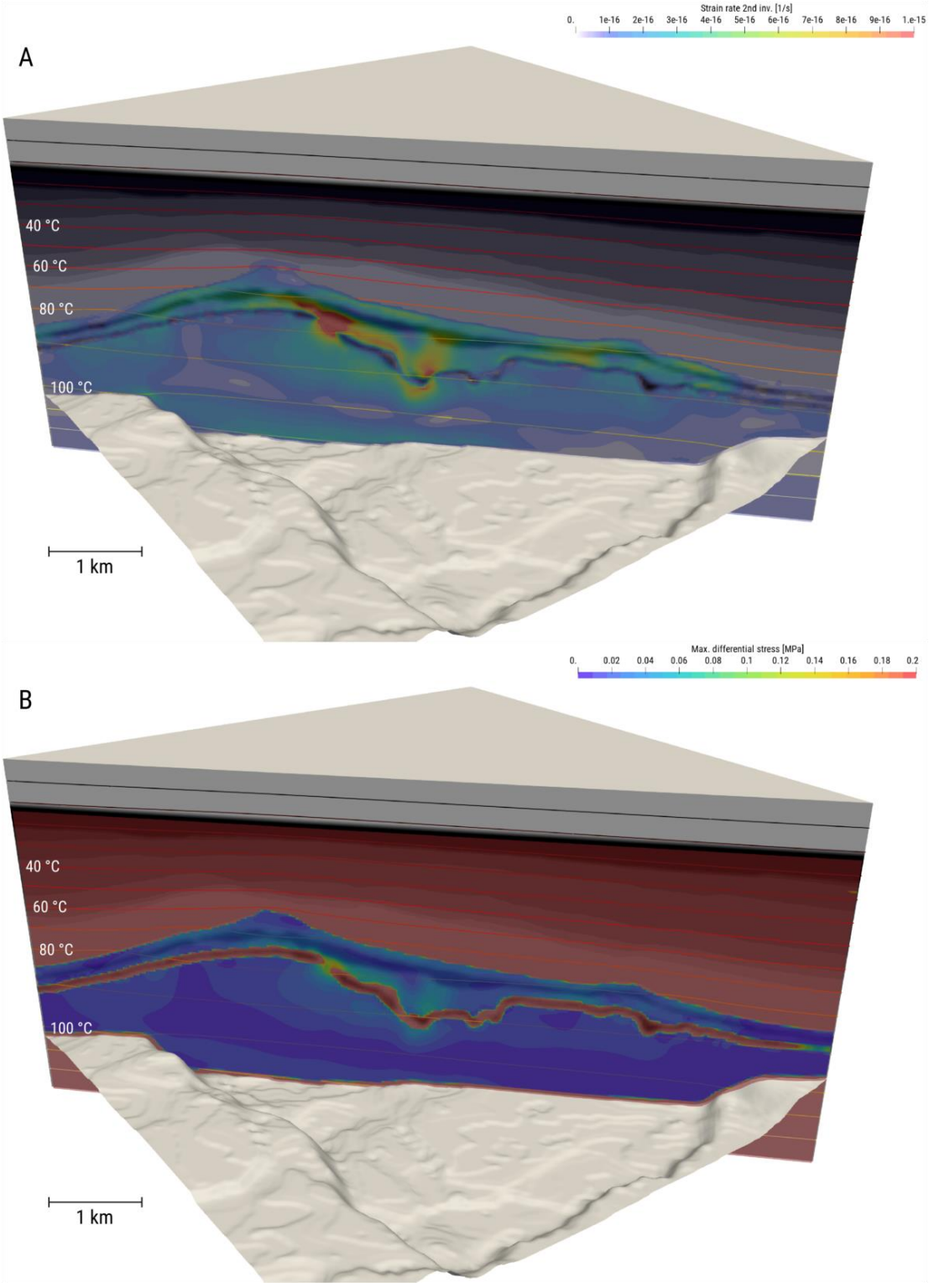

FIGURE 4.7

Strain rates (**A**) and differential stresses (**B**) resulting from a model with coupled PS-DC creep (d_{max} = 2.5 cm) in the absence of superimposed far-field tectonic deformation. Gray surface indicates the top of the basement and contour lines show the characteristic temperature distribution.

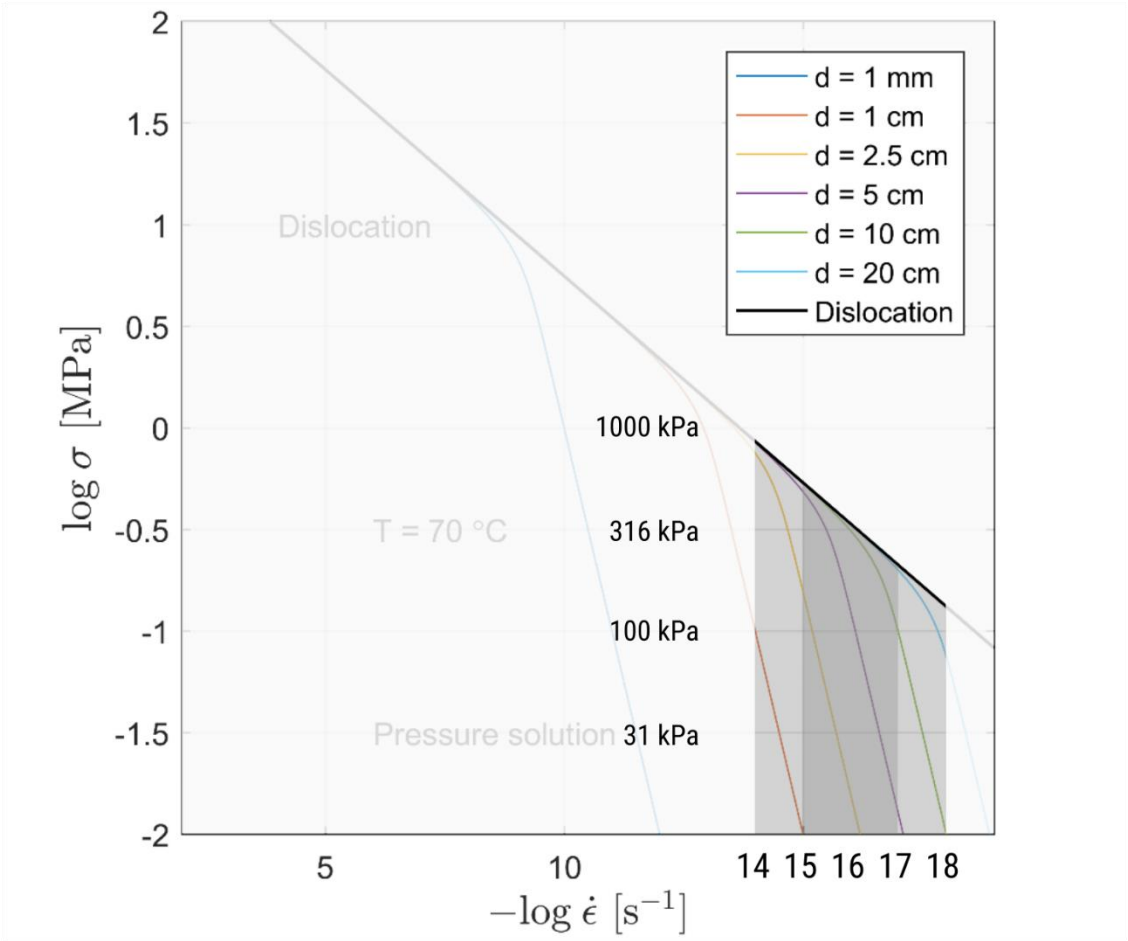

FIGURE 4.8

Adapted graph from Figure 3.8, but with shaded area indicating the actual ranges of strain rate and differential stress that we obtain for the model discussed in section 4.4.1 and Figure 4.7. Gray shaded area corresponds to strain-rate and stress ranges observed in the model. Noticeable differential stresses (> 10 kPa) that result from a coupled PS-DC creep, where the DC creep is not dominant, are associated with grain sizes larger than 1 cm.

4.4.2 Variations of the reference model with coupled PS-DC creep

To get a better overview of the value range of the differential stresses in salt rock when coupled PS-DC creep is applied, we examine a number of variations of the reference model described above (Figure 4.9). Figure 4.10a represents the reference model with a constant grain size (d_{max} = 2.5 cm) throughout the salt pillow. Exposing the model to a far-field extensional deformation results in higher differential stresses on the right flank of the salt pillow (Figure 4.9b,c). Figure 4.9c shows the case where we

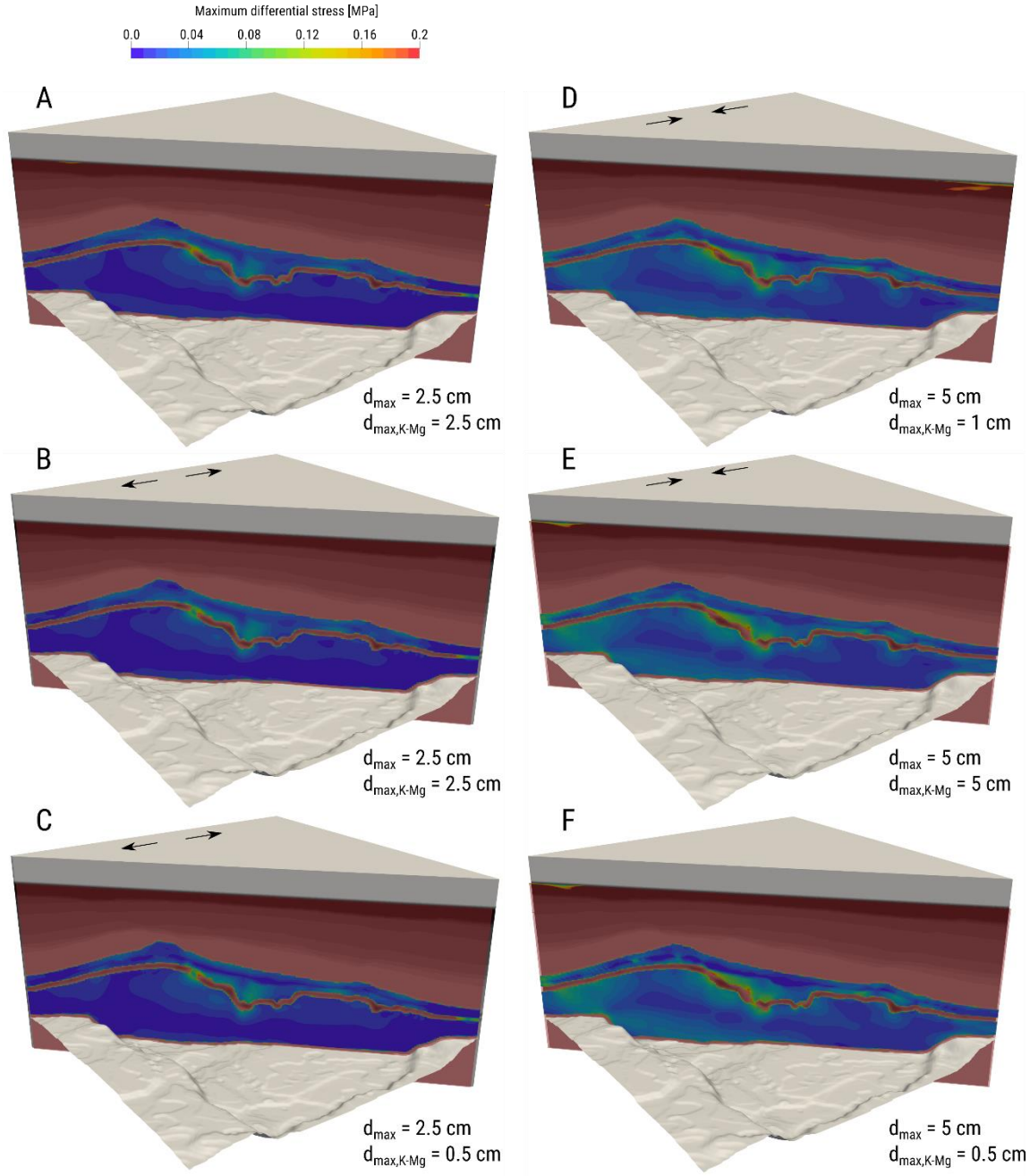

FIGURE 4.9

Comparison between the coupled PS-DC-creep reference model (Salt-DC[1], see Table 3.1) and model variations as absolute differential stress. If indicated by arrows, the models are subject to a far-field tectonic setting with imposed strain rates of 1×10^{-17} s^{-1}. **A:** Reference model (same as in Figure 4.7). Left column **(A-C)** are models with d_{max} = 2.5 cm. **C** is an exception with a smaller grain size for the K-Mg salt layer. Right column **(D-F)** contains models with d_{max} = 5 cm for the main salt but variable grain sizes for the K-Mg salt.

decrease the grain size for the K-Mg salt; this reduces the stress magnitude at the right flank of the salt pillow. In the right column of Figure 4.9, we show the changes that occur for double grain size (d_{max} = 5 cm). Subjecting the model to a far-field tectonic compression (Figure 4.9e, f) has a slight reducing effect on the stress state in the top of the salt pillow. We see this in comparison with Figure 4.9d, where no compression is applied and higher stresses occur. Otherwise, the stress pattern is very similar for all cases in Figure 4.9d-f. Overall, the change in K-Mg grain size has only a minor impact, apart from slightly reduced stresses at the right flank of the salt pillow. Much more important is the grain size of the main salt, which overall increases the stress magnitudes in the salt pillow. The amplification is particularly strong close to fault zones in the basement and in the vicinity of the anhydrite stringers.

4.4.3 Models with deactivated pressure solution creep

In the previous sections, we have seen that on the scale of a salt pillow, the resulting differential stresses occurring within the salt are well below 0.5 MPa when pressure solution creep is active. In this section, we consider the scenario of inactive PS creep and study the effect of various DC creep laws as well as internal heterogeneities, and tectonic strain on the internal stress state of the salt pillow.

As a reference, we choose a model with the dislocation creep law by (Wawersik and Zeuch 1986) (Salt-DC[2], see A typical combination of the dislocation creep (Wawersik and Zeuch 1986), and pressure solution creep (Spiers et al. 1990) with reasonable grain size (e.g., *d* = 1cm) results in a smooth transition shown in Figure 3.2. As expected, dislocation creep is active in the high-stress regime, while pressure solution creep is dominant in the low-stress regime. The influence of temperature is moderate. Note that for the dislocation creep described by (Wawersik and Zeuch 1986), the effective stress exponent is temperature-dependent. Hence on a log-log plot, slopes of the dislocation creep branch are slightly different. For other creep mechanisms, e.g. (Ter Heege et al. 2005b), this effect is not present.

Table 3.1). Moreover, we apply tectonic boundary conditions and extend the model with a low deformation rate of $5\times10^{-17}s^{-1}$ approximately perpendicular to the graben structure in the basement. The model results of the reference model and variations of the reference model are shown in Figure 4.10. Please note that the color scale now includes a wider range than before and scales up to 1 MPa. Figure 4.10a refers to the DC creep reference model. The reference model and all variations of the models show a characteristic concentration in differential stress at the top of the pillow structure with magnitudes > 0.6 MPa. As observed before, the presence of heterogeneities influences the overall pattern of stress distribution. If no heterogeneities are present in the pillow structure, one obtains the stress distribution shown in Figure 4.10f. High stresses concentrate in the top part of the pillow and decrease with depth, due to the increase in temperature. The Anhydrite stringers induce local anomalies in the stress field (Figure 4.10e) but do not significantly amplify the overall magnitude. A much more significant impact is the choice of the DC-salt rheology (see overview in Table 3.1), which affects the overall magnitude of the stress (Figure 4.10a, c, d).

Figure 4.11 helps to identify the relative differences between the DC-creep reference model and its variations. We see that the Salt-DC^4 creep rheology by (Bräuer et al. 2011b) is the DC-creep rheology that overall results in the highest stress amplitudes and that the Salt-DC^3 creep (Ter Heege et al. 2005b) still creates higher stresses than the reference Salt-DC^2 creep by (Wawersik and Zeuch 1986). This comparative view also illustrates the limited impact of glacial (un-)loading (Figure 4.11d) on the present-day stress state relative to the effect of other modifications to the reference model. For example, an increase in far-field tectonic strain-rate causes an amplification to the stresses in extreme locations (flanks and top), which is demonstrated with the comparison in Figure 4.11a, where the amplification of the reference model stress is visualized relative to a model that is subject to decreased tectonic strain rate ($10^{-17}\ s^{-1}$). The presence of a K-Mg layer results in a stress focusing effect, which localizes stresses in the upper parts of the pillow (Figure 4.11e).

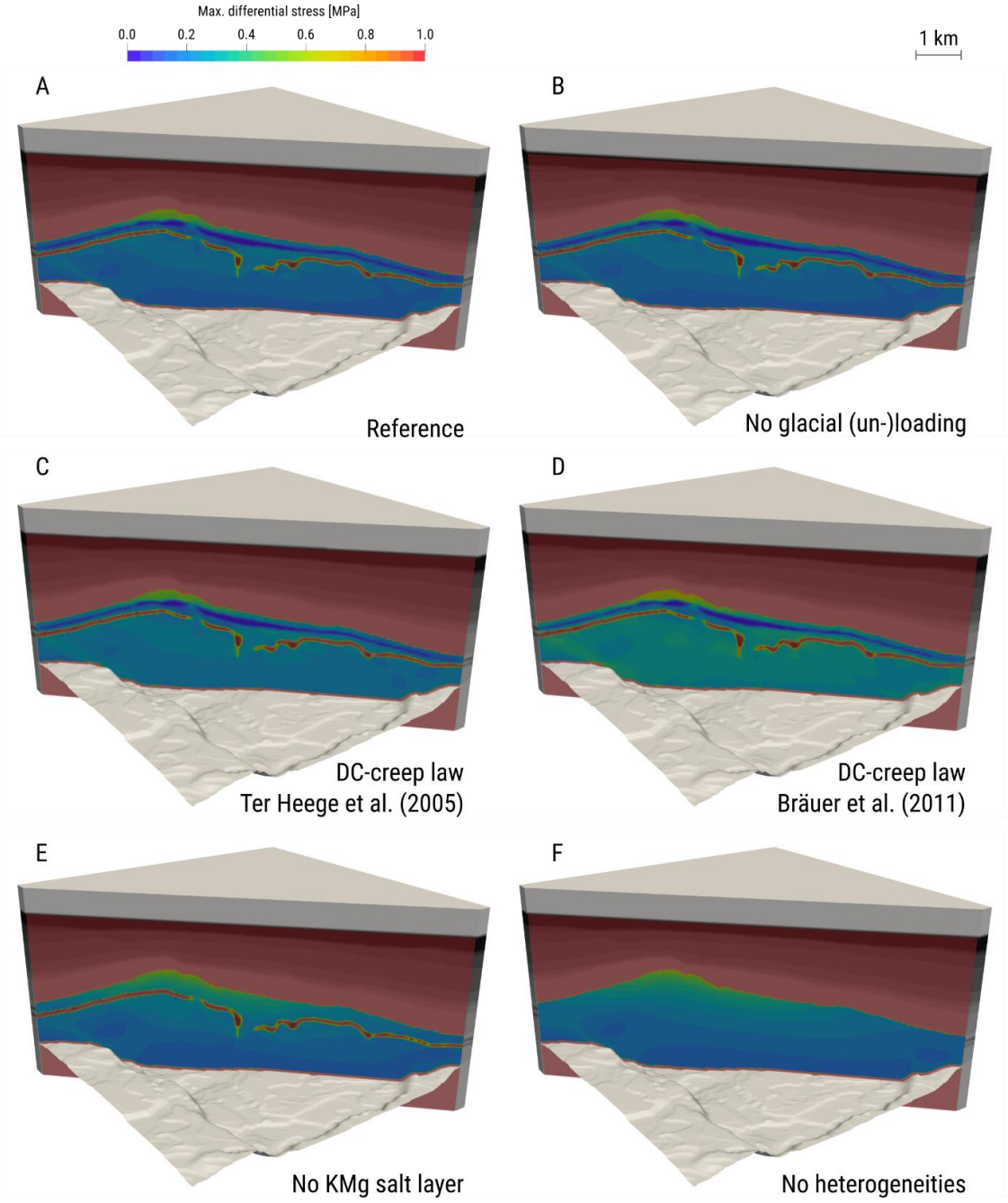

FIGURE 4.10

Comparison between DC-creep reference model (Salt-DC[2], see Table 3.1) and model variations shown as absolute values of differential stress. All models are subject to a far-field extensional tectonic setting with imposed strain rates of 5×10^{-17} s^{-1}. **A:** Reference model (Salt-DC[2], (Wawersik and Zeuch 1986)). **B:** Same but without the effect of additional loading during the latest ice age. **C:** Model with different DC-creep law (Salt-DC[3], (Ter Heege et al. 2005b)). **D:** Model with different DC-creep law (Salt-DC[4], (Bräuer et al. 2011b)). **E:** Similar to A but without a weak K-Mg salt layer. **F:** Similar to A but without intra-salt heterogeneities.

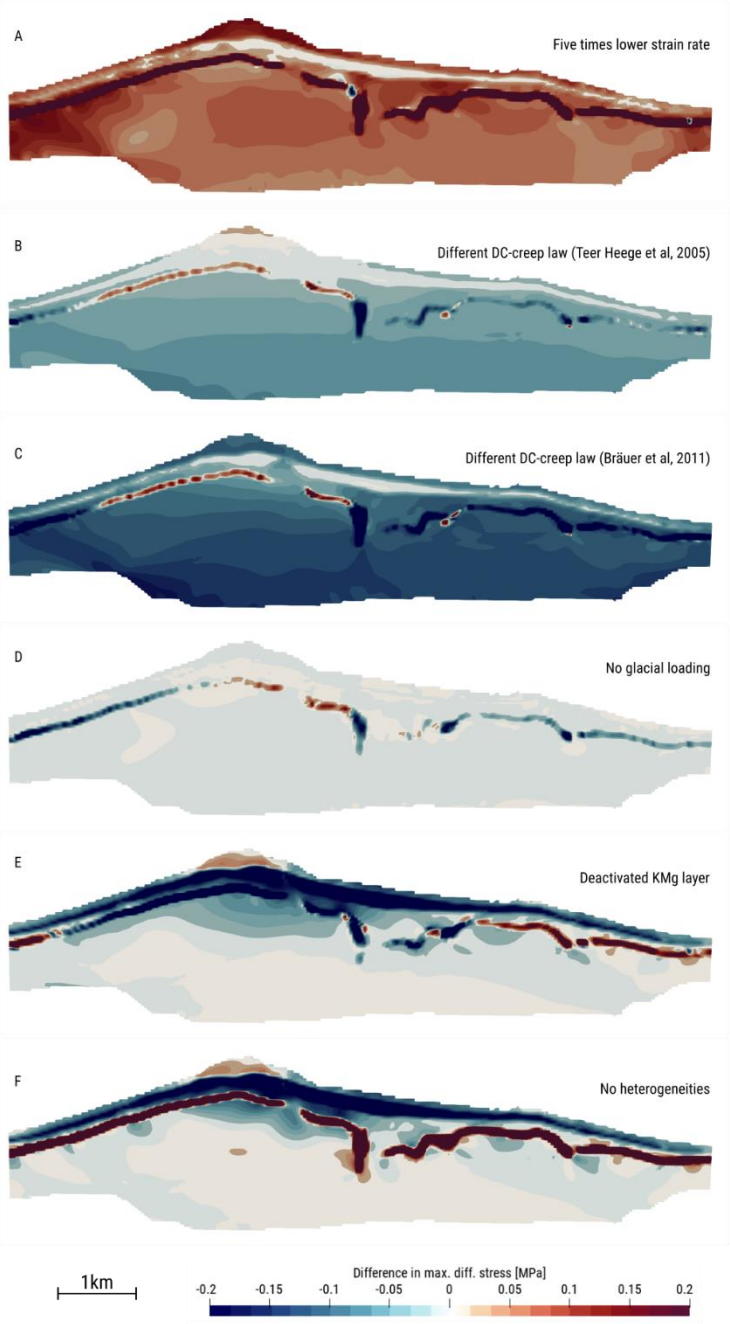

FIGURE 4.11

Comparison of the DC-creep reference model and alternative models. Colors indicate the difference in maximum differential stress. Red colors indicate higher stresses in the reference model; blue colors denote higher stresses in the comparative model. **A:** Relative changes of the reference model compared to a model with an extension rate that is five times lower. **B&C:** Relative changes compared to models with different DC-creep laws. **D:** Relative change in stress compared to a model without the effect of glacial (un-)loading. **E**: Difference to a model without a weak K-Mg-salt layer. **F:** Relative change compared to a model without heterogeneities.

4.4.4 The effect of glacial loading: Coupled PS-DC creep models

To examine the effect of glacial loading on the salt-internal stress state, we compare models with and without glacial loading and unloading for different end-member rheologies. In Figure 4.12, we illustrate this comparison for a coupled PS-DC creep scenario with a grain size of 2.5 cm, and in Figure 4.13, a similar comparison is shown for DC creep only. For all models, we apply a very low far-field tectonic strain rate with a magnitude of 10^{-17} s^{-1} to mimic a minimum amount of tectonic activity.

In the case of a coupled PS-DC creep, the differences within the salt are negligible. Soon after the full retreat of the ice shield at 130 kyrs, we observe higher differential stresses at the very top of the pillow, but also in the vicinity of the stringers and close to sharp edges in the basement topography. However, the differences in differential stress vanish quickly after the end of the glacial period. Stress differences within the stringers and at the boundary of the salt structures can be explained by minor geometrical offsets due to differences in vertical loading. In conclusion, we do not observe any effect of glacial loading for this particular setting and the chosen PS-DC salt rheology.

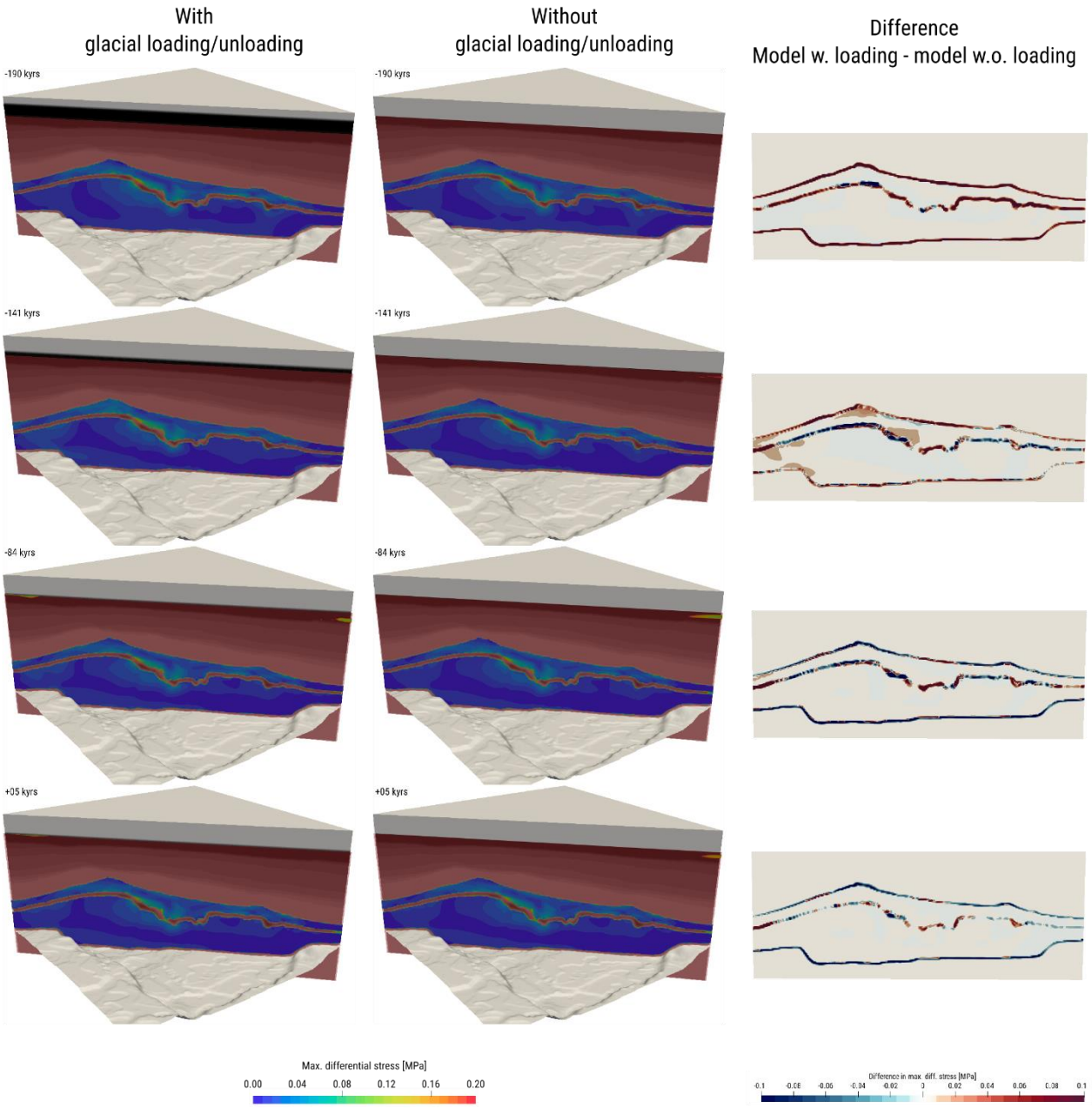

FIGURE 4.12

The effects of glacial loading examined for models where a combined PS-DC creep rheology (dmax = 2.5cm) is applied. The extent of the ice sheet is indicated with dark shading. Left/Center: Models with and without glacial loading and unloading. Colors represent maximum differential stress. Right: Difference in maximum differential stress along a cross-section through the 3D models.

4.4.5 The effect of glacial loading: DC creep models

We now consider a similar comparison, but for models with a deactivated pressure-solution creep (Figure 4.13) to mimic a situation in which grain boundary diffusivity is low. Compared to Figure 4.12, we adapted the color scale to higher magnitudes. As in the previous comparison, we find virtually no differences in the differential stress before the Ice Age. Again, there are differences at the boundaries of the salt structure and within the stringers, which result from differences in vertical loading. At the end of the glacial period, the stress residuals are positive and reach up to 0.1-0.2 MPa. At 80 kyrs, the residual effects largely disappear, the polarity of the anomalies partly changes, and the magnitude further decays up to the present-day. However, at present-day conditions, we do observe a residual stress concentration at the very top of the salt pillow structure. It is a negative deviation compared to the reference model, which was not affected by a glacial period.

Overall, the residual magnitudes are much larger compared to the first scenario with coupled PS-DC creep. Notable residual stresses induced by glacial loading and unloading are likely linked to exposed locations within the salt structure, for example, the top of the pillow. Here, the differential stress magnitude at the top of the pillow differs between 15% and 30% from its original value. This corresponds to differential stresses of 40-80 kPa.

4.4.6 Summary: Differential stresses induced by glacial loading

In summary, glacial loading may induce differential stresses within the salt structure at certain locations. However, this is only true when pressure-solution creep is mostly inactive. For combined PS-DC creep models, the differential stress induced by glacial loading is negligible. Provided that the salt dominantly deforms in a dislocation-creep manner, glacial (un-)loading may induce differential stresses between 50 and 100 kPa.

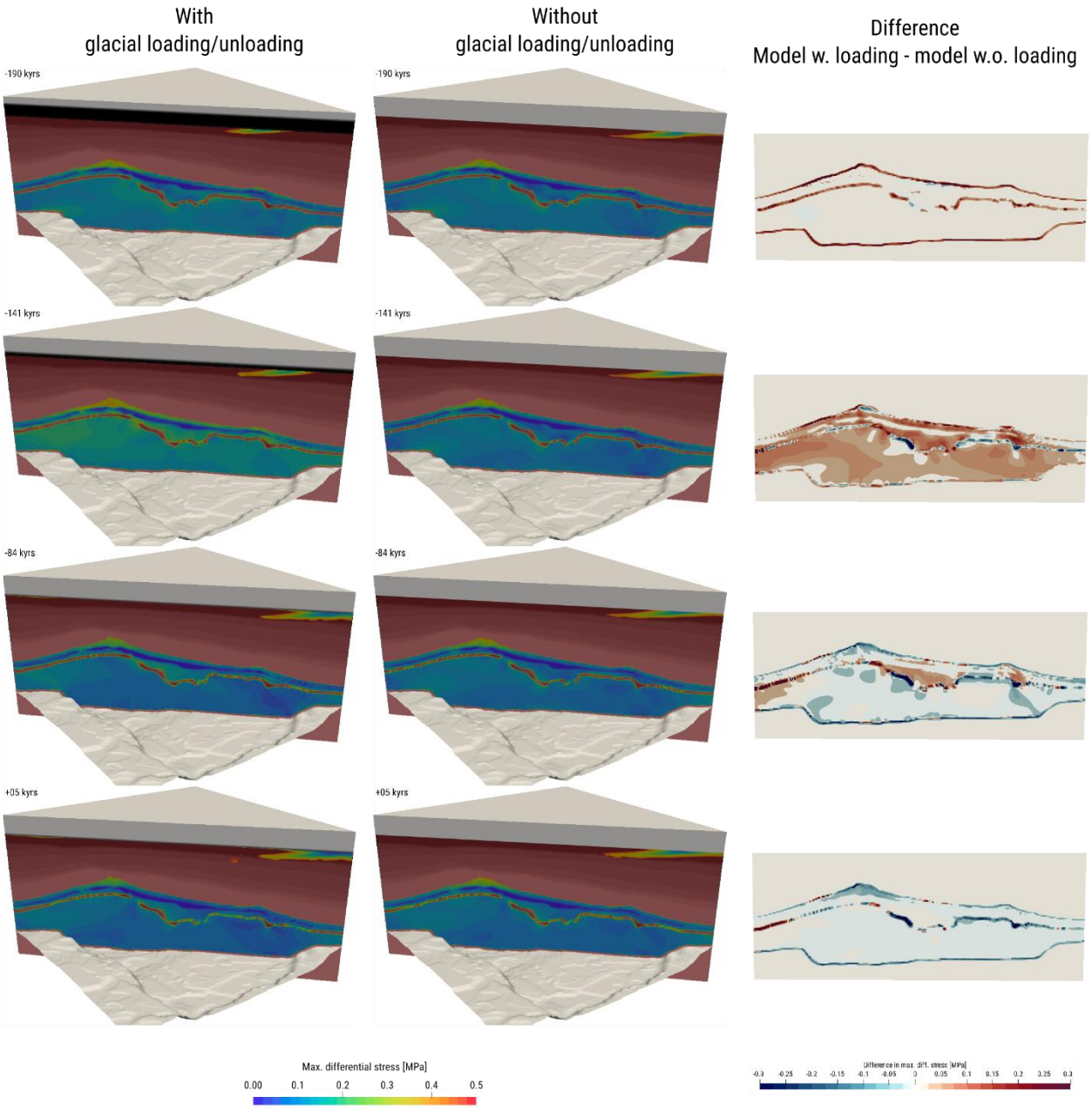

FIGURE 4.13

Effects of glacial loading examined for models where only a DC-creep (Salt-DC^2) rheology is applied. The extent of the ice sheet is indicated with dark shading. Basement topography is shown as a light grey surface. Left/Center: Models with and without glacial loading and unloading. Colors represent maximum differential stress. Right: Difference in maximum differential stress along a cross-section through the 3D models.

4.4.7 Summary and key observations

[1] For models of the salt pillow structure with coupled pressure solution and dislocation (PS-DC) creep, we obtain maximum differential stresses that are typically below 0.5 MPa.

[2] Whenever pressure solution creep is deactivated, the resulting stresses are higher and reach up to 0.7-0.8 MPa, depending on which creep law is employed. Highest differential stresses are associated with the DC^4-creep law (BGRa, Bräuer et al. 2011b)

[3] We obtain maximum stress magnitudes near the top of the salt pillow structure, which is a robust feature, that was observed in all models.

[4] Stresses induced by glacial (un-)loading may only contribute to the order of 100 kPa, but only if PS creep not active, which is, in principle, testable using microstructural observations.

[5] Different DC-creep laws result in a change in the stress patterns.

[6] Changes in the tectonic rate amplify the stress magnitude but have almost no effect on the relative stress patterns within the salt body.

[7] Internal heterogeneities induce local stress changes, as do faults in the basement topography. Within the scope of the pillow model, we find that locally induced stress anomalies have length scales of approximately 1km.

4.5 Salt wall model

So far, we examined the internal stress state for a salt pillow structure. Here, we study the internal stress state of a salt dome or wall structure. Figure 4.14 shows the DC-creep reference model of the salt wall geometry, which employs the Salt-DC[2] rheology (see A typical combination of the dislocation creep (Wawersik and Zeuch 1986), and pressure solution creep (Spiers et al. 1990) with reasonable grain size (e.g., d = 1cm) results in a smooth transition shown in Figure 3.2. As expected, dislocation creep is active in the high-stress regime, while pressure solution creep is dominant in the low-stress regime. The influence of temperature is moderate. Note that for the dislocation creep described by (Wawersik and Zeuch 1986), the effective stress exponent is temperature-dependent. Hence on a log-log plot, slopes of the dislocation creep branch are slightly different. For other creep mechanisms, e.g. (Ter Heege et al. 2005b), this effect is not present.

Table 3.1, (Wawersik and Zeuch 1986)). Pressure solution creep is deactivated to simulate a situation with low grain boundary diffusivity. As before, the white solid surface indicates the basement topography. We represent the top salt with contour lines to illustrate the three-dimensional structure of the salt wall for orientation purposes. Figure 4.14a shows maximum differential stress, where stresses higher than 0.5 MPa are clipped to focus on salt-internal stress ranges. Gray shadings in the background indicate the lithological units employed.

Partly because of the absence of internal heterogeneities, the stress distribution looks homogeneous and only gradually changes in the vertical direction, from low values towards the basement to high values towards the top of the wall structure (Figure 4.14a). This behavior is closely related to the temperature distribution within the salt and reflects the temperature-dependent Arrhenius type of DC-creep rheology. Laterally, except for the right flank of the salt wall, we only observe insignificant variations of maximum differential stress. Though, at the right flank of the salt wall,

just at the interface towards the overburden, we obtain higher stress, which is associated with high strain rates (Figure 4.14b). Overall the high strain rates mostly concentrate at the right flank of the salt wall.

In the following, we first provide an overview of the absolute differential stresses obtained for all models and subsequently refer to the relative differences with respect to the reference model described above. First, we focus on the models with coupled PS-DC-creep. As noted before, the key parameter of coupled PS-DC creep controlling the stress is the maximum grain size. For reference, we choose d_{max} = 2.5 cm. Overall, the differential stress magnitudes obtained here are much lower (< 80 kPa) than in the

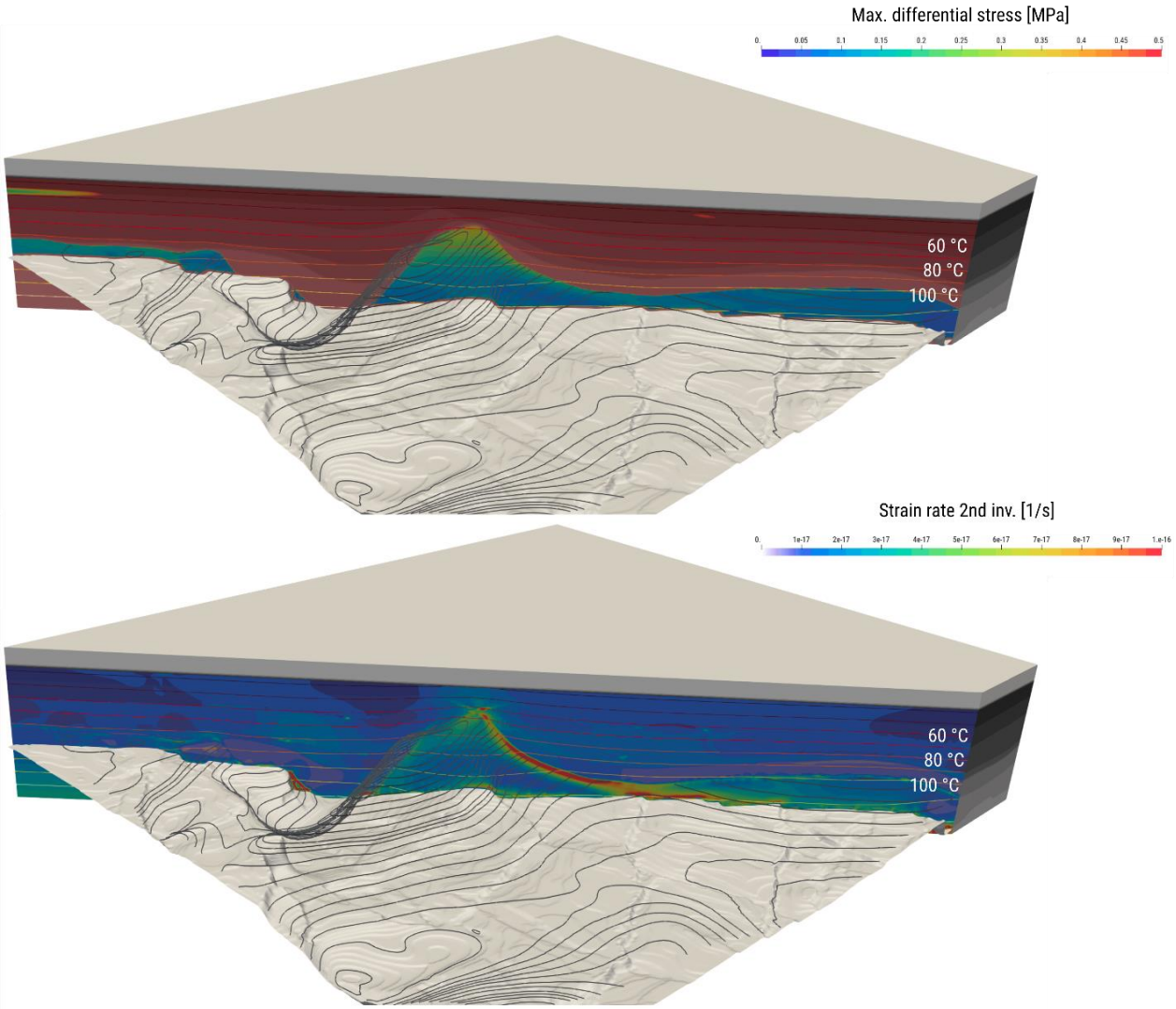

FIGURE 4.14

DC-creep reference model of a salt wall. PS-creep is deactivated to mimic a situation with low grain boundary diffusivity. The white surface shows the basement topography, and black contour lines specify the top salt interface. Colored contours on the cross-section show the steady-state temperature of the model. **A:** Maximum differential stress in MPa; Color scale range is larger than in Figure 4.15a. **B:** Strain rates in s^{-1}.

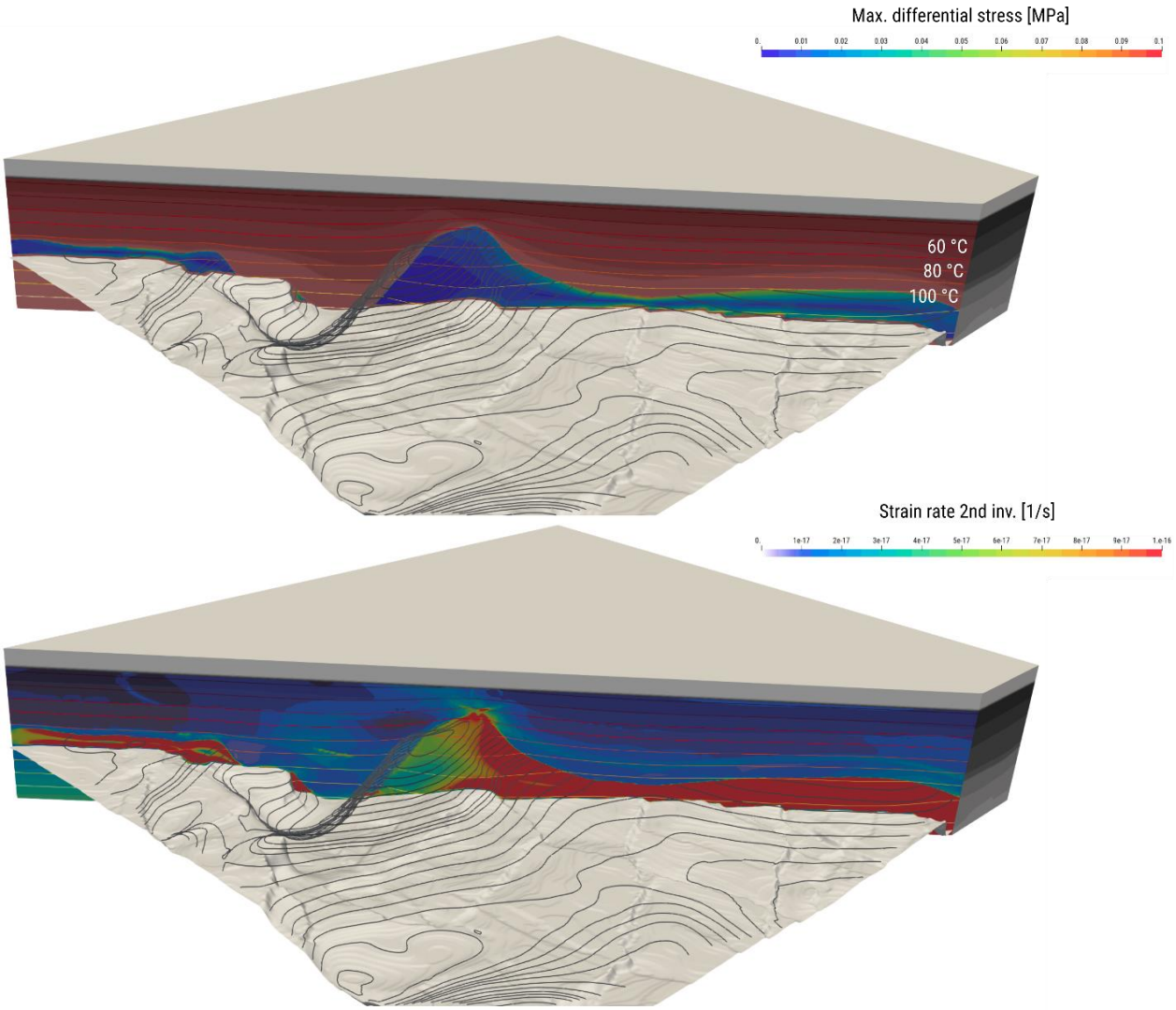

FIGURE 4.15

Coupled PS-DC-creep reference model of a salt wall. The white surface shows the basement topography, and black contour lines specify the top salt interface. Colored contours on the cross-section show the steady-state temperature of the model. **A:** Maximum differential stress in MPa; Note that the color scale range is smaller than Figure 4.14a. **B:** Strain rates in s^{-1}.

DC-creep reference model. However, relatively seen, the PS-DC creep model shows a high lateral stress contrast (Figure 4.15a). Differential stresses are focussed on the right flanks of the diapir and within the flat bedded part. In the flat-bedded parts, we obtain a stress concentration towards the salt-sediment contact. Strain rates are elevated at the right flank and in the flat-bedded parts (Figure 4.15b). The pattern is similar to the strain rate pattern observed for the DC creep reference model, but absolute values are higher than before.

4.5.1 Changes due to larger grain size and tectonic deformation

From theory, we expect overall higher stresses for larger grain sizes. So, if we double the maximum grain size (d_{max} = 5 cm) compared to the current reference model (Figure 4.16a), the stress pattern changes. Stress concentrations at the right flank remain, but the differential stress at the base of the salt wall is enhanced (Figure 4.16b), and we obtain elevated stresses at the top and bottom interface of the salt. In the next step, we test the impact of far-field tectonic deformation. Figure 4.16c shows the same model as in Figure 4.16a, but with the difference that this model is exposed to tectonic compression of a rather small strain rate (10^{-17} s^{-1}). We examine the same scenario, but with a tectonic extension of the same rate in Figure 4.16d. In the case of compression, we obtain a small reduction of stresses, whereas, overall, the stresses increase in case of tectonic extension. However, we find that none of the tectonic boundary conditions influence the general pattern of the salt internal differential stress.

4.5.2 The effect of different DC-creep laws

In order to evaluate the possible variability in maximum differential stress as a function of DC-creep law, we provide an overview with examined models where PS-creep was explicitly deactivated (Figure 4.17). The DC-creep reference models (Salt-DC[2], (Wawersik and Zeuch 1986) A typical combination of the dislocation creep (Wawersik and Zeuch 1986), and pressure solution creep (Spiers et al. 1990) with reasonable grain size (e.g., *d* = 1cm) results in a smooth transition shown in Figure 3.2. As expected, dislocation creep is active in the high-stress regime, while pressure solution creep is dominant in

the low-stress regime. The influence of temperature is moderate. Note that for the dislocation creep described by (Wawersik and Zeuch 1986), the effective stress exponent is temperature-dependent. Hence on a log-log plot, slopes of the dislocation creep branch are slightly different. For other creep mechanisms, e.g. (Ter Heege et al. 2005b), this effect is not present.

Table 3.1) is given in Figure 4.17a, where we obtain the highest stress (~ 0.5 MPa) at the tip of the wall. If we employ another DC-creep (Salt-DC[3], (Ter Heege et al. 2005b) A typical combination of the dislocation creep (Wawersik and Zeuch 1986), and pressure solution creep (Spiers et al. 1990) with reasonable grain size (e.g., *d* = 1cm) results in a smooth transition shown in Figure 3.2. As expected, dislocation creep is active in the high-stress regime, while pressure solution creep is dominant in the low-stress regime. The influence of temperature is moderate. Note that for the dislocation creep described by (Wawersik and Zeuch 1986), the effective stress exponent is temperature-dependent. Hence on a log-log plot, slopes of the dislocation creep branch are slightly different. For other creep mechanisms, e.g. (Ter Heege et al. 2005b), this effect is not present.

Table 3.1), we see that stress pattern changes (Figure 4.17b). Stresses are, overall, slightly higher (+0.05 MPa) compared to the reference model except at the top of the wall, where only values up to 0.45 MPa are obtained. In case of the BGRa DC-creep (Salt-DC[4], A typical combination of the dislocation creep (Wawersik and Zeuch 1986), and pressure solution creep (Spiers et al. 1990) with reasonable grain size (e.g., *d* = 1cm) results in a smooth transition shown in Figure 3.2. As expected, dislocation creep is active in the high-stress regime, while pressure solution creep is dominant in the low-stress regime. The influence of temperature is moderate. Note that for the dislocation creep described by (Wawersik and Zeuch 1986), the effective stress exponent is temperature-dependent. Hence on a log-log plot, slopes of the dislocation creep

branch are slightly different. For other creep mechanisms, e.g. (Ter Heege et al. 2005b), this effect is not present.

Table 3.1) from (Bräuer et al. 2011b), the stress pattern is similar to Salt-DC^3, which is due to the fact that both power-laws employ the same mathematical form that is different from the one used in Salt-DC^2 (see section 3.1). In terms of magnitude, we observe differential stresses of ~0.65 MPa, again at the top and the right flank of the wall. Those magnitudes are the highest we observe and mark the upper limit for the tectonic strain rates employed in this numerical study.

4.5.3 The effect of tectonic deformation

Figure 4.18 summarizes the stress obtained for different tectonic loading conditions. For all cases shown, we obtain a stress concentration at the top of the salt dome. If zero tectonic strain is applied, we reach magnitudes of up to 0.4 MPa (Figure 4.18a). The compressional tectonic setting decreases the maximum values to approximately 0.3 MPa (Figure 4.18b). In contrast, we obtain differential stress magnitudes of up to 0.5 MPa for an extensional tectonic setting and similar rates (Figure 4.18c). We find differential stress magnitudes greater than 0.5 MPa when using extensional strain boundary conditions on both sides of the model domain, which effectively corresponds to a diagonal extension.

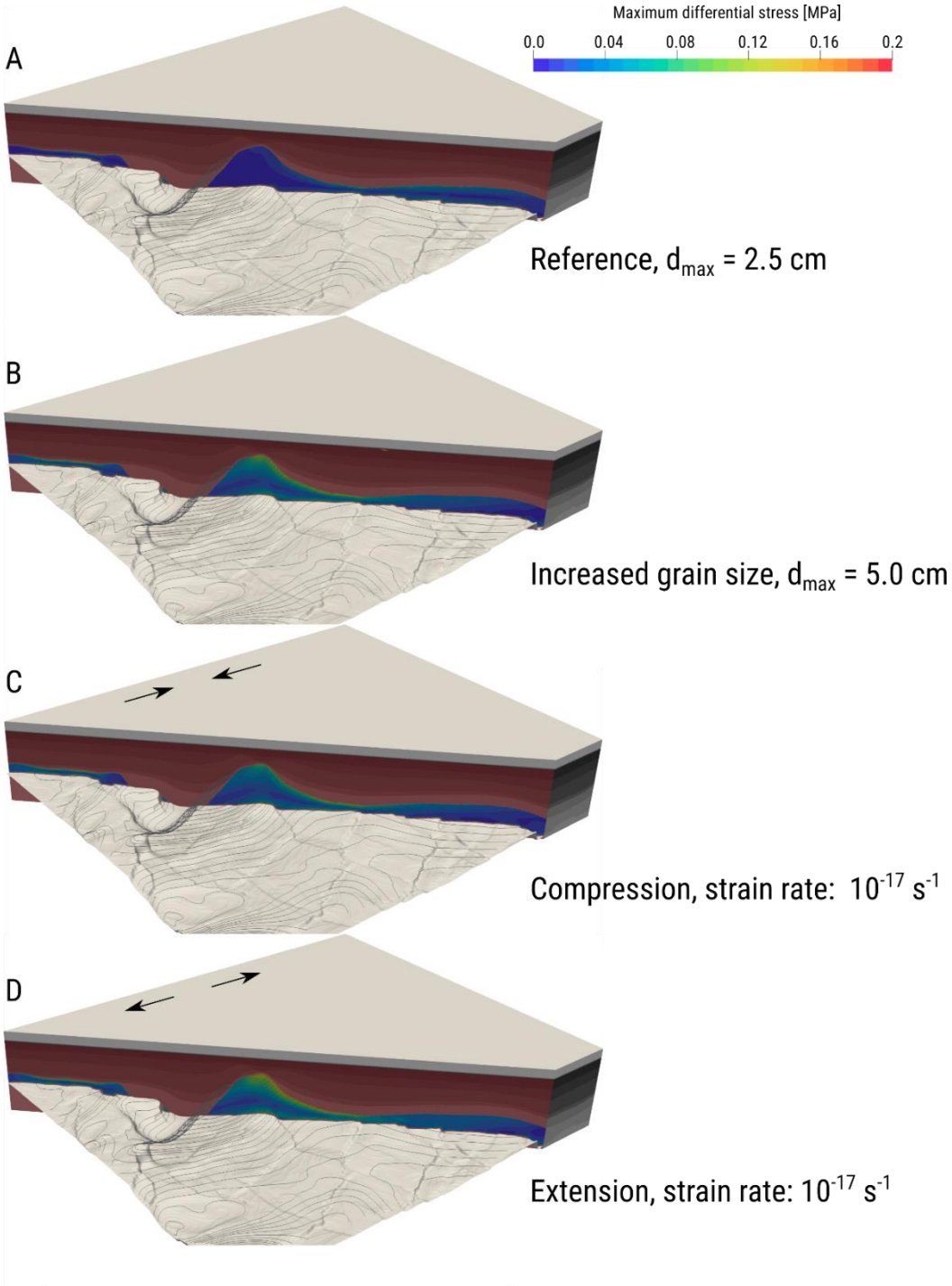

FIGURE 4.16

Absolute changes in maximum differential stress for various conditions relative to a reference model with coupled PS-DC creep (Salt-PS[1]-DC[2], see A typical combination of the dislocation creep (Wawersik and Zeuch 1986), and pressure solution creep (Spiers et al. 1990) with reasonable grain size (e.g., *d* = 1cm) results in a smooth transition shown in Figure 3.2.

As expected, dislocation creep is active in the high-stress regime, while pressure solution creep is dominant in the low-stress regime. The influence of temperature is moderate. Note that for the dislocation creep described by (Wawersik and Zeuch 1986), the effective stress exponent is temperature-dependent. Hence on a log-log plot, slopes of the dislocation creep branch are slightly different. For other creep mechanisms, e.g. (Ter Heege et al. 2005b), this effect is not present.

Table 3.1). Arrows indicate the direction of far-field tectonic strain applied to the models. **A:** Reference model with coupled PS-DC creep. **B:** Same as in A but with doubled grain size. **C:** Same as A but within a compressional tectonic regime. **D:** Same as A but for an extensional tectonic regime with the same far-field deformation rate as C**.**

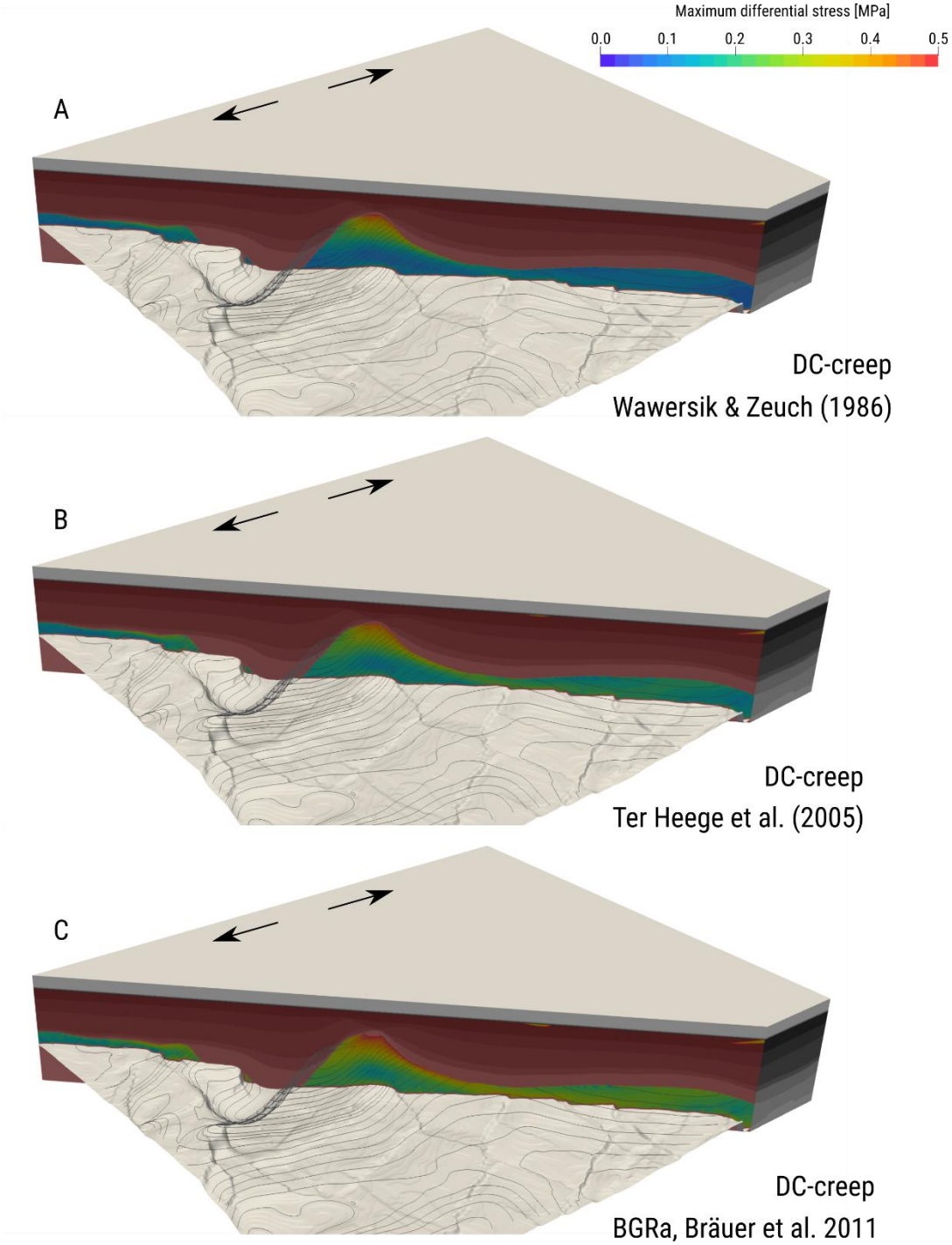

FIGURE 4.17

Variations in maximum differential stress resulting from different DC-creep laws. All models are subject to tectonic extension with a far-field deformation rate of 10^{-17} s^{-1}. **A:** Salt-DC[2] creep (see

A typical combination of the dislocation creep (Wawersik and Zeuch 1986), and pressure

solution creep (Spiers et al. 1990) with reasonable grain size (e.g., *d* = 1cm) results in a smooth transition shown in Figure 3.2. As expected, dislocation creep is active in the high-stress regime, while pressure solution creep is dominant in the low-stress regime. The influence of temperature is moderate. Note that for the dislocation creep described by (Wawersik and Zeuch 1986), the effective stress exponent is temperature-dependent. Hence on a log-log plot, slopes of the dislocation creep branch are slightly different. For other creep mechanisms, e.g. (Ter Heege et al. 2005b), this effect is not present.

Table 3.1, (Wawersik and Zeuch 1986)). **B:** Salt-DC[3] creep (see A typical combination of the dislocation creep (Wawersik and Zeuch 1986), and pressure solution creep (Spiers et al. 1990) with reasonable grain size (e.g., *d* = 1cm) results in a smooth transition shown in Figure 3.2. As expected, dislocation creep is active in the high-stress regime, while pressure solution creep is dominant in the low-stress regime. The influence of temperature is moderate. Note that for the dislocation creep described by (Wawersik and Zeuch 1986), the effective stress exponent is temperature-dependent. Hence on a log-log plot, slopes of the dislocation creep branch are slightly different. For other creep mechanisms, e.g. (Ter Heege et al. 2005b), this effect is not present.

Table 3.1, (Ter Heege et al. 2005b)). **C:** Salt-DC[4] creep (see A typical combination of the dislocation creep (Wawersik and Zeuch 1986), and pressure solution creep (Spiers et al. 1990) with reasonable grain size (e.g., *d* = 1cm) results in a smooth transition shown in Figure 3.2. As expected, dislocation creep is active in the high-stress regime, while pressure solution creep is dominant in the low-stress regime. The influence of temperature is moderate. Note that for the dislocation creep described by (Wawersik and Zeuch 1986), the effective stress exponent is temperature-dependent. Hence on a log-log plot, slopes of the dislocation creep branch are slightly different. For other creep mechanisms, e.g. (Ter Heege et al. 2005b), this effect is not present.

Table 3.1, (Bräuer et al. 2011b)).

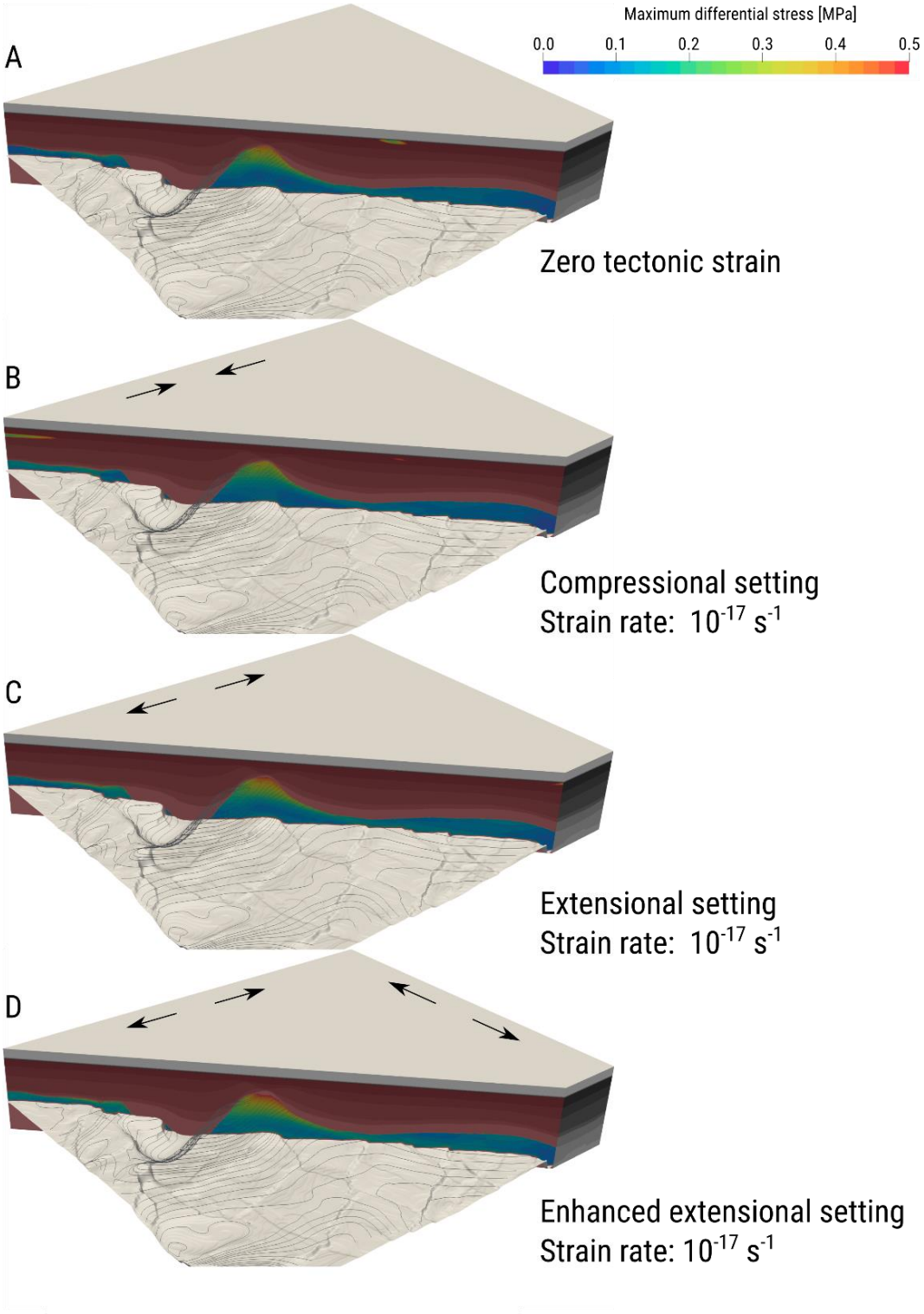

FIGURE 4.18

Models with DC-creep and different tectonic loading. **A:** Zero tectonic strain. **B**&**C:** Model with a compressional and extensional setting, respectively. **D:** Enhanced extensional tectonic strain, where deformation is applied to either side of the model.

4.5.4 Relative changes in maximum differential stress

In order to illustrate the entire variation in maximum differential stress for the salt wall type models, we provide a summary with relative changes in differential stress in Figure 4.19. The stress changes are relative changes with respect to the DC-creep reference model (Figure 4.14). We first compare the reference model with models of coupled PS-DC creep. As expected from theory, the magnitudes in differential stress of pure DC-creep are much higher. On average, we find an increase of 130 kPa (Figure 4.19a,b). In Figure 4.19c-e, we compare the reference model with models of the same rheology, but different loading boundary conditions. Figure 4.19c shows the effect of enhanced tectonic loading (five-times enhanced rate) and in Figure 4.19d, we visualize a scenario with reversely directed tectonic loading of the same magnitude. Whereas we find higher stress at the top of the wall (~100 kPa) for an increased extension rate, we note that compressional loading only slightly increases the differential stress at the center, but decreases the stress magnitude at the top and right flank of the salt wall.

Overall, the extensional setting results in enhanced differential stress, about 50 kPa on average. Again, we find the highest differences at the top of the salt wall. However, within the dome center, the extension can also result in a decrease in differential stress. For comparison, we also show the impact of glacial (un-)loading in this context (Figure 4.19e). We find that the impact of glacial (un-)loading on the state of stress is not as significant as other modifications to the rheology and tectonic boundary conditions (< 50 kPa). The most significant stresses induced by the additional loading during the glacial period occur at the top part of the salt wall.

In Figure 4.19f,g and also in Figure 4.20, we show the impact of different DC-creep laws on the maximum differential stress. Whereas the BGRa DC-creep (Salt-DC^4, Bräuer et al. 2011b) generally results in higher stresses (75-150kPa), employing the DC-creep law by

(Ter Heege et al. 2005b) results in less enhanced stresses (75 kPa) in the flat parts of the wall and similar stress magnitudes in the tip of the wall.

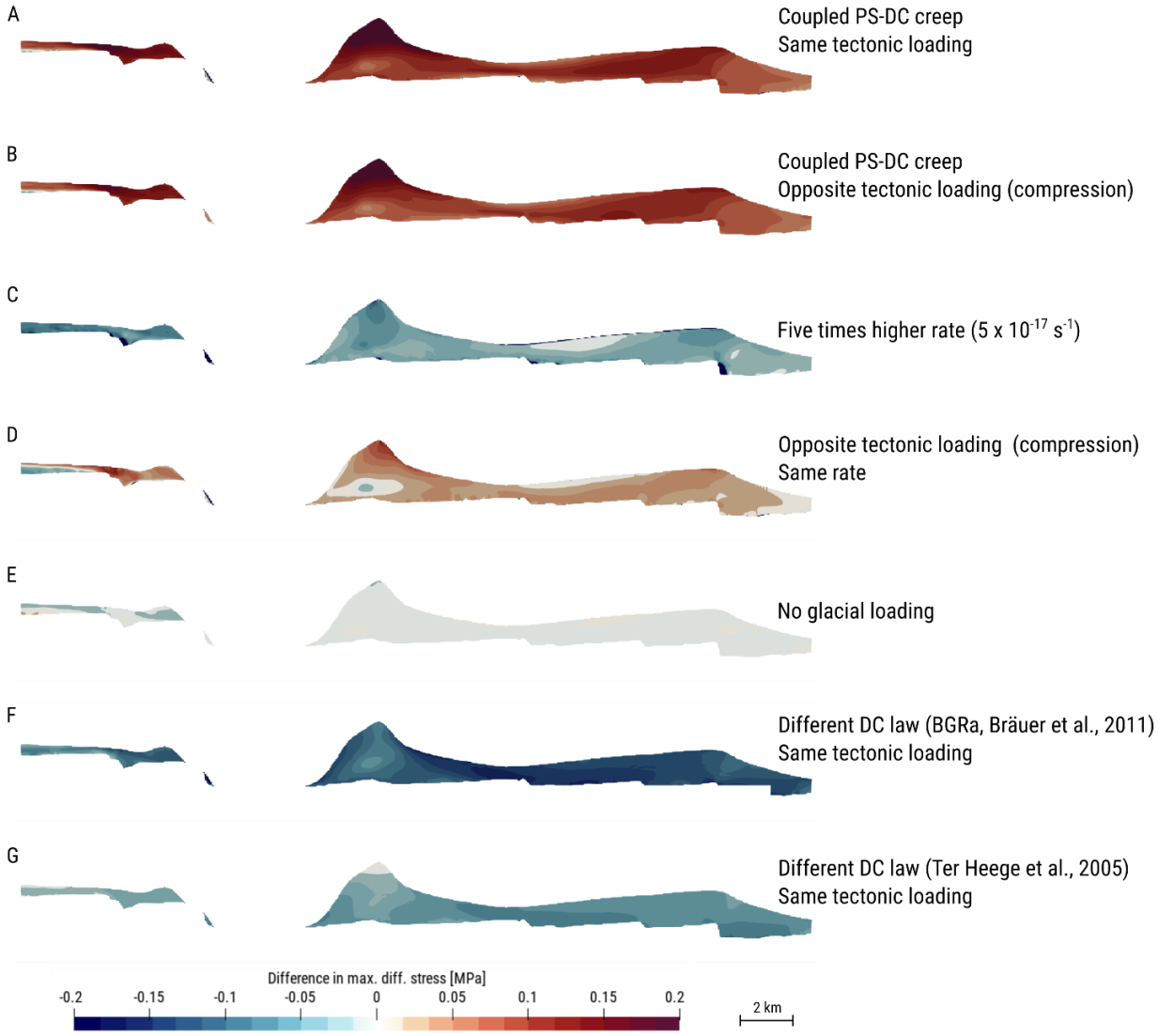

FIGURE 4.19

Differences in differential stress with respect to the reference DC-creep model. Cross-sections are similar to those of other figures with a 3D perspective. Red colors indicate elevated maximum differential stress, relative to the DC-creep reference model. Blue colors show areas with smaller differential stress compared to the reference model. **A & B** show the differences to models with coupled PS-DC creep (d_{max} = 5 cm) for similar directed and opposite directed tectonic loading, respectively. **C-E** show comparison with results obtained by models with the same DC-creep law but different loading, i.e., extensional tectonic loading with five times higher rate (**C**), compressional tectonic loading with the

equivalent rate (**D**), and without glacial loading (**E**). **F & G** show differences in differential stress between the reference model and models of other DC-creep laws, respectively.

4.5.5 The effect of glacial loading for the salt wall scenario

In this final section related to the salt wall model, we examine the effect of glacial loading on the present-day stress state of the salt wall and also look at the differences in stress evolution, for both, pure DC-creep (Figure 4.20) and coupled PS-DC creep (Figure 4.21).

Considering the effect of glacial loading on the DC-creep model at present-day, we obtain residual stresses < 0.1 MPa mostly in the top and at the right flank of the salt wall. The polarity of this residual stress is negative, which means that the model that does not contain the ice sheet has higher differential stresses in those locations at present-day. From the evolution of the stress state, we see that this was not always the case. For example, just after the end of the deglaciation period (140 kyrs ago), we obtain strongly positive residual differential stresses, which turn into negative residual differential stresses 50 kyrs later (90 kyrs ago), which can likely be attributed to the interaction between the salt wall and the poro-visco-elastoplastic host rocks.

For the coupled PS-DC creep (Figure 4.21), we find similar trends and polarities, but the magnitudes of the residual differential stress at present-day are negligible (< 0.005 MPa).

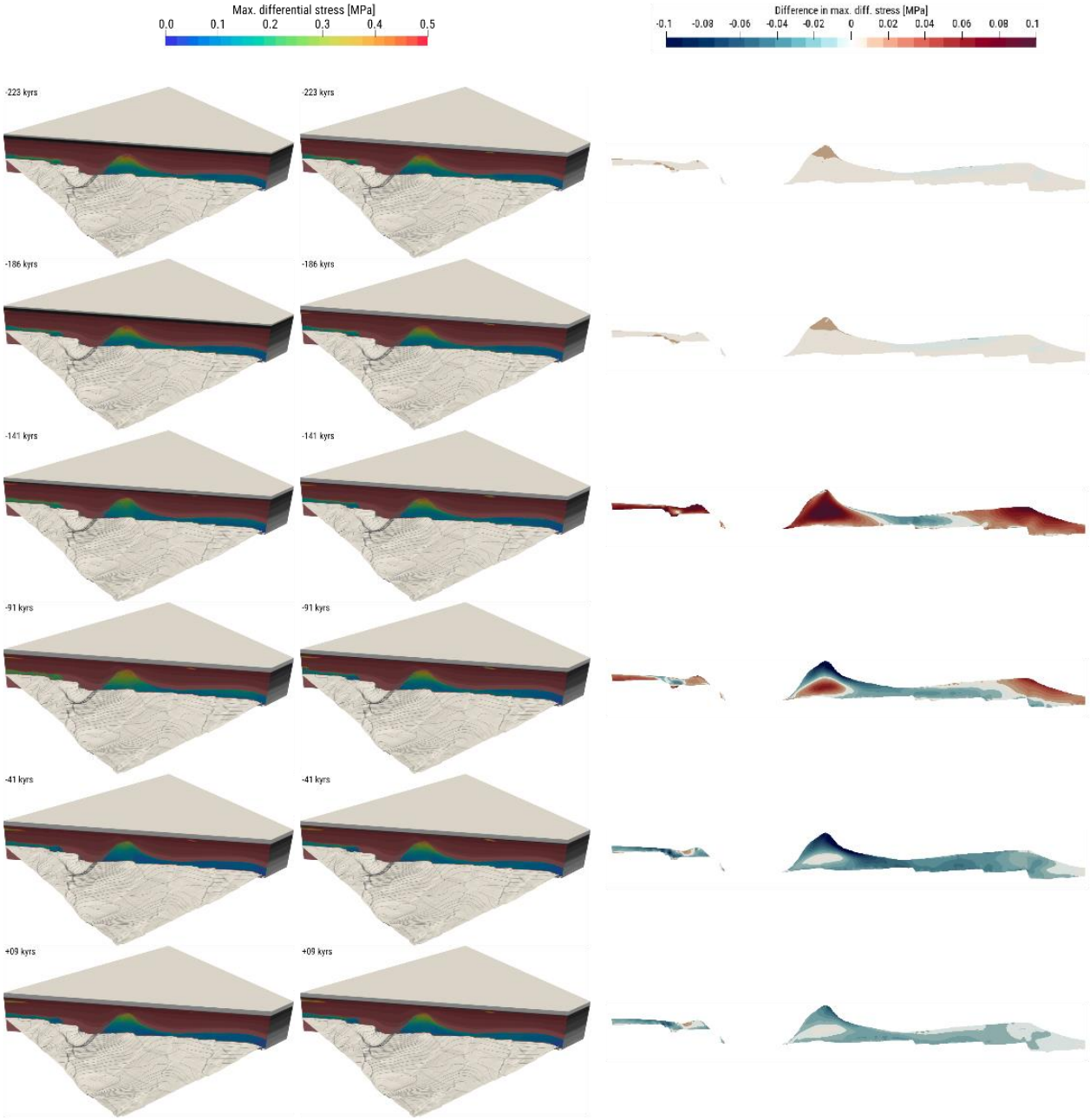

FIGURE 4.20

The effect of glacial loading on the reference DC-creep model. The left column contains a snapshot of the stress evolution over time, starting at the time when the model was entirely covered with the ice sheet. Figures in the bottom row approximately show the present-day situation. Center column is similar to the left column, but for a case without a superimposed ice sheet. The right column contains equivalent snapshots, but with the difference in maximum differential stress of left and center column.

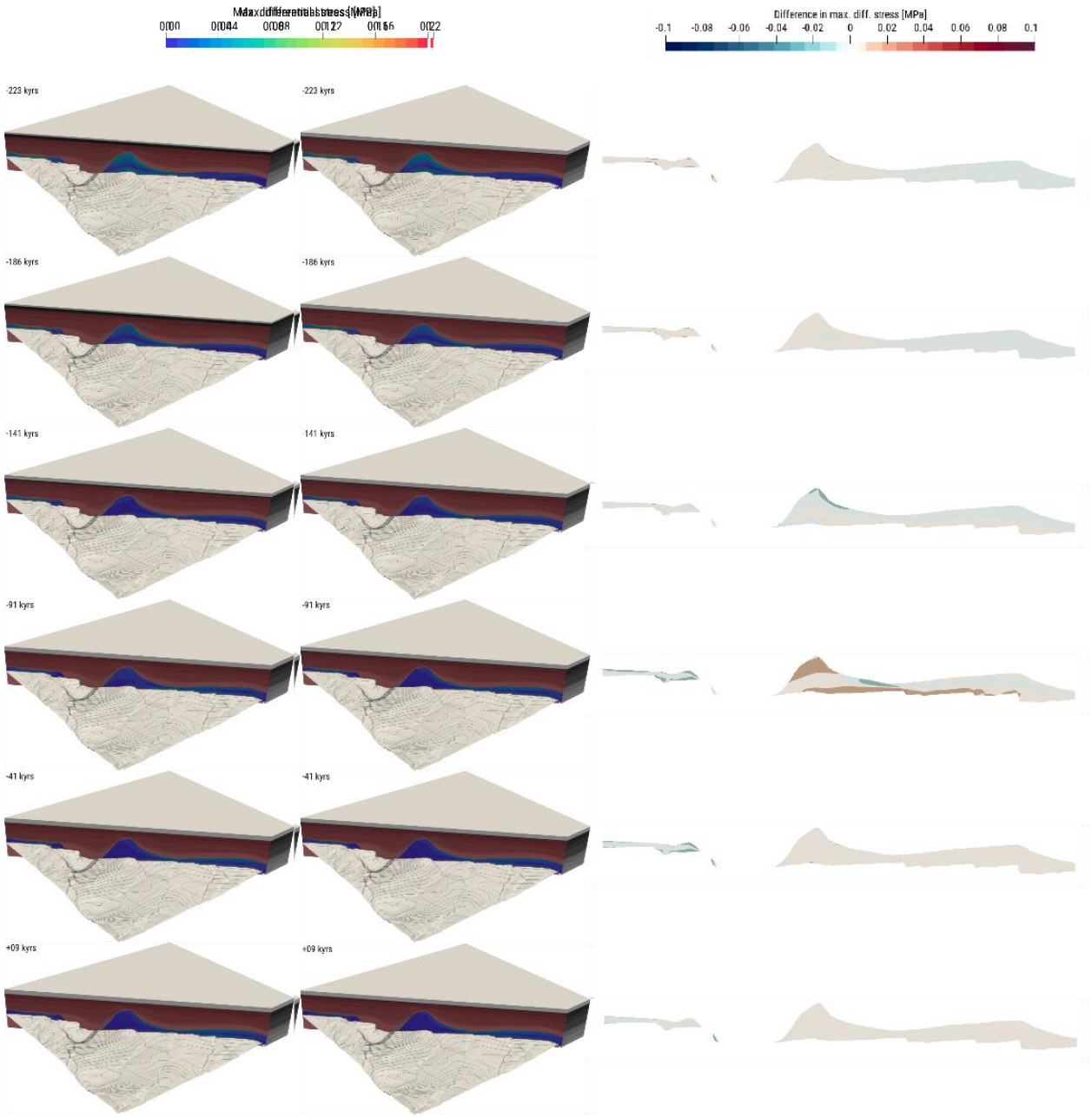

FIGURE 4.21

The effect of glacial loading for the reference PS-DC-creep model. The left column contains a snapshot of the stress evolution over time, starting at the time when the model was entirely covered with the ice sheet. Figures in the bottom row approximately show the present-day situation. Center column is similar to the left column, but for a case without a superimposed ice sheet. The right column contains equivalent snapshots, but with the difference in maximum differential stress of left and center column.

4.5.6 Summary and key observations

[1] Models with salt walls/diapirs exhibit differential stresses of up to ~0.65 MPa; the largest magnitudes occur towards the top or along the side boundaries of the salt structures if a small amount of tectonic extension is taken into account

[2] Additional vertical (un-)loading through ice masses result in slightly decreased differential stresses (~ 50 kPa) in the top part of the salt structures. However, in the case of coupled PS-DC creep, this effect is negligible.

[3] Changes in the employed dislocation creep rheology are most significant and resulting stress magnitudes differ by the same order of magnitude as if the tectonic strain rates were five times higher.

4.6 Flat bedded salt

In comparison with a salt dome, the flat bedded salt model is a much less evolved salt structure with a rather small salt thickness. Therefore, buoyancy forces are lower, and the upwelling of the salt is suppressed, which, in turn, is expected to induce much less differential stress. For this reason, we choose a DC-creep model as the reference as the DC-creep-only model is, on average, likely to result in higher differential stresses than a model with combined PS-DC-creep. Nevertheless, we provide an overview of possible stresses states obtained for models that integrate coupled PS-DC-creep but will then focus on variations of the DC-creep reference model and respective states of stress.

4.6.1 Ranges of differential stress for coupled PS-DC creep rheology

The overview of coupled PS-DC creep models (Figure 4.22) compares five models with different tectonic boundary conditions and different grain sizes. Whereas in Figure 4.22a-c the models underlie a constant d_{max} = 2.5 cm for both, the primary salt and K-Mg salt layer, we also show two models that incorporate a contrast in grain size, i.e., d_{max} = 5cm and $d_{max,K\text{-}Mg}$ = 2.5 cm, for primary and K-Mg salt respectively (Figure 4.22d,e). The models in Figure 4.22a-c are different in terms of tectonic loading. As we see, none of the applied extensional far-field deformation fields has a significant impact on the stress state for the given maximum grain size. Overall, the stress magnitudes are below 20 kPa. However, if we increase d_{max} for the primary salt, we do observe stress concentrations in the vicinity of basement faults. Still, the magnitudes are below 30 kPa. Only, if one additionally assumes a higher tectonic far-field deformation, differential stress magnitudes increase to up to 0.1 MPa.

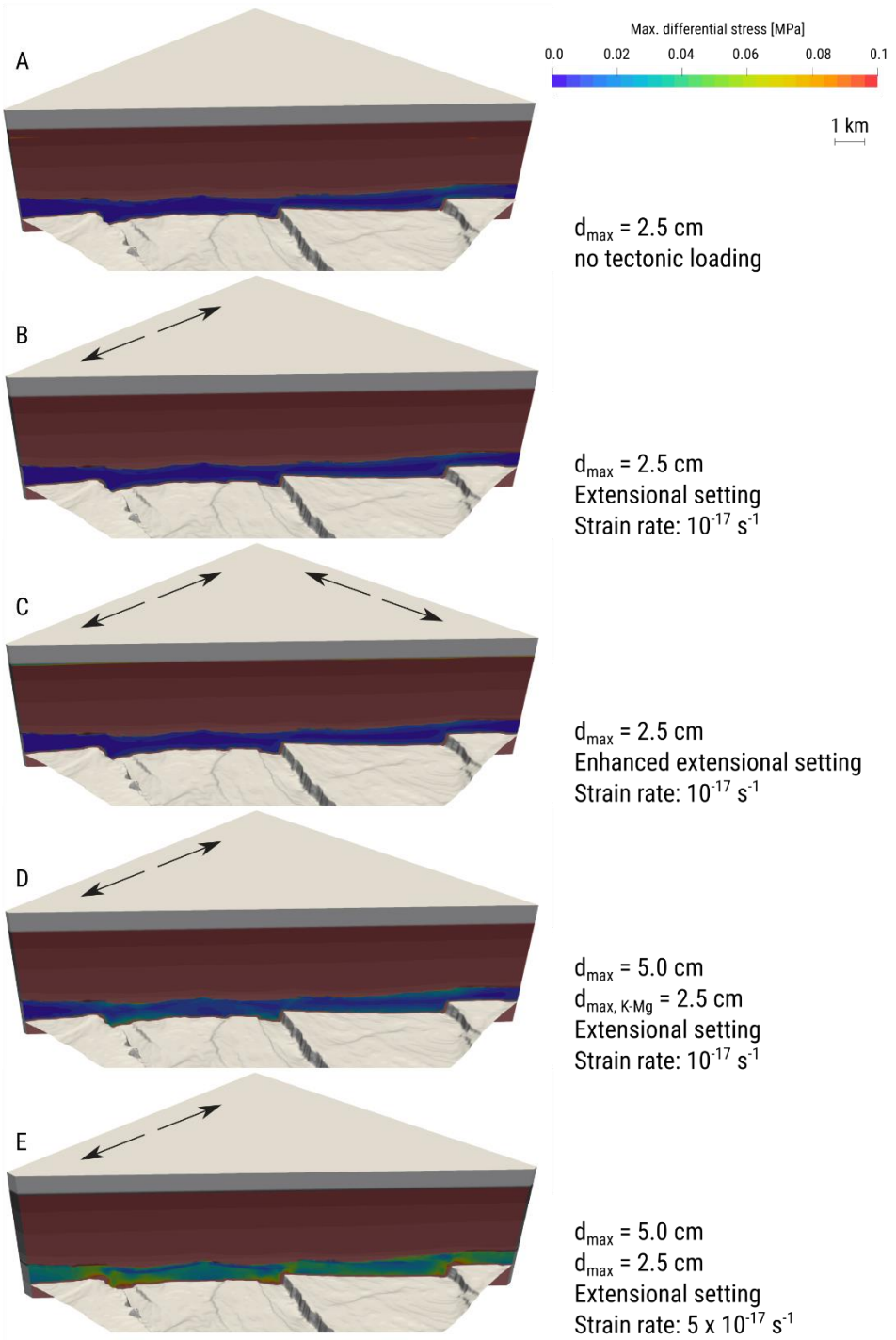

FIGURE 4.22

Overview of maximum differential stresses resulting from different models of coupled PS-DC-creep (Salt-PS-DC1, see Table 3.1). The models are different in terms of maximum grain size and tectonic boundary conditions. **A-C** share the same dmax for both, primary salt rock and K-Mg salt, but differ regarding the tectonic loading. **D & E**, both contain a contrast in grain size between the main salt (d_{max} = 5 cm) and the K-Mg salt layer (d_{max} = 2.5 cm), but E involves a far-field deformation field with a five-times higher rate.

4.6.2 DC-creep reference model of flat-bedded salt

The reference model is subject to tectonic extension (5×10^{-17} s^{-1}) and we integrate the glacial (un-) loading history. We show the maximum differential stress of the reference model in Figure 4.23a, where, on average, the stress magnitude reaches values of up to ~ 0.3 MPa. Compared to the other model geometries, this value is significantly smaller; however, we do obtain a stress concentration close to basement steps. These high-stress patches are likely related to the weak K-Mg salt layers and span over about 500 m. The deformation within the salt mostly concentrates within the K-Mg layer, but also in the vicinity of basement faults, at locations where we observe high stresses (Figure 4.23b). It should be noted that we do not impose active faults or weak zones in the basement. The elevated intra-salt areas are thus caused by a feedback of salt flow and basement geometry.

4.6.3 Variations of the DC-creep reference model

To get an overview of possible stress magnitudes when only DC-creep is active for the primary salt, we summarize selected model scenarios in Figure 4.24. Overall, the differential stress magnitudes are much higher than for comparable PS-DC creep scenarios. On average, we obtain differential stresses of up to 200 to 300 kPa. Whereas the glacial loading has no visible effect (Figure 4.24b), we do observe more notable effects if different DC-creep laws are employed. In the case of Salt-DC[4] creep ((Bräuer et al. 2011b), Figure 4.24c), we find differential stress up to 400 kPa, again in the vicinity of basement faults. If Salt-DC[3] creep of (Ter Heege et al. 2005b) is employed, the stress pattern is similar, but magnitudes only reach approximately up to 300 kPa (Figure 4.24d). Local heterogeneities (Figure 4.24f) have an impact on the stress field, but only affect the stresses within the primary salt only very locally (< 100 m).

As the example in Figure 4.24e shows, reducing the tectonic deformation rate in the far-field by a factor five decreases the overall stress amplitude by about 100 kPa.

To get better insights into the relative changes in differential stress, we illustrate how the differential stress changes in comparison to the reference model (Figure 4.25). The

overview gives an impression of the relative importance of glacial loading on the present-day stress state (Figure 4.25b). As discussed above, compared to other uncertain model inputs, the impact of glacial (un-)loading on the stress state of the flat bedded salt is insignificant and barely noticeable (< 5 kPa). Whether or not we deal with a coupled PS-DC creep or a dominant DC creep has the most significant effect within this comparison (Figure 4.25a). Differential stresses of the DC-creep reference model are at least 200-300 kPa higher than in the same model with activated PS-DC creep (Dmax=5cm). We also find that a higher tectonic extension rate increases the differential stress in the general salt layer (Figure 4.25c). The presence of relatively weak K-Mg layers results in a stress-focussing effect, which is accommodated by the more competent Halite salt, and removing these effects results in overall smaller stresses.

The impact of changing the DC-creep law is more significant than other variations. It may have a substantial effect of 100-250 kPa difference in differential stress (Figure 4.25d, e). Besides an average offset, anomalies of stronger differences occur towards faults in the basement and span over 500–1500 m in the lateral direction. Finally, adding internal heterogeneities to the model setup has a similar impact as a change in DC-creep (Figure 4.25f). Patches of higher stress span from the steps in the basement towards focussing points associated with the geometry of the K-Mg salt.

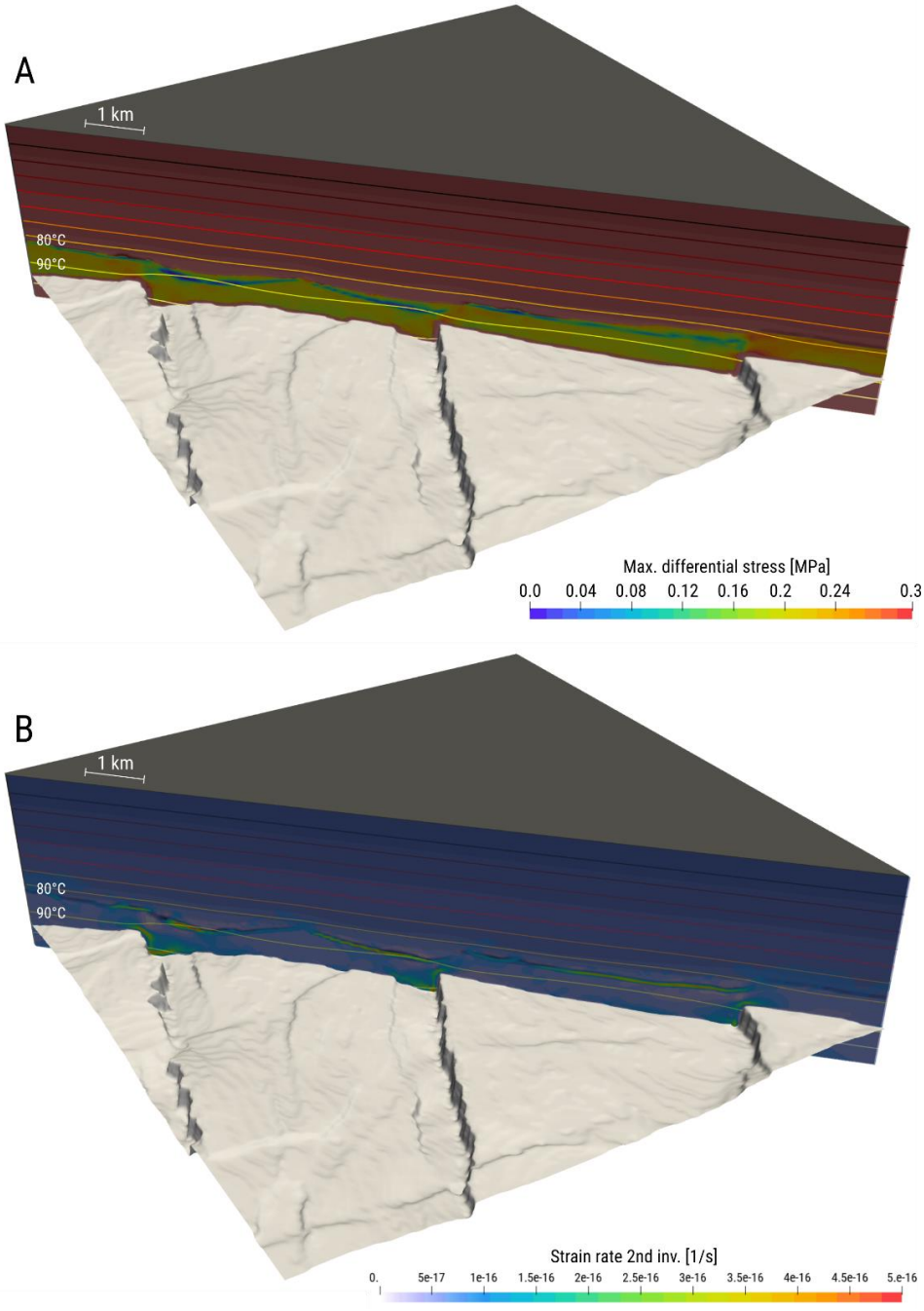

FIGURE 4.23

A DC-creep reference model for a flat-bedded salt geometry. The white surface illustrates the Top basement topography. The model is under extension with a low tectonic strain rate of $5 \cdot 10^{-17} s^{-1}$. Temperature contour lines are superimposed for reference. The average temperature within the salt is at 90°C. **A:** Maximum differential stress. High stresses are associated with basement steps and reach magnitudes up to 300 kPa. High strain rates occur within the weak K-Mg salt layer and in the vicinity of basement steps.

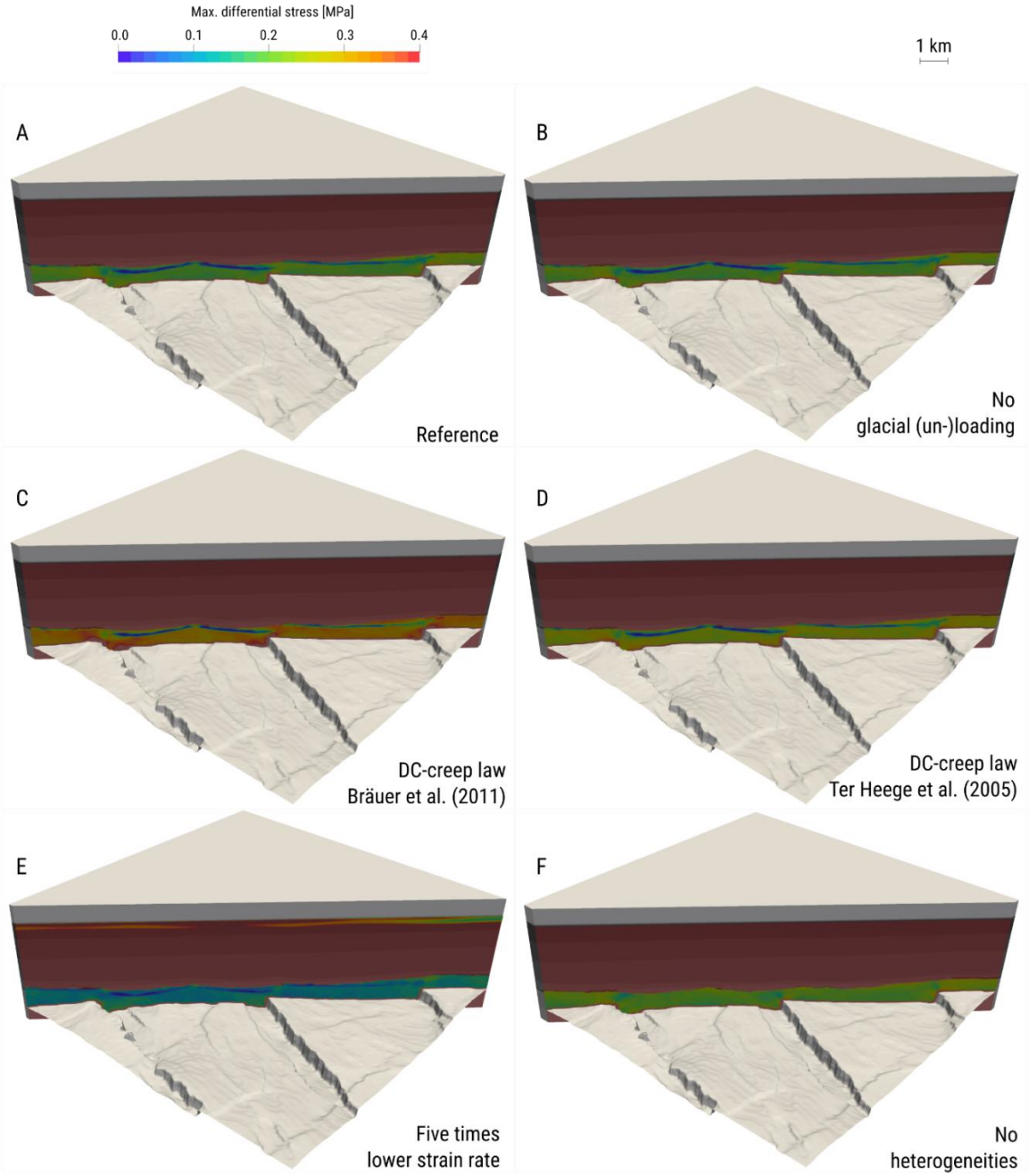

FIGURE 4.24

Comparison between DC-creep reference model (Salt-DC[2], see Table 3.1) and model variations as absolute differential stress. All models are subject to a far-field extensional tectonic setting with imposed strain rates of 5×10^{-17} s^{-1}. **A:** Reference model (Salt-DC[2], (Wawersik and Zeuch 1986)). **B:** Same but without additional loading during the latest ice age. **C:** Model with different DC-creep law (Salt-DC[3], (Ter Heege et al. 2005b)). **D:** Model with different DC-creep law (Salt-DC[4], (Bräuer et al. 2011b)). **E:** Same as A but with a lower deformation rate (1×10^{-17} s^{-1}). **F:** Similar to A but without intra-salt heterogeneities.

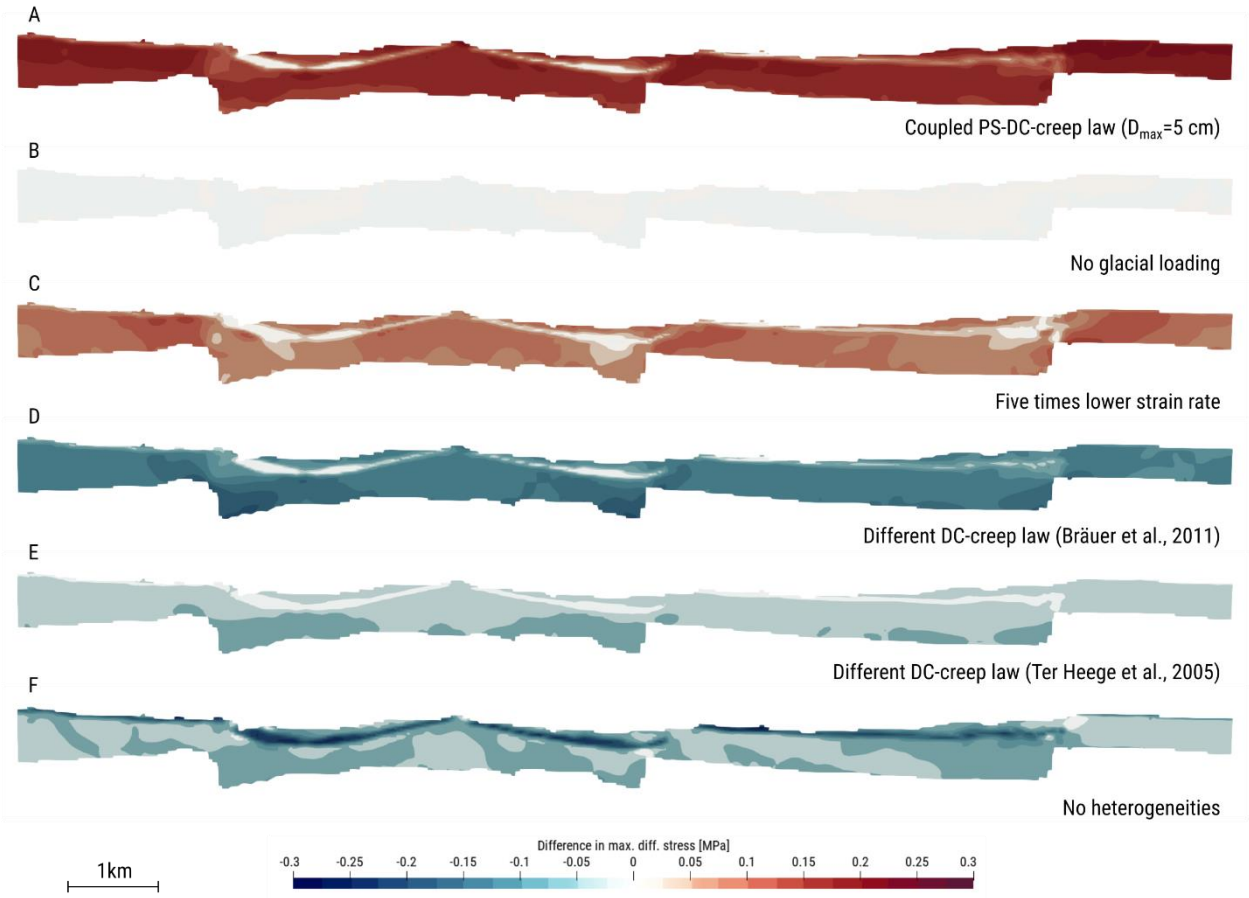

FIGURE 4.25

Relative changes in differential stress. Red colors indicate areas where differential stresses of the reference model are higher, blue colors show regions where differential stresses of the reference model are lower as in respective comparative models. A comparison with a similar model but activated coupled PS-DC creep. B illustrates the difference in differential stress due to glacial loading, and C shows the impact of less tectonic strain. D-E shows the comparison with alternative DC-creep models, and F illustrates the effect of having heterogeneities within the Zechstein salt on the stress state.

4.6.4 Summary and key observations

[1] Simulations with flat-bedded salt and a coupled PS-DC creep result in differential stresses smaller than 100 kPa. The effects of tectonic boundary conditions, glacial (un-) loading history, and changes in grain size do not cause higher stresses.

[2] If at all, high stresses in flat bedded salt only occur when PS-creep is inactive or not dominant. Here, we obtain stresses up to 400 kPa.

[3] Basement steps lead to a concentration of maximum differential stress. We observe patches of increased stress that reach up to 500 m.

[4] The presence of weak inclusion layers influences the pattern of stress distribution within the host salt rock as it must accommodate the differential stress. The location of the inclusion layers relative to the edges in the basement topography influences the pattern of stress concentration.

[5] High strain rates accumulate within weak inclusion layers.

5 Summary and Recommendations

5.1 Overall summary

We have addressed dome-scale variations in the stress field by summarizing published literature and by describing the results of new, 3D simulations tuned to three relevant scenarios in the Netherlands. We can summarize the findings as follows:

[1] Based on microstructural observations, differential stress variations of up to several MPa can be expected to occur within salt domes. There is, however, no published work that systematically measured how such stresses vary within larger-scale salt domes. There are some (weak) suggestions that stresses are higher close to shear zones within the salt structures.

[2] In-situ measured stresses from drill-holes seem to suggest smaller values of up to 1 MPa, but results are not entirely conclusive.

[3] The effect of differential stresses may have a significant effect on cavity closure rates, which will generally increase depending on the ratio of the far-field shear stress and pressure difference of the cavity with respect to the surrounding (a parameter that is likely to change during the abandonment phase). Analytical models of hole-closure suggest that the results are highly sensitive to the rheology of the rock salt.

[4] Existing literature suggests that anhydrite stringers within the salt can cause stresses of ~0.1-0.5 MPa, but existing work mostly focusses on stresses around rather than within salt structures.

[5] We, therefore, performed systematic 3D numerical simulations that took a flat-lying salt, salt pillows, and a salt wall into account, as well as internal

heterogeneities within the salt, such as a weak K-Mg-layer and higher-density stringers.

[6] We demonstrate that it is now computationally feasible to perform 3D numerical models at a dome-scale to create an uncertainty analysis of the subsurface stress state, taking into account a-priori parameter ranges from microstructural analysis and in situ constraints.

[7] Our simulation results show that differential stresses are generally largest for the salt pillow and salt wall cases and may reach values of up to 0.65 MPa, whereas stress magnitudes are rather < 0.4 MPa for flat-bedded salt cases. Stresses are largest towards the top and sides of the salt structures. Far-field tectonic deformation can enhance stresses, depending on the geometry of salt structures. Yet, for the rather low deformation rates in the Netherlands, this is not a first-order effect.

[8] Stresses can also be enhanced in the vicinity (~500 m) of basement steps and internal heterogeneities. Weak layers within the salt may result in a 'stress-focusing effect' that enhances stresses above the layers, whereas dense anhydrite stringers cause buoyancy related stresses in their vicinity.

[9] The effect of rheology is significant. The largest stress magnitudes are obtained for cases in which pressure-solution is inactive. In low-stress regime, the pressure solution creep is weaker, and hence preferable deformation mechanism, compared to the dislocation creep. The transition between the creep mechanisms is, however, poorly constrained. A particularly important parameter influencing this is the mean grain size. In order to provide more insights for a specific case study, the parametric numerical simulations combined with the microstructural analysis are generally recommended.

[10] The effect of glacial loading changes the stresses immediately after the loading was removed, but has only a minor effect on the present-day stress field within salt domes, particular given the already discussed effects and uncertainties in the material parameters.

5.2 Recommendations

[1] Caverns within flat-bedded salt structures are more likely to experience low differential stresses, provided they are not close to anhydrite stringers or steps in the basement topography.

[2] Yet, more care should be taken if cavities are built close to the top of a salt structure with more significant amplitudes, close to the lateral salt-sediment, or close to weak/strong layers within the salt such as stronger and dense anhydrite stringers or weak K-Mg-salt layers. For these cases, detailed computations are recommendable combined with microstructural analysis.

[3] It is generally advisable to consider a range of creep rheologies in models of cavity closure, including non-linear ones, as the uncertainties in rheology remain large. At this stage, it remains unclear whether closure is mostly sensitive to the rheology of the salt immediately surrounding the cavity or also to the rheology further away. This is a critical point that deserves further studies, as the creation of the cavity may re-activate grain boundaries and therefore induce pressure solution creep which micro-structural observations suggest to be otherwise currently largely inactive in many of the salt structures in the Netherlands. It is advisable to take dome-scale models into account in this, as a switch in deformation mechanism in parts of the salt structure may induce larger scale flow within the salt (and potentially activate, for example, the sinking of anhydrite stringers).

[4] In order to improve the predictive power of subsidence, subsurface deformation, and stress-state, we suggest that studies of cavity abandonment should employ integrated 4D models of the geological salt structure and its overburden, while taking the cavity construction, operation, and its abandonment phase into account. These models should not only concentrate on deformation within the salt, but also on the stress-state at the salt-host rock interface to allow estimating how this changes as a result of abandonment and evaluate the potential of hydrofracture formation there in case highly pressurized brine escapes the salt.

6 References

Adamuszek, Marta and Marcin Dabrowski. 2019. 'Sinking of a Fragmented Anhydrite Layer in Rock Salt'. *Tectonophysics*.

Albertz, Markus and Christopher Beaumont. 2010. 'An Investigation of Salt Tectonic Structural Styles in the Scotian Basin, Offshore Atlantic Canada: 2. Comparison of Observations with Geometrically Complex Numerical Models'. *Tectonics* 29(4).

Albertz, Markus, Christopher Beaumont, John W. Shimeld, Steven J. Ings, and Sofie Gradmann. 2010. 'An Investigation of Salt Tectonic Structural Styles in the Scotian Basin, Offshore Atlantic Canada: 1. Comparison of Observations with Geometrically Simple Numerical Models'. *Tectonics* 29(4):TC4017.

Albertz, Markus and Steven J. Ings. 2012. 'Some Consequences of Mechanical Stratification in Basin-Scale Numerical Models of Passive-Margin Salt Tectonics'. *Geological Society, London, Special Publications* 363(1):303–30.

Allen, Janice and Christopher Beaumont. 2012. 'Impact of Inconsistent Density Scaling on Physical Analogue Models of Continental Margin Scale Salt Tectonics'. *Journal of Geophysical Research: Solid Earth* 117(B8).

Balay, Satish, Shrirang Abhyankar, Mark F. Adams, Jed Brown, Peter Brune, Kris Buschelman, Lisandro Dalcin, Alp Dener, Victor Eijkhout, William D. Gropp, Dmitry Karpeyev, Dinesh Kaushik, Matthew G. Knepley, Dave A. May, Lois Curfman McInnes, Richard Tran Mills, Todd Munson, Karl Rupp, Patrick Sanan, Barry F. Smith, Stefano Zampini, Hong Zhang, and Hong Zhang. 2019. *PETSc Users Manual*. ANL-95/11-Revision 3.12. Argonne National Laboratory.

Baumann, T. S., B. J. P. Kaus, and P. Eichheimer. 2017. '3D Numerical Modelling of Salt Tectonics'. Paris, France.

Baumann, Tobias S., B. J. Kaus, and Anton A. Popov. 2018. 'Deformation and Stresses Related to the Gorleben Salt Structure: Insights from 3D Numerical Models'. *Mechanical Behavior of Salt, Saltmech IX* 15–27.

Berest, Pierre, Hakim Gharbi, Benoit Brouard, Dieter Brückner, Kerry DeVries, Grégoire Hévin, Gerd Hofer, Christopher Spiers, and Janos Urai. 2019. 'Very Slow Creep Tests on Salt Samples'. *Rock Mechanics and Rock Engineering*.

Bonté, D., J. D. Van Wees, and J. M. Verweij. 2012. 'Subsurface Temperature of the Onshore Netherlands: New Temperature Dataset and Modelling'. *Netherlands Journal of Geosciences* 91(4):491–515.

Bräuer, Volkmar, Ralf Eickemeier, Dieter Eisenburger, Christoph Grissemann, Jürgen Hesser, Stefan Heusermann, Diethelm Kaiser, Hans Nipp, Thomas Nowak, Ingo Plischke, Hajo Schnier, Otto Schulze, Juergen Soennke, and Jan Weber. 2011a. 'Description of the Gorleben Site Part 4 Geotechnical Exploration of the Gorleben Salt Dome'. *Federal Institute for Geosciences and Natural Resources (BGR)*.

Bräuer, Volkmar, Ralf Eickemeier, Dieter Eisenburger, Christoph Grissemann, Jürgen Hesser, Stefan Heusermann, Diethelm Kaiser, Hans Nipp, Thomas Nowak, Ingo Plischke, Hajo Schnier, Otto Schulze, Juergen Soennke, and Jan Weber. 2011b. 'Description of the Gorleben Site Part 4 Geotechnical Exploration of the Gorleben Salt Dome'. *Federal Institute for Geosciences and Natural Resources (BGR)*.

Briegel, Ueli and Walter H. Müller. 1978. 'The Rheological Behavour of Polycrystalline Anhydrite'.

Bruno, Mike, J. Ramos, and K. Lao. 2017. 'Geomechanical Stability of Solution Mined Caverns Near Salt Dome Edges, Including Influence of External Reservoir Depletion'. P. 24 in.

Burchardt, Steffi, Hemin Koyi, Harro Schmeling, and Lukas Fuchs. 2012. 'Sinking of Anhydrite Blocks within a Newtonian Salt Diapir: Modelling the Influence of Block Aspect Ratio and Salt Stratification: Sinking of Anhydrite Blocks'. *Geophysical Journal International* 188(3):763–78.

Carter, Neville L. and Francis D. Hansen. 1983. 'Creep of Rocksalt'. *Tectonophysics* 92(4):275–333.

Carter, Neville L., Francis D. Hansen, and Paul E. Senseny. 1982. 'Stress Magnitudes in Natural Rock Salt'. *Journal of Geophysical Research* 87(B11):9289.

Chemia, Z., H. Koyi, and H. Schmeling. 2008. 'Numerical Modelling of Rise and Fall of a Dense Layer in Salt Diapirs'. *Geophysical Journal International* 172(2):798–816.

Chemia, Z., H. Schmeling, and H. Koyi. 2009. 'The Effect of the Salt Viscosity on Future Evolution of the Gorleben Salt Diapir, Germany'. *Tectonophysics* 473(3–4):446–56.

Chemia, Zurab and Hemin Koyi. 2008. 'The Control of Salt Supply on Entrainment of an Anhydrite Layer within a Salt Diapir'. *Journal of Structural Geology* 30(9):1192–1200.

Cornet, J. S., M. Dabrowski, and D. W. Schmid. 2016. 'Shear Enhanced Borehole Closure'. American Rock Mechanics Association.

Cornet, Jan, Marcin Dabrowski, and Daniel Walter Schmid. 2017. 'Long-Term Cavity Closure in Non-Linear Rocks'. *Geophysical Journal International* 210(2):1231–43.

Cornet, Jan S. and Marcin Dabrowski. 2018. 'Nonlinear Viscoelastic Closure of Salt Cavities'. *Rock Mechanics and Rock Engineering* 51(10):3091–3109.

Cornet, Jan S., Marcin Dabrowski, and Daniel W. Schmid. 2018a. 'Long Term Creep Closure of Salt Cavities'. *International Journal of Rock Mechanics and Mining Sciences* 103:96–106.

Cornet, Jan S., Marcin Dabrowski, and Daniel W. Schmid. 2018b. 'Long Term Creep Closure of Salt Cavities'. *International Journal of Rock Mechanics and Mining Sciences* 103:96–106.

De Bresser, J., J. Ter Heege, and C. Spiers. 2001. 'Grain Size Reduction by Dynamic Recrystallization: Can It Result in Major Rheological Weakening?' *International Journal of Earth Sciences* 90(1):28–45.

Desbois, Guillaume, Janos L. Urai, and Johannes H. P. de Bresser. 2012. 'Fluid Distribution in Grain Boundaries of Natural Fine-Grained Rock Salt Deformed at Low Differential Stress (Qom Kuh Salt Fountain, Central Iran): Implications for Rheology and Transport Properties'. *Journal of Structural Geology* 43:128–43.

Desbois, Guillaume, Prokop Závada, Zsolt Schléder, and Janos L. Urai. 2010. 'Deformation and Recrystallization Mechanisms in Actively Extruding Salt Fountain: Microstructural Evidence for a Switch in Deformation Mechanisms with Increased Availability of Meteoric Water and Decreased Grain Size (Qum Kuh, Central Iran)'. *Journal of Structural Geology* 32(4):580–94.

Duin, E. J. T., J. C. Doornenbal, R. H. B. Rijkers, J. W. Verbeek, and Th E. Wong. 2006. 'Subsurface Structure of the Netherlands-Results of Recent Onshore and Offshore Mapping'. *Netherlands Journal of Geosciences* 85(4):245.

Duretz, Thibault, David Alexander May, T. V. Gerya, and P. J. Tackley. 2011. 'Discretization Errors and Free Surface Stabilization in the Finite Difference and Marker-in-Cell Method for Applied Geodynamics: A Numerical Study'. *Geochemistry, Geophysics, Geosystems* 12(7).

Ehlers, Jürgen. 1990. 'Reconstructing the Dynamics of the North-West European Pleistocene Ice Sheets'. *Quaternary Science Reviews* 9(1):71–83.

Eickemeier, R., S. Heusermann, M. Knauth, W. Minkley, HK NIPP, and T. Popp. 2013. 'Preliminary Safety Analysis of the Gorleben Site: Thermo-Mechanical Analysis of the Integrity of the Geological Barrier in the Gorleben Salt Formation-13307'. *WM2013*.

Fernandez, Naiara and Boris J. P. Kaus. 2015. 'Pattern Formation in 3-D Numerical Models of down-Built Diapirs Initiated by a Rayleigh–Taylor Instability'. *Geophysical Journal International* 202(2):1253–70.

Fuchs, Lukas, Hemin Koyi, and Harro Schmeling. 2014. 'Numerical Modeling on Progressive Internal Deformation in Down-Built Diapirs'. *Tectonophysics* 632:111–22.

Goteti, Rajesh, Steven J. Ings, and Christopher Beaumont. 2012. 'Development of Salt Minibasins Initiated by Sedimentary Topographic Relief'. *Earth and Planetary Science Letters* 339–340:103–16.

Gradmann, Sofie, Christopher Beaumont, and Markus Albertz. 2009. 'Factors Controlling the Evolution of the Perdido Fold Belt, Northwestern Gulf of Mexico, Determined from Numerical Models'. *Tectonics* 28(2).

Gresho, P. M. and R. L. Sani. 2000. *Incompressible Flow and the Finite Element Method, Volume 2, Isothermal Laminar Flow*. 1 edition. Chichester: Wiley.

Happel, John and Howard Brenner. 1983. *Low Reynolds Number Hydrodynamics: With Special Applications to Particulate Media*. Vol. 1. the hague: Martinus Nijhoff Publishers.

Harlow, Francis H. and J. Eddie Welch. 1965. 'Numerical Calculation of Time-Dependent Viscous Incompressible Flow of Fluid with Free Surface'. *The Physics of Fluids* 8(12):2182–2189.

Ismail-Zadeh, Alik, Igor Tsepelev, Chistopher Talbot, and Alexander Korotkii. 2004. 'Three-Dimensional Forward and Backward Modelling of Diapirism: Numerical Approach and Its Applicability to the Evolution of Salt Structures in the Pricaspian Basin'. *Tectonophysics* 387(1–4):81–103.

Jackson, Martin PA and Michael R. Hudec. 2017. *Salt Tectonics: Principles and Practice*. Cambridge University Press.

Kaus, B. J. P., A. A. Popov, T. S. Baumann, A. E. Pusok, A. Bauville, N. Fernandez, and M. Collignon. 2016. 'Forward and Inverse Modelling of Lithospheric Deformation on Geological Timescales'. Pp. 299–307 in *NIC Symposium 2016*. Vol. 48, *NIC Series*. Julich: Forschungszentrum Julich GmbH, Zentralbibliothek.

Kaus, Boris J. P. and Yuri Y. Podladchikov. 2001. 'Forward and Reverse Modeling of the Three-Dimensional Viscous Rayleigh-Taylor Instability'. *Geophysical Research Letters* 28(6):1095–98.

Kaus, Boris JP, Hans Mühlhaus, and Dave A. May. 2010. 'A Stabilization Algorithm for Geodynamic Numerical Simulations with a Free Surface'. *Physics of the Earth and Planetary Interiors* 181(1–2):12–20.

van Keken, P. E., C. J. Spiers, A. P. van den Berg, and E. J. Muyzert. 1993. 'The Effective Viscosity of Rocksalt: Implementation of Steady-State Creep Laws in Numerical Models of Salt Diapirism'. *Tectonophysics* 225(4):457–76.

King, Rosalind, Guillaume Backé, Mark Tingay, Richard Hillis, and Scott Mildren. 2012. 'Stress Deflections around Salt Diapirs in the Gulf of Mexico'. *Geological Society, London, Special Publications* 367(1):141–53.

Kneuker, Tilo, Gernold Zulauf, Michael Mertineit, Joachim Behlau, and Jörg Hammer. 2014. 'The Impact of Finite Strain on Deformation Mechanisms of Permian Stassfurt Rock Salt at the Morsleben Site (Germany): Constraints from Microfabric Studies and EBSD Analyses'. Retrieved 30 September 2019 (https://www.ingentaconnect.com/content/schweiz/zdgg/2014/00000165/00000001/art00009;jsessionid=16g106blhm69l.x-ic-live-02).

Koyi, Hemin A. 2001. 'Modeling the Influence of Sinking Anhydrite Blocks on Salt Diapirs Targeted for Hazardous Waste Disposal'. *Geology* 29(5):387–390.

Lang, Jörg, Andrea Hampel, Christian Brandes, and Jutta Winsemann. 2014. 'Response of Salt Structures to Ice-Sheet Loading: Implications for Ice-Marginal and Subglacial Processes'. *Quaternary Science Reviews* 101:217–33.

Lang, Jörg, Tobias Lauer, and Jutta Winsemann. 2018. 'New Age Constraints for the Saalian Glaciation in Northern Central Europe: Implications for the Extent of Ice Sheets and Related Proglacial Lake Systems'. *Quaternary Science Reviews* 180:240–259.

Lauer, Tobias and Marcel Weiss. 2018. 'Timing of the Saalian-and Elsterian Glacial Cycles and the Implications for Middle–Pleistocene Hominin Presence in Central Europe'. *Scientific Reports* 8(1):5111.

Leitner, Christoph, Franz Neubauer, János L. Urai, and Johannes Schoenherr. 2011. 'Structure and Evolution of a Rocksalt-Mudrock-Tectonite: The Haselgebirge in the Northern Calcareous Alps'. *Journal of Structural Geology* 33(5):970–984.

Li, S., S. Abe, J. L. Uraï, F. Strozyk, P. A. Kukla, and H. Van Gent. 2012. 'A Method to Evaluate Long-Term Rheology of Zechstein Salt in the Tertiary'. *Proc. Mech. Beh. Salt VII* 215–220.

Li, Shiyuan, Steffen Abe, Lars Reuning, Stephan Becker, Janos L. Urai, and Peter A. Kukla. 2012. 'Numerical Modelling of the Displacement and Deformation of Embedded Rock Bodies during Salt Tectonics: A Case Study from the South Oman Salt Basin'. *Geological Society, London, Special Publications* 363(1):503–20.

Li, Shiyuan and Janos L. Urai. 2016. 'Numerical Modeling of Gravitational Sinking of Anhydrite Stringers in Salt (at Rest)'.

Li, Shiyuan, Janos L. Urai, and Guangqing Zhang. 2017. 'Numerical Modeling of the Deformation of Embedded Brittle Rock Bodies in Compressive Environment during Salt Tectonics – A Case Study from SOSB'. *Journal of Petroleum Science and Engineering* 152:1–8.

Luo, Gang, Michael R. Hudec, Peter B. Flemings, and Maria A. Nikolinakou. 2017. 'Deformation, Stress, and Pore Pressure in an Evolving Suprasalt Basin: Stress and Overpressure in Salt Basins'. *Journal of Geophysical Research: Solid Earth* 122(7):5663–90.

Luo, Gang, Maria A. Nikolinakou, Peter B. Flemings, and Michael R. Hudec. 2012. 'Geomechanical Modeling of Stresses Adjacent to Salt Bodies: Part 1—Uncoupled Models'. *AAPG Bulletin* 96(1):43–64.

Mechelse. 2017. 'The In-Situ Stress Field in the Netherlands: Regional Trends, Local Deviations and an Analysis of the Stress Regimes in the Northeast of the Netherlands'. Delft University of Technology.

Mertineit, Michael, Michael Schramm, Jörg Hammer, and Gernold Zulauf. 2014. 'Deformation of Anhydrite Rocks (Gorleben-Bank, Z3OSM) in a High-Strain Domain of the Gorleben Salt Dome, Germany'. *Zeitschrift Der Deutschen Gesellschaft Für Geowissenschaften* 165(1):49–62.

Mossop, A. P. 2012. 'Production-Induced Stress Change in and Above a Reservoir Pierced by Two Salt Domes: A Geomechanical Model and Its Applications'. *SPE Journal* 18.

Nikolinakou, Maria A., Peter B. Flemings, and Michael R. Hudec. 2014. 'Modeling Stress Evolution around a Rising Salt Diapir'. *Marine and Petroleum Geology* 51:230–38.

Nikolinakou, Maria A., Michael R. Hudec, and Peter B. Flemings. 2014. 'Comparison of Evolutionary and Static Modeling of Stresses around a Salt Diapir'. *Marine and Petroleum Geology* 57:537–45.

Nikolinakou, Maria A., Gang Luo, Michael R. Hudec, and Peter B. Flemings. 2012. 'Geomechanical Modeling of Stresses Adjacent to Salt Bodies: Part 2—Poroelastoplasticity and Coupled Overpressures'. *AAPG Bulletin* 96(1):65–85.

Nocquet, J. M., E. Calais, and B. Parsons. 2005. 'Geodetic Constraints on Glacial Isostatic Adjustment in Europe'. *Geophysical Research Letters* 32(6).

Pelletier, Dominique, Andre Fortin, and Ricardo Camarero. 1989. 'Are FEM Solutions of Incompressible Flows Really Incompressible? (Or How Simple Flows Can Cause Headaches!)'. *International Journal for Numerical Methods in Fluids* 9(1):99–112.

Podladchikov, Yu, C. Talbot, and A. N. B. Poliakov. 1993. 'Numerical Models of Complex Diapirs'. *Tectonophysics* 228(3–4):189–198.

Poliakov, A.N.B., Yu. Podladchikov, and C. Talbot. 1993. 'Initiation of Salt Diapirs with Frictional Overburdens: Numerical Experiments'. *Tectonophysics* 228(3–4):199–210.

Poliakov, A. N. B., R. Van Balen, Yu Podladchikov, Betrand Daudre, SAPL Cloetingh, and Chris Talbot. 1993. 'Numerical Analysis of How Sedimentation and Redistribution of Surficial Sediments Affects Salt Diapirism'. *Tectonophysics* 226(1–4):199–216.

Poliakov, Alexei NB, Yuri Yu Podladchikov, Ethan Ch Dawson, and Christopher J. Talbot. 1996. 'Salt Diapirism with Simultaneous Brittle Faulting and Viscous Flow'. *Geological Society, London, Special Publications* 100(1):291–302.

Popov, A. A. and S. V. Sobolev. 2008. 'SLIM3D: A Tool for Three-Dimensional Thermomechanical Modeling of Lithospheric Deformation with Elasto-Visco-Plastic Rheology'. *Physics of the Earth and Planetary Interiors* 171(1):55–75.

Raith, Alexander F. and Janos L. Urai. 2018. 'Squeeze Mining-Induced Stress Changes in the Faulted Overburden of the Veendam Salt Pillow'. *Mechanical Behavior of Salt, Saltmech IX* 807–21.

Rummel, Fritz, Benke, Klaus, and Denzai, Klaus. 1996. 'Hydraulic Fracturing Stress Measurements in the Krummhörn Gas Storage Field, Northwestern Germany'. in *SMRI Spring Meeting*.

Schléder, Zsolt, Stanis\law Burliga, and János L. Urai. 2007. 'Dynamic and Static Recrystallization-Related Microstructures in Halite Samples from the K\lodawa Salt Wall (Central Poland) as Revealed by Gamma-Irradiation'. *Neues Jahrbuch Für Mineralogie-Abhandlungen: Journal of Mineralogy and Geochemistry* 184(1):17–28.

Schléder, Zsolt and János L. Urai. 2005. 'Microstructural Evolution of Deformation-Modified Primary Halite from the Middle Triassic Röt Formation at Hengelo, The Netherlands'. *International Journal of Earth Sciences* 94(5):941–55.

Schléder, Zsolt and János L. Urai. 2007. 'Deformation and Recrystallization Mechanisms in Mylonitic Shear Zones in Naturally Deformed Extrusive Eocene–Oligocene Rocksalt from Eyvanekey Plateau and Garmsar Hills (Central Iran)'. *Journal of Structural Geology* 29(2):241–55.

Schmid, Daniel W., Yuri Y. Podladchikov, and Fernando O. Marques. 2004. 'Folding of a Finite Length Power Law Layer'. *Journal of Geophysical Research: Solid Earth* 109(B3).

Schoenherr, Johannes, Janos L. Urai, Peter A. Kukla, Ralf Littke, Zsolt Schléder, Jean-Michel Larroque, Mark J. Newall, Nadia Al-Abry, Hisham A. Al-Siyabi, and Zuwena Rawahi. 2007. 'Limits to the Sealing Capacity of Rock Salt: A Case Study of the

Infra-Cambrian Ara Salt from the South Oman Salt Basin'. *AAPG Bulletin* 91(11):1541–57.

Schreiner, Wolfgang, Gernot Jäpel, and Till Popp. 2004. 'Pneumatic Fracture Tests and Numerical Modeling for Evaluation of the Maximum Gas Pressure Capacity and the Effective Stress Conditions in the Leaching Horizon of Storage Caverns in Salt Diapirs'. in *SMRI Fall Conference*.

Schultz-Ela, Daniel D. 2003. 'Origin of Drag Folds Bordering Salt Diapirs'. *AAPG Bulletin* 87(5):757–780.

Spiers, C. J., P. M. T. M. Schutjens, R. H. Brzesowsky, C. J. Peach, J. L. Liezenberg, and H. J. Zwart. 1990. 'Experimental Determination of Constitutive Parameters Governing Creep of Rocksalt by Pressure Solution'. *Geological Society, London, Special Publications* 54(1):215–27.

Strozyk, F., H. Van Gent, J. L. Urai, and P. A. Kukla. 2012. '3D Seismic Study of Complex Intra-Salt Deformation: An Example from the Upper Permian Zechstein 3 Stringer, Western Dutch Offshore'. *Geological Society, London, Special Publications* 363(1):489–501.

Strozyk, Frank, Janos L. Urai, Heijn van Gent, Martin de Keijzer, and Peter A. Kukla. 2014. 'Regional Variations in the Structure of the Permian Zechstein 3 Intrasalt Stringer in the Northern Netherlands: 3D Seismic Interpretation and Implications for Salt Tectonic Evolution'. *Interpretation* 2(4):SM101–17.

Svendsen, John Inge, Helena Alexanderson, Valery I. Astakhov, Igor Demidov, Julian A. Dowdeswell, Svend Funder, Valery Gataullin, Mona Henriksen, Christian Hjort, and Michael Houmark-Nielsen. 2004. 'Late Quaternary Ice Sheet History of Northern Eurasia'. *Quaternary Science Reviews* 23(11–13):1229–1271.

Ter Heege, J. H., J. H. P. De Bresser, and C. J. Spiers. 2005a. 'Dynamic Recrystallization of Wet Synthetic Polycrystalline Halite: Dependence of Grain Size Distribution on Flow Stress, Temperature and Strain'. *Tectonophysics* 396(1–2):35–57.

Ter Heege, J. H., J. H. P. De Bresser, and C. J. Spiers. 2005b. 'Rheological Behaviour of Synthetic Rocksalt: The Interplay between Water, Dynamic Recrystallization and Deformation Mechanisms'. *Journal of Structural Geology* 27(6):948–63.

Thiemeyer, Nicolas, Gernold Zulauf, Michael Mertineit, Jolien Linckens, Maximilian Pusch, and Jörg Hammer. 2016. 'Microfabrics and 3D Grain Shape of Gorleben Rock Salt: Constraints on Deformation Mechanisms and Paleodifferential Stress'. *Tectonophysics* 676:1–19.

Urai, J. L. and C. J. Spiers. 2007. 'The Effect of Grain Boundary Water on Deformation Mechanisms and Rheology of Rocksalt during Long-Term Deformation'. *The*

Mechanical Behavior of Salt – Understanding of THMC Processes in Salt. Retrieved 30 September 2019 (https://www.taylorfrancis.com/).

Urai, Janos L., Christopher J. Spiers, Hendrik J. Zwart, and Gordon S. Lister. 1986. 'Weakening of Rock Salt by Water during Long-Term Creep'. *Nature* 324(6097):554–57.

Urai, Janos, Zsolt Schléder, Chris Spiers, and Peter Kukla. 2008. 'Flow and Transport Properties of Salt Rocks'. Pp. 277–90 in *Dynamics of Complex Intracontinental Basins: The Central European Basin System*.

Van Gent, Heijn, Janos L. Urai, and Martin de Keijzer. 2011. 'The Internal Geometry of Salt Structures – A First Look Using 3D Seismic Data from the Zechstein of the Netherlands'. *Journal of Structural Geology* 33(3):292–311.

Wawersik, W. R. and D. H. Zeuch. 1986. 'Modeling and Mechanistic Interpretation of Creep of Rock Salt below 200°C'. *Tectonophysics* 121(2–4):125–52.

Weijermars, R. 2015. 'Salt Sheet Coalescence in the Walker Ridge Region (Gulf of Mexico): Insights from Analytical Models'. *Tectonophysics* 640–641:39–52.

Weijermars, R., M. R. Hudec, T. P. Dooley, and M. P. A. Jackson. 2015. 'Downbuilding Salt Stocks and Sheets Quantified in 3-D Analytical Models: 3D MODELS OF DOWNBUILDING SALT DIAPIRS'. *Journal of Geophysical Research: Solid Earth* 120(6):4616–44.

Weijermars, Ruud and Martin P. A. Jackson. 2014. 'Predicting the Depth of Viscous Stress Peaks in Moving Salt Sheets: Conceptual Framework and Implications for Drilling'. *AAPG Bulletin* 98(5):911–45.

Weinberg, Roberto Ferrez and Yuri Podladchikov. 1994. 'Diapiric Ascent of Magmas through Power Law Crust and Mantle'. *Journal of Geophysical Research: Solid Earth* 99(B5):9543–9559.

Willson, Stephen M. and Joanne T. Fredrich. 2005. 'Geomechanics Considerations for Through- and Near-Salt Well Design'. in *SPE Annual Technical Conference and Exhibition*. Dallas, Texas: Society of Petroleum Engineers.

Závada, Prokop, Guillaume Desbois, Alexander Schwedt, Ondrej Lexa, and Janos L. Urai. 2012. 'Extreme Ductile Deformation of Fine-Grained Salt by Coupled Solution-Precipitation Creep and Microcracking: Microstructural Evidence from Perennial Zechstein Sequence (Neuhof Salt Mine, Germany)'. *Journal of Structural Geology* 37:89–104.

van der Zee, Wouter, Cem Ozan, Martin Brudy, and Marc Holland. 2011. '3D Geomechanical Modeling of Complex Salt Structures'. in *SIMULIA customer conference*.

Zoback, Mark D. 2010. *Reservoir Geomechanics*. Cambridge University Press.